The structure and properties of silica thin films and nanowires

Taehyun Kim

October 2009

A thesis submitted for the degree of

Doctor of Philosophy

of

The Australian National University

Certificate

This thesis, to the best of my knowledge and belief, does not contain any results previously published by another person or submitted for a degree or diploma at any university except where due reference is made in the text.

Taehyun Kim

October 19, 2009

Acknowledgements

Most of all, I wish to record my thanks to Prof. Rob Elliman, my excellent supervisor, for his faith in this project and his patient encouragement over many years. I am fortunate to have had the opportunity to work with him and not have hoped for a better mentor. His dedication, knowledge, and skill as a research scientist are an inspiration. Thank you.

I would like to thank my advisory panel Prof. Neville Fletcher and Dr. Tessica Dall for their invaluable advice, discussion and academic support.

Next, I would like to thank the rest of the research group: my postdoctoral fellows Dr. Avi Shalav, Dr. Dinesh Venkatachalam, and Dr Andrew Wilkinson for providing feedback on this project and suggesting corrections to this thesis. Dr. Kidane Belay, my general staff fellow, for his experimental skill and help. Muhammad Nawaz, Daniel Pyke, and Anwaar Malik, the fellow Ph.D. students for making the last few years friendly and enjoyable.

I would also like to thank the people of EME for their kind, patience, and help.

I would like to thank and acknowledge contributions for the following people.

- Dr. Jodie Bradby and Dr. Simon Ruffell for performing the Hardness measurements.
- Dr. Damien McGrouther of the University of New South Wales for imaging with Foused Ion Beam.
- Prof. Neville Flatcher for his theoretical modeling work.
- Dr. Tessica Dall for helping Hi-ERDA measurement.

- Dr. Andrew Wikinson for helping implantation work.
- David Liewellyn for his help with microscopy imaging and TEM sample preparation.
- Steven Huth for his contributions to provide TEM image.
- Dr. Marc Spooner for preliminary study of film mechanical properties in chapter 3.
- Dr. Praveen Kumar Sekhar for his contributions in preliminary study of nanowire project.
- Dr. Avi Shalav for setting up optical and PL system.
- Prof. Suk-ho Choi and his group in Korea for helping electric measurement of memory device.
- Non-academic staff at EME for keeping everything running smoothely.
- Prof. Neil Manson for helping scholarship.
- The School Computer Unit.
- Anyone else I may have neglected to mention.

Last, but certainly not least, I am indebted to the support of my family. Thank you Man and Dad for their unlimited supporting whatever I do. Thank you my three old sisters and brother in law for their unconditional scarifying. Thank you my three nieces for their love. Thank you my friends in Korea for their unchanged belief. Thank you God for everything.

Abstract

This thesis presents the structure and physical properties of silicon rich oxide (SRO) films and SiO_x nanowires for their potential applications in non-volatile memory device or optical- and bio-sensors.

As an extension of earlier study, the mechanical properties of SRO films deposited by plasma enhanced chemical vapour deposition (PECVD) were studied to correlate with loss of hydrogen during annealing process. Two distinct modes (Straight and oscillating) of crack propagation for films on a (100) Si substrate are reported. Amplitude and wavelength of oscillating cracks affected by SiO_2 buffer layer and failure behavior on film irradiated by ion implantation techniques are examined. Charge trapping related to hydrogen release in the SRO films and the formation of metal nanoparticles within SRO films by direct thermal reaction is also briefly discussed.

During the fabrication process of metal nanoparticles, the growth of amorphous silica (SiO_x) nanowires was observed. A systematic study has been performed to understand the growth mechanism of the SiO_x nanostructures and a growth model based on the VLS mechanism is proposed by the production of SiO as a vapour phase source of Si and O via a reaction between Si and residual oxygen, present in the annealing ambient at 3-10ppm, described by: $2Si + O_2 \rightarrow 2SiO$. The dominance of this reaction over the competing reaction: $Si + O_2 \rightarrow SiO_2$ is a strong function of oxygen concentration and temperature and for the fixed oxygen concentration employed in this study, limits growth to the temperature range >1000°C.

The controlled growth of nanowires depending on growth conditions, including catalyst/substrate combination, process gases, growth temperature and time, or combinations of these parameters, is reported. In addition, more subtle growth modes including the growth of nanowires on silica substrate with a secondary source of SiO produced by a Si capping wafer in the vicinity of the substrate are investigated.

This thesis also discusses the fabrication of hybrid metal-silica nanostructures including self-supporting nanowires films, Au-peapod structures, Au-decorated nanowires, core-shell, and hyper-hybrid SiO_x nanowires. A growth model is proposed and their basic properties such as photoluminescence and optical absorption are investigated.

Journal publications related to this thesis

Chapter 3:

- R.G. Elliman, T.D.M. Dall, M. Spooner, **T.H. Kim**, A.R. Wilkinson, "Stress and stress relief in dielectric thin films- the role of hydrogen", Nucl. Instr. Meth. B249, 310-313 (2006)

- R.G. Elliman, T.D.M. Weijers-Dall, M.G. Spooner, **T.H. Kim**, A.R. Wilkinson, S. Huth and V. Tobias, "Novel crack propagation in PECVD-deposited dielectric thin films", Nucl. Instr. Meth. B257, 554-557 (2007)

- R.G. Elliman, M. Spooner, T.D.M. Dall, **T.H. Kim** and N.H. Fletcher, "Oscillating cracks in glassy films on silicon substrates", Phil. Mag. 87, 4893-4906 (2007)

Chapter 5:

- R.G. Elliman, A.R. Wilkinson, **T.H. Kim**, P.K. Sekhar, and S. Bhansali, "Optical emission from erbium-doped silica nanowires", Journal of Applied Physics 103, 104304 (2008)

- R.G. Elliman, A.R. Wilkinson, **T.H. Kim**, P.K. Sekhar, and S. Bhansali, "Ion beam synthesis and doping of photonic nanostructures", Nucl. Instr. Meth. B266, 1362-1365 (2008)

- P.K. Sekhar, A.R. Wilkinson, R.G. Elliman, **T.H. Kim**, and S. Bhansali, "Erbium Emission from Nanoengineered Silicon Surface", J. Phys.Chem, C112, 20109-20113 (2008)

- N.H. Fletcher, R.G. Elliman, and **T.H. Kim**, "Gold bead-strings in silica nanowires: a simple diffusion model", Nanotechnology, 20, 085613 (2009)

Table of Contents

List of Figures

List of Tables

Chapter 1

Introduction

1.1 Overview

Silicon oxides (SiO_2), nitrides (Si_3N_4), and oxynitrides (SiO_xN_y) have been intensively studied because of their technological importance in microelectronic, optoelectronic and micro-electro-mechanical systems (MEMS) based applications[1-6]. Films of these materials are typically deposited onto host substrates by techniques such as chemical vapour deposition (CVD)[7, 8] or sputter deposition[9]. However, the as-deposited films often contain high levels of residual stress[10, 11]. The fabrication of most devices also involves thermal cycling, which can further contribute to the thin film stress[12]. An understanding of such thin-film stress and film failure modes is critical in most applications.

The excellent thermal stability, biocompatibility and chemical inertness of silica has also led to applications involving nanostructured material with high surface-to-volume fraction such as porous silica, and more recently silica nanowires. These materials have great potential for bio- and environmental sensing.

1.2 Motivation for current study

Silicon rich silicon oxide (SRO) films (NB: SRO is used throughout this thesis to mean silicon-rich oxide and oxynitride films) have properties, such as their refractive index, that depend on the excess silicon concentration and they have been exploited in recent years to fabricate light-emitting silicon nanocrystals and optical waveguides. Our preliminary work in this area showed that SRO films deposited by plasma enhanced chemical vapour deposition (PECVD) contain high concentrations of hydrogen. The hydrogen was found to be released from the films during subsequent annealing at temperatures above about 400°C and to be correlated with an increase in tensile stress. The current study extends this initial work and assesses SRO films for use in non-volatile memory applications. Specifically, the latter investigates charge trapping at the defects produced by hydrogen desorption and at the synthesis of metal and/or metal silicide nanocrystals by metal diffusion and reaction within SRO films.

During the course of our study to understand the formation of transition-metal nanoparticles in the SRO matrix we observed the growth of amorphous silicon-rich silica nanowires. This led to a major new research direction aimed at understanding their growth and functionalisations. This study was further motivated by the unique physical properties of nano-structured silica and its potential for novel bio-sensing applications. This work led to a provisional patent.

1.3 Thesis structure

This thesis is presented in six chapters, including this introduction. Chapter 2 briefly introduces the various experimental techniques used in this thesis. The main experimental results are then presented in Chapters 3 to 5. Chapter 3 presents results on the thermal stability and mechanical properties of the SRO films and concludes with a brief survey of potential applications. Chapters 4 to 5 present the results on silica nanowires, with Chapter 4 concentrating on the growth, structure and properties of silica nanowires, and Chapter 5 concentrating on with the fabrication, structure and properties of hybrid metal-silica nanostructures. Finally, Chapter 6 summarizes the conclusions and discusses possible directions for future work.

1.4 References

[1] S. R. Walker, J. A. Davies, P. Mascher, S. G. Wallace, W. N. Lennard, G. R. Massoumi, R. G. Elliman, T. R. Ophel, H. Timmers, *Nuclear Instruments & Methods in Physics Research Section B-Beam Interactions with Materials and Atoms* **2000**, *170*, 461.

[2] K. Danaie, A. Bosseboeuf, C. Clerc, C. Gousset, G. Julie, *Sensors and Actuators a-Physical* **2002**, *99*, 78.

[3] M. Modreanu, M. Gartner, N. Tomozeiu, A. Szekeres, *Journal of Optoelectronics and Advanced Materials* **2001**, *3*, 575.

[4] T. Baak, *Applied Optics* **1982**, *21*, 1069.

[5] N. Hatzopoulos, D. I. Siapkas, P. L. F. Hemment, W. Skorupa, *Journal of Applied Physics* **1996**, *80*, 4960.

[6] M. C. Netti, M. D. B. Charlton, G. J. Parker, J. J. Baumberg, *Applied Physics Letters* **2000**, *76*, 991.

[7] D. Dong, E. A. Irene, D. R. Young, *Journal of the Electrochemical Society* **1978**, *125*, 819.

[8] P. G. Pai, S. S. Chao, Y. Takagi, G. Lucovsky, *Journal of Vacuum Science & Technology a-Vacuum Surfaces and Films* **1986**, *4*, 689.

[9] O. Hanaizumi, K. Ono, Y. Ogawa, *Applied Physics Letters* **2003**, *82*, 538.

[10] A. C. Adams, F. B. Alexander, C. D. Capio, T. E. Smith, *Journal of the Electrochemical Society* **1981**, *128*, 1545.

[11] A. Sassella, A. Borghesi, F. Corni, A. Monelli, G. Ottaviani, R. Tonini, B. Pivac, M. Bacchetta, L. Zanotti, *Journal of Vacuum Science & Technology a-Vacuum Surfaces and Films* **1997**, *15*, 377.

[12] M. P. Hughey, R. F. Cook, *Thin Solid Films* **2004**, *460*, 7.

Chapter 2

Experimental Techniques

This chapter provides a brief overview of the various experimental techniques used in this thesis. Additional specific details are provided in each of the experimental chapters.

2.1 Sample preparation methodology

Silicon-rich-oxide, amorphous-silicon and metal thin films were deposited onto various substrates using plasma-enhanced chemical vapour deposition (PECVD) and sputter deposition techniques. Additionally ion implantation techniques were used for ion-irradiation and doping effects of selected samples. Thermal annealing of the samples was carried out in an open quartz tube furnace.

2.1.1 Plasma enhanced chemical vapour deposition (PECVD)

An Oxford Plasmalab 80 PECVD system was used to deposit the silicon rich oxide (SRO) films on silicon substrates. Figure 2.1 shows a schematic diagram of the PECVD system. The upper electrode is connected to a 13.56 MHz RF generator and the sample is placed on the lower electrode. During the deposition process, dilute silane (95% N_2 + 5% SiH_4) and nitrous oxide (N_2O) are introduced into reactor chamber and the RF generator produces plasma between two circular electrodes. When highly reactive radicals in the plasma encounter other reactive species on the sample surface, a solid layer of SiO_xN_y composition is formed. For films deposited in the present study, the RF power, pressure and temperature in the reactor were 20W, 1 Torr, and 300°C respectively. For this study, the composition of SRO films was controlled by varying the flow rate of N_2O whilst holding that of SiH_4 content. The flow rates of the various gases and the corresponding film compositions are listed in Table 2.1[1]. The hydrogen content is not given explicitly here as it is a volatile component of the film and varies with annealing temperature, as discussed in Chapter3.

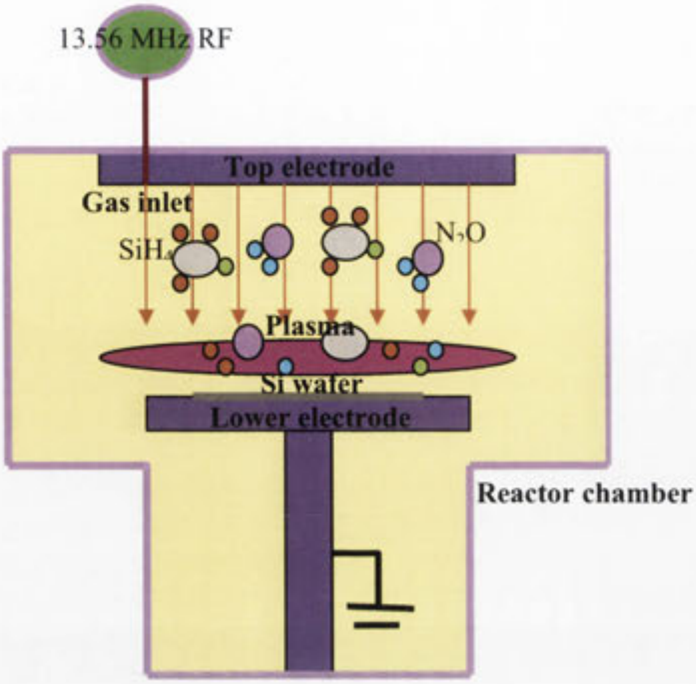

Figure 2.1: The schematic diagram of the PECVD system [2].

Table 2.1: Flow rates used to produce the various SRO films.

Material	N_2O flow rate (sccm)	SiH_4 flow rate (sccm)	NH_3 flow rate (sccm)
$SiO_{2.13}N_{0.05}$:H	700	160	0
$SiO_{1.14}N_{0.25}$:H	75	160	0
$SiO_{1.16}N_{0.32}$:H	50	160	0
$SiO_{0.85}N_{0.35}$:H	35	160	0
$SiO_{0.65}N_{0.44}$:H	25	160	0

2.1.2 Ion implantation

Ion-irradiation and doping of films and nanostructures were carried out using either the ANU 175kV ion implanter or the ANU 1.7MV tandem accelerator (National electrostatics corporation, USA, 5SDH-4). Figure 2.2 shows a schematic diagram of the 5SDH-4.

The accelerator is equipped with a SNICS (source of negative ions by cesium sputtering) ion source, and can produce a large variety of negative ion beams from solid cathodes. In the source chamber, cesium is heated to form a vapour which is then ionized to form Cs^+ ions. These ions are accelerated towards the tip of the negative biased cathode, where they sputter the cathode material. In our study, pressed powder of Si, Au, and Er_2O_3 were used as sources of Si, Au, and Er (ErO) ions respectively. The sputtered ions are extracted through the centre of the ionizer, focused, and accelerated towards the mass analyzing magnet. Ions with a specific mass-to-charge ratio are selected for implantation using the 90° magnet and the beam is then focused and steered before injection into the high voltage accelerator. This accelerator is a tandem accelerator of "pelletron" design. The negatively charged ions entering the high voltage column are accelerated towards a positive terminal at the centre of the tank. At the terminal, negative ions are partially stripped of electrons and converted to positive ions by passing them through a nitrogen charge-exchange cell. The resulting beam of positive ions is then accelerated from the terminal towards the ground potential at the end of the column. The beam is then filtered with a 15° switching magnet, focused and steered. Finally, the electrostatic scanning system ensures that ions are uniformly distributed across a Ta aperture in front of the sample. The implanted ion density is determined from the projected aperture area and the integrated ion charge collected from the sample, and has an uncertainty of ± 5 %. All implantations were performed at room temperature and pressure $\leq 5 \times 10^{-7}$ Torr. A liquid-nitrogen cooled shield was used to minimize hydrocarbon contamination on the sample and crystalline samples were tilted by 7° with respect to the incident beam direction to reduce channeling effects. The concentration depth profiles of the implanted ion species were calculated using Stopping and Range of Ions in Matter (SRIM) Monte-Carlo simulations[3]. The principle and operation of the 175kV ion implanter are similar to the injection stage of the 5SDH-4 accelerator (Figure 2.3).

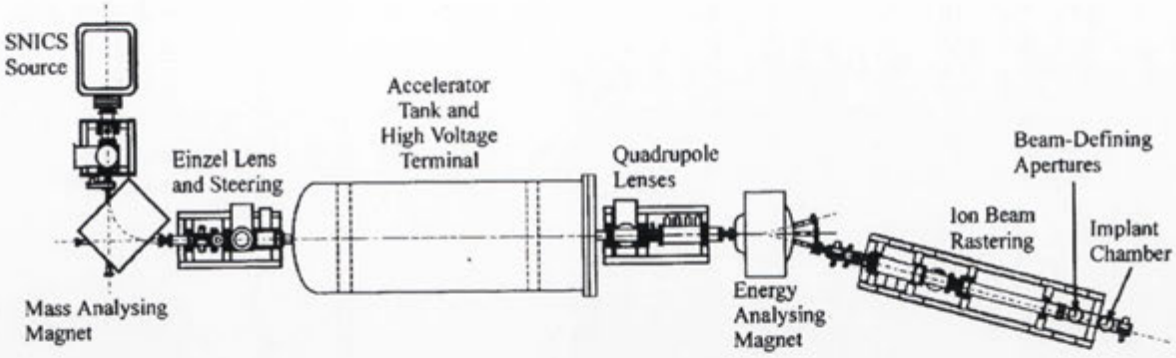

Figure 2.2: ANU 1.7MV tandem accelerator (NEC 5SDH-4).

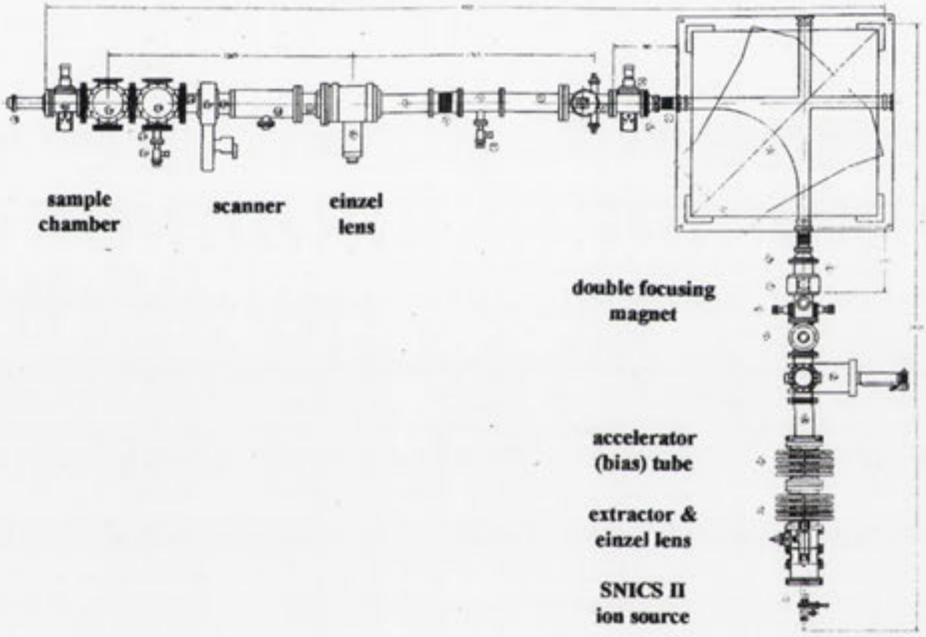

Figure 2.3: ANU 5SDH-4 accelerator.

2.1.3 Sputter system

Sputtering techniques (ATC 2400 UHV) were used to deposit thin films of material onto the sample surface. Figure 2.4 shows a schematic diagram of the ATC 2400 UHV. In the sputter system, ions in a gaseous plasma created by a 13.56 MHz generator are concentrated by magnets onto the source material. The source material is eroded via energy transfer from the arriving ions and ejected in the form of neutral particles –

either as individual atoms, clusters of atoms or molecules. These ejected neutral particles travel in a straight line and deposit on a substrate placed in their path to form a thin film of the source material. The sputter deposition rate is a function of sputter yield of the material, the power density of ions striking the target and nature of the power source (eg. RF or DC). In our study, materials such as Si (RF), Au (DC), Ni (DC) and Er (RF) were deposited on silica, silicon, and the surface of nanowires at normal pressure of 4 mille Torr in an inert Ar environment with a total gas flow of 20 sccm.

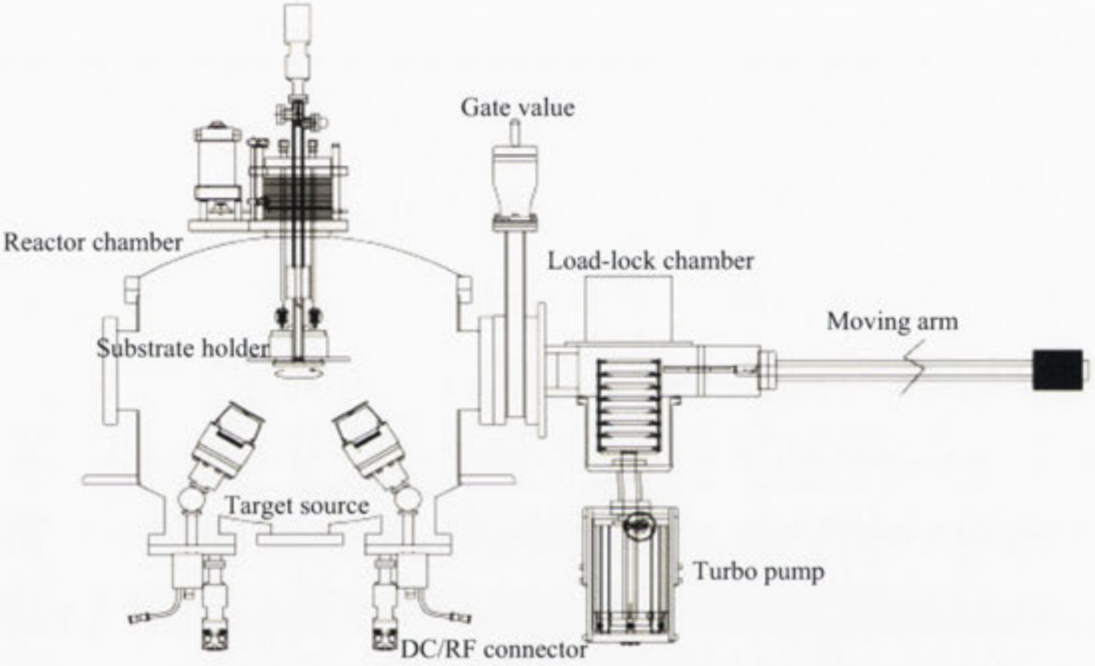

Figure 2.4: A schematic diagram of the ATC 2400 UHV[4].

2.1.4 Thermal annealing

Thermal annealing was used extensively in this project to study hydrogen loss and changes in the mechanical properties of SRO films, and to grow, modify and functionalize various nanostructures. Appropriate annealing times and temperatures were required for each of these results. Thermal annealing was carried out in a conventional horizontal single-zone quartz-tube furnace (Lindberg 1500°C) under flowing Ar, N_2, and O_2 gas. The gas was passed through a moisture-absorbing filter before entering the furnace. When being placed in the tube, the samples were usually in a quartz boat pushed slowly into a pre-heated furnace using a quartz rod. Depending on the temperature this typically occurred over a period of 15-30 seconds. The samples were removed from the furnace tube by slowly pulling them from the hot-zone of the furnace. This also took 15-30 seconds, depending on the temperature.

2.2 Sample imaging

The surface morphology of the samples was investigated using an optical microscope and scanning and transmission electron microscopes (SEM and TEM).

2.2.1 Scanning Electron Microscopy

Most SEM images were obtained using a Hitachi S4300 Schottky Field Emission SEM equipped with an energy dispersive x-ray detector (INCA Energy 350 EDXA system) with an accelerating voltage of ~5-10kV and a working distance of ~5-15mm. In some cases, a Hitachi S4500 Field Emission SEM was also used for imaging of selected samples. Imaging was performed in both secondary electron and backscattered electron modes. The latter provides high atomic-number contrast and was used to clearly distinguish the spatial distribution of heavy elements, such as Au and Er, in silica matrices. The technique is described in detail in standard textbooks[5].

2.2.2 Transmission Electron Microscopy (TEM)

Transmission electron microscopy was performed using a Philips CM 300 TEM operating at an accelerating voltage of 300kV. Standard bright-field and dark-field conditions as well as diffraction patterns were used in our study. The TEM was also equipped with an energy dispersive x-ray detector (EDAX detecting unit) for quantitative analysis of the sample.

For preparing cross-sectional TEM samples of nanowires, a novel XTEM sample preparation method using epoxy resin was employed. As-grown nanowires with or without a substrate were infiltrated under vacuum with a vacuum compatible epoxy resin. The cured resin block was then set up in a Reichert Ultracut Microtome equipped with a Diatome diamond knife. This was used to cut thin sections of materials from the sample surface without contacting the silicon substrate. Sections were cut at approximately 70nm thickness and then mounted on 200 mesh perforated carbon support grids.

2.2.3 Dual beam Focused Ion beam

Cross-sectional SEM images of thin film cracks and some XTEM sample preparation was performed on the XT Nova Nanolab 200 dual-beam focused ion beam (FIB) system at the Electron Microscope Unit of the University of New South Wales. Ion milling was performed with a 30 keV Ga^+ ion beam and imaging performed in secondary electron mode. A schematic of the milling process is shown in Figure 2.5. Before milling, a platinum thin film was deposited on the surface of the sample to protect it from incidental ion milling damage.

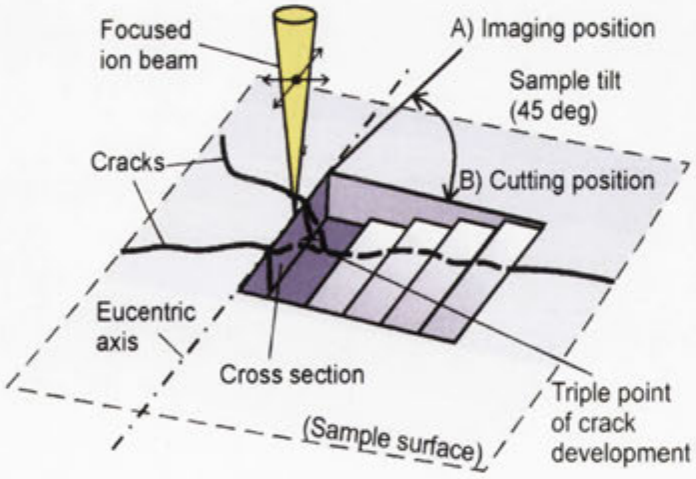

Figure 2.5: A schematic illustration of the dual beam Focused Ion Beam process.

2.3 Other sample characterization techniques

A range of other sample characterization techniques was employed as part of this study. Many of these are discussed in detail elsewhere. The main purpose of this section is to identify the instruments used for particular measurements so that the capabilities and limitations of the techniques can be assessed.

2.3.1 Nanoindentation

The hardness and reduced elastic modulus of thin films was measured using a Hysitron Tribo Indenter (see Figure 2.6) at the ANU. The measurements were performed using three-sided pyramidal (Berkovich) tips and the data extracted from the elastic response region of the force vs penetration-depth measurement[6].

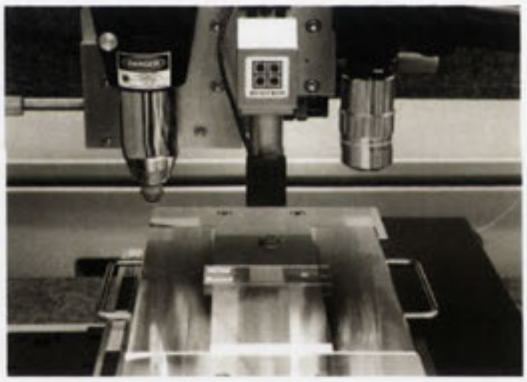

Figure 2.6: Image of Hysitron Tribo indenter[7].

2.3.2 Heavy-Ion Elastic Recoil Detection

The composition of silicon-rich oxide films, including the hydrogen content, was determined by Heavy-Ion Elastic Recoil Detection (HI-ERDA, National Heavy Ion Facility at the ANU[8]) using a custom designed position-sensitive gas-ionization detector, as detailed elsewhere[9-11]. The analysis was performed with 200MeV gold primary ions.

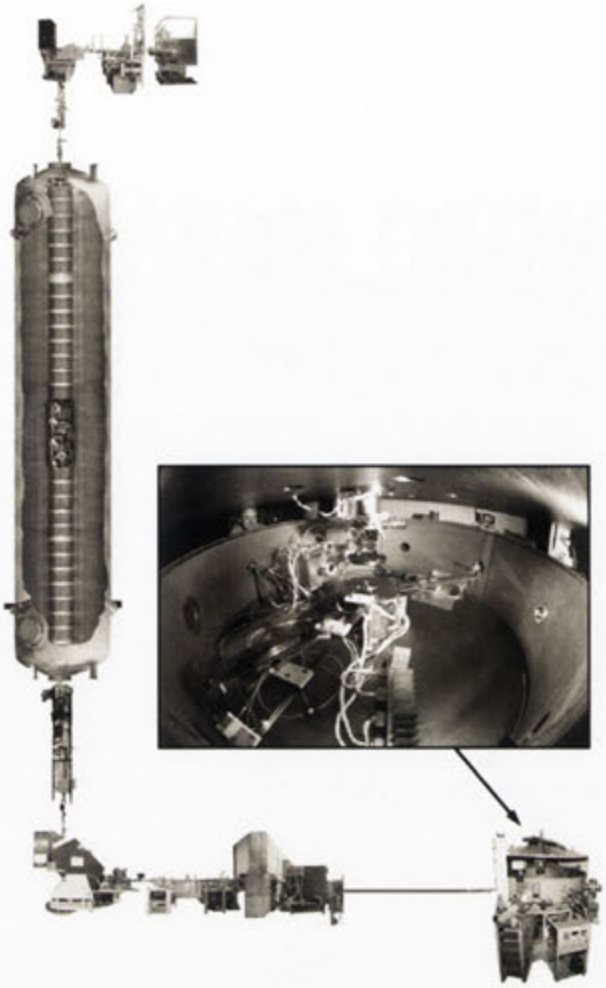

Figure 2.7: Image of Heavy-Ion Elastic Recoil Detection (HI-ERDA, National Heavy Ion Facility at the ANU).

2.3.3 Stress measurement

The thin film stress was determined from wafer curvature measurements using the Stoney equation[12] :

$$\sigma = \frac{E_s}{6(1-\nu_s)} \frac{t_s^2}{t_f} (\frac{1}{R_1} - \frac{1}{R_o}) \quad (2.1)$$

Where σ is the stress in the film, E_s and ν_s are the substrate's modulus of elasticity and Poisson ratio, t_s and t_f are the thickness of the substrate and the film, and R_1 and R_o are the radius of curvature for the stressed and unstressed wafer.

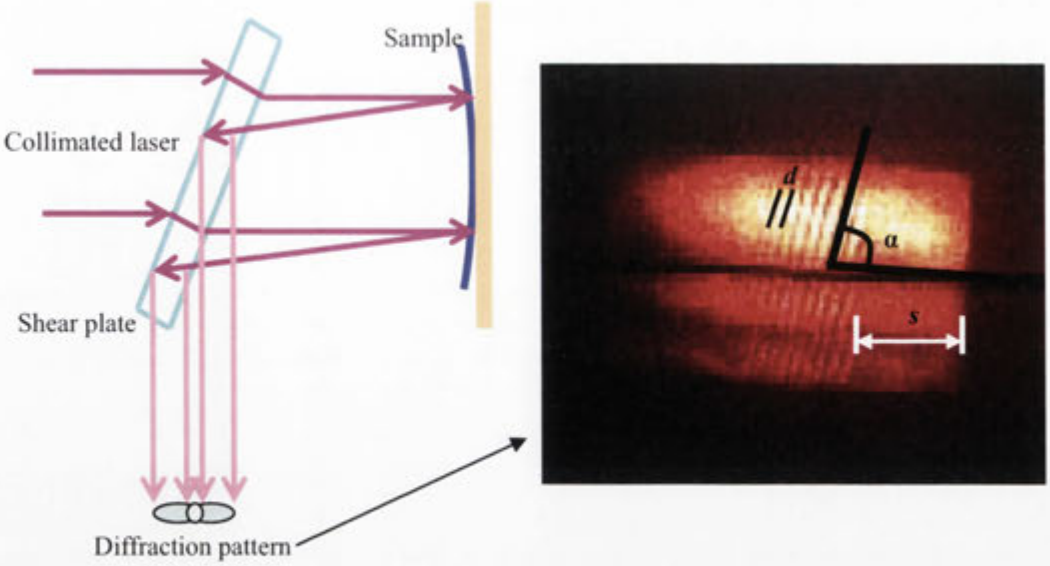

Figure 2.8: A schematic diagram of a shear plate[13] and image of resulting diffraction pattern.

Curvature measurements were made using an optical shear plate to create an interference pattern between a reference beam and light reflected from the sample surface, as shown in Figure 2.8.

For a set of plane waves incident on the shear plate, the interference fringes spacing (*d*), laser wavelength (λ), index of the shear plate (*n*), and the angle of the fringes (α) are related by:

$$d = \frac{\lambda}{2n\alpha} \qquad (2.2)$$

And the wavefront radius on the screen will be given by:

$$R = \frac{Sd}{\lambda \sin(\alpha)} \qquad (2.3)$$

Where *S* is the 'shear' (the distance between the two images) and the fringe spacing is measured perpendicular to the fringe direction using the radius of curvature *R* of the reflected wavefront. The radius of curvature of the sample R_{sample} can then be determined by:

$$R_{sample} = 2(R \pm L) \qquad (2.4)$$

where L is the distance between the sample and the screen. The positive sign indicates a diverging beam (concave sample) while the negative sign is a converging beam (convex sample).

2.3.4 Photoluminescence

Photoluminescence measurements[14] were performed on nanowire samples to study intrinsic (defect-related) luminescence and Er-based luminescence. Measurements were performed on a custom built instrument, as shown in Figure 2.9. An Ar^+ ion laser operating at 488nm was used as the excitation source and luminescence emission was analyzed with a Triax 320 spectrometer equipped with a high-sensitivity liquid-nitrogen cooled germanium detector (for infra-red wavelengths). The excitation laser was mechanically chopped at 15Hz and standard lock-in amplifier techniques were employed to collect the spectra.

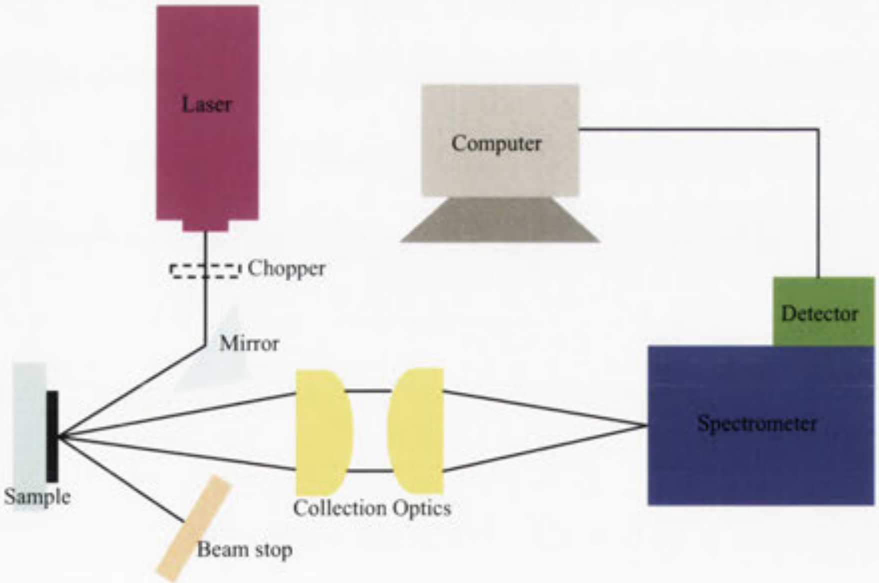

Figure 2.9: A schematic diagram of the PL system.

2.3.5 Optical absorption spectroscopy (Cary-5000 system)

Optical absorption spectroscopy (Cary-5000) was used to study the optical absorption characteristics of nanowires and hybrid nanowire/metal structures. Measurements were performed on a Cary-5000 system using a R928 photomultiplier tube to detect visible and UV light as well as a cooled PbS photocell for near infra-red measurement. The system was used in both reflection and transmission mode over the wavelength range 300 to 1200nm.

2.4 References

[1] P. N. K. Deenapanray, H. H. Tan, J. Lengyel, A. Durandet, M. Gal, C. Jagadish, *IEEE Optoelectronics and Microelectronics Materials Devices Proceeding* **1998**.

[2] *OXFORD Plasmalab 80 Plus System Manual* **1996**.

[3] J. F. Ziegler, J. P. Biersack, U. Littmark, *Paragon Press, New York* **1985**.

[4] *ACT 2400 UHV Sputter System Manual* **1999**.

[5] J. Goldstein, *Scanning Electron Microscopy and X-ray Microanalysis* **1992**, *Plenum Press, New York*.

[6] N. Sneddon, *International Journal of Engineering Science* **1965**, *3(1)*, 45.

[7] http://www.hysitron.com, *last access 05/2009*.

[8] H. Timmers, R. G. Elliman, G. R. Palmer, T. R. Ophel, D. J. O'Connor, *Nuclear Instruments & Methods in Physics Research Section B-Beam Interactions with Materials and Atoms* **1998**, *136*, 611.

[9] H. Timmers, R. G. Elliman, T. R. Ophel, *Nuclear Instruments & Methods in Physics Research Section a-Accelerators Spectrometers Detectors and Associated Equipment* **2000**, *447*, 536.

[10] H. Timmers, T. D. M. Weijers, R. G. Elliman, *Nuclear Instruments & Methods in Physics Research Section B-Beam Interactions with Materials and Atoms* **2002**, *190*, 393.

[11] H. Timmers, T. D. M. Weijers, R. G. Elliman, T. R. Ophel, *Application of Accelerators in Research and Industry* **2001**, *576*, 487.

[12] G. G. Stoney, *Proceedings of the Royal Society of London* **1909**, *A82*, 172.

[13] M. W. Grindel, *Testing Collimation Using Shearing Interferometry.* **2004**.

[14] T. H. Gfroerer, *in Encyclopedia of Analytical Chemistry, edited by R. A. Meyers (Wiley, Chichester, 2000).*

Chapter 3

Mechanical properties of silicon rich oxide films and their applications

This chapter presents data on the mechanical properties of SiO_xN_y:H films, which are one type of SRO film, and their use as materials for non-volatile memory applications and as active substrates for nanowire growth. This work was undertaken as an extension of earlier studies and does not attempt to present a detailed investigation of SiO_xN_y:H films but rather to report some of the more significant supplementary results that came out of this work. The results on nanowire growth were unexpected and laid the foundation for the main work reported in this thesis. This is presented in Chapters 4 and 5.

3.1 Introduction

Dielectric thin films are employed extensively in modern microelectronic, optoelectronic, photonic and micro-electromechanical devices where they are variously used as insulating layers, waveguides, mirrors and mechanical components such as beams and membranes[1-4]. The most commonly used deposition technique for such films is Plasma-enhanced chemical vapour deposition (PECVD) and depending on deposition conditions, such as wafer temperature, gas flow ratios, radio frequency (RF) and RF power, and chamber pressure, the mechanical properties of thin films can be controlled. In general, it is accepted that these films may include several impurities such as hydrogen and nitrogen diluted into SiH_4 plasma[5]. As deposited films typically exhibit compressive stress, which is detrimental for the preparation of large area devices[6]. The fabrication of devices and structures also often requires thermal processing of the films which can lead to changes in mechanical properties of the films[7, 8]. In extreme cases these changes can lead to film failure by delamination or cracking. Various cracking mechanisms have been studied by Hutchinson and Suo[9, 10]. In general, the driving force for crack propagation is the elastic energy reduction associated with the crack and the crack resistance is the energy needed to advance the crack. When the energy released by crack propagation is less than the resistance, no cracks propagate in the film. On the other hand, if the energy release is larger than the crack resistance, cracks nucleated at a flaw will propagate in the film. For cracks which extend through the film thickness only and leave the interface and substrate intact, the crack propagates laterally in the film after reaching the interface, until it reaches a film edge or another flaw or crack. However, depending on the film stress and the mechanical properties of the film and substrate, the crack may penetrate into the substrate or bifurcate onto the interface (interface debonding), as shown in Figure 3.1[10].

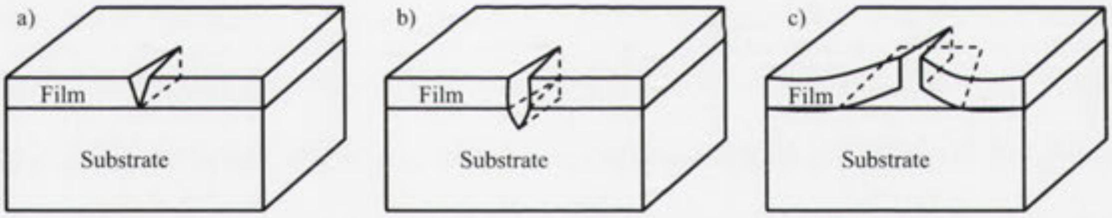

Figure 3.1: a) a film cracking, b) substrate penetration, and c) interface debonding[10].

Clearly, knowledge of the thermal stability and material properties of dielectric thin films and their connection with the electrical properties and the evolution of structures are very important for their practical use. Silicon rich oxide (SRO) film have been extensively studied and characterized due to their potential use in optical and electrical applications[3, 11-14]. These films are also often used as passivation layers and intermetal level dielectrics and are widely used in microelectronic devices, such as dynamic and static random access memories, CMOS transistors[15-19]. Such films are often deposited by plasma enhanced chemical vapor deposition (PECVD) because this process offers ready control of the film composition, good adhesion to the substrate, and low-densities of deposition defects.

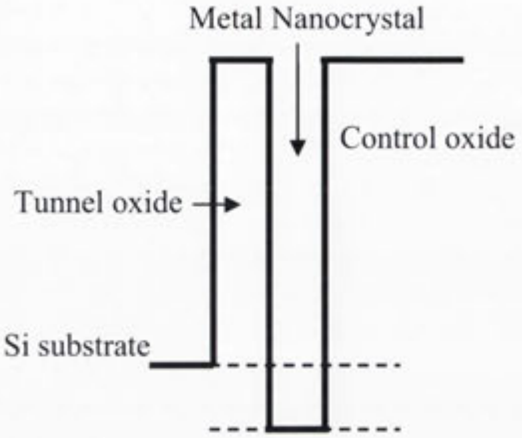

Figure 3.2: Energy band diagram for an embedded metal induced nanocrystal between a control oxide and a tunnel oxide (d_{eff} is the effective potential well depth).

Depending on the deposition conditions, SRO films include impurities such as hydrogen and nitrogen. The excess Si in the film plays an important role in determining its electrical properties including charge trapping[20] and carrier transportation[21, 22]. It can also be used to produce silicon nanocrystals (Si-NCs) in the film by high temperature annealing[23]. In this process, the deposited homogeneous SRO film is changed to a biphasic material, in which Si-NCs are dispersed in an amorphous matrix[24]. Metal-insulator-silicon (MIS) structures containing semiconducting NCs embedded in dielectric materials have been of particular interest with regard to their potential use in electronic devices such as single electron transistors and non volatile memory devices[25, 26]. In such devices, where floating gates are not electrically continuous but distributed into NCs, charge loss through lateral paths is suppressed so that, contrary to the standard floating gate flash electrically erasable programmable read-only memories, very small tunneling oxide thickness and low voltage operation can be used[27]. SRO films are the most compatible material in which Si-NCs as well as metal induced nanocrystals (M-NCs) can be contained. The memory effect of M-NCs was found to be more pronounced than those of the semiconductor NCs. The M-NCs memory devices possess several advantages such as stronger coupling with the conduction channel, a wide range of available work functions, and bigger density of states around the Fermi level and smaller perturbation due to carrier confinement[28]. The following sections present an overview of the mechanical properties of SRO films and their applications.

3.2 Experimental details

Different crystallographically orientated Si wafers and thermally grown SiO_2 with different thickness (2~180nm) were employed as substrates for thin film deposition. Thin SiO_xN_y:H films were deposited on each particular substrate by PECVD using an Oxford Instruments PlasmaLab 80 system. SiH_4 (diluted to 5% with hydrogen) was used as a gas source of silicon and N_2O was used as a source of oxygen. Other process conditions were kept constant: 1 Torr process pressure, 300°C substrate temperature, and 20W RF power. The composition of the films was varied by controlling the ratio of the SiH_4 and N_2O gases. This was achieved by holding the SiH_4 flow rate at a fixed value of 160 sccm and varying the N_2O flow rate between 25-710 sccm.

Heavy ion elastic recoil detection (HI-ERD) was employed to measure the composition of films, including the hydrogen content. These measurements were undertaken with 200 MeV Au primary ions produced by the 14UD pelletron accelerator at the Australian National University. The composition of as-deposited films is shown in Table 3.1 for different N_2O flow rates.

After deposition, samples were annealed at temperatures in the range from 400 to 1100°C using a quartz-tube furnace with N_2 ambient for 1hour. The effect of ion-implantation on film failure was assessed by irradiation of selected samples over half their area with 400 keV Si^+ ions prior to annealing and comparing the crack behaviors between implanted and unimplanted regions. All annealed samples were examined by optical microscopy and/or scanning electron microscopy (SEM) and selected samples were examined in cross section using an FEI Dualbeam FIB system. The 3-dimensional optical profile of surface structure and roughness of the selected sample was performed on selected samples by optical profiler (Wyko NT9100 Optical profiling system).

Table 3.1: Composition of the materials as determined by heavy ion ERD.

Material	N_2O (sccm)	[Si] (at %)	[O] (at %)	[N] (at %)	[H] (at %)
$SiO_{2.13}N_{0.05}$:H	710	26.6	56.6	1.3	15.2
$SiO_{1.42}N_{0.25}$:H	75	29.1	41.4	10.5	18.8
$SiO_{1.16}N_{0.32}$:H	50	30.7	35.6	11.4	22.1
$SiO_{0.85}N_{0.35}$:H	35	35.2	29.8	10.4	24.4
$SiO_{0.65}N_{0.44}$:H	25	37.2	24.0	10.6	27.9

Hardness testing was performed with a Hysitron TriboIndenter using three-sided pyramid (Berkovich) tips. The film stress was calculated from wafer curvature measurements using the Stoney equation[29]. High-frequency C-V measurements were performed by using an Agilent 4284A C-V meter with a frequency of 1MHz and a modulation signal amplitude of 100mV.

For metal induced nanostructures, nickel with a thickness of 10nm was deposited on SRO films and subsequently annealed in the furnace system at 800, 900, and 1100°C with N_2 ambient for 1 hour. Cross-sectional TEM images of metal induced structures were acquired in bright-field mode using a Philips CM300 FEI microscope and 300keV electrons. The chemical composition was analyzed by energy dispersive x-ray spectroscopy (EDX) using an energy dispersive spectrometer attached to the TEM instrument.

3.3 Experimental results

3.3.1 Film stress, hardness and hydrogen content

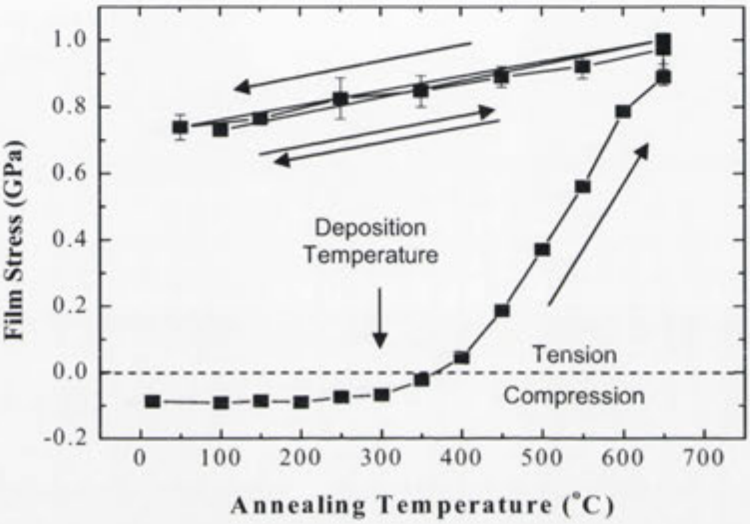

Figure 3.3: Stress evolution as a function of annealing temperature for a 1.2μm thick $SiO_{1.16}N_{0.32}$:H film deposited onto (100) Si by Plasma-enhanced chemical vapour deposition (PECVD) with the substrate heated to 300°C. Measurements were performed in situ as the sample was heated in air and data are shown for two complete heating and cooling, as indicated by the arrows.

Figure 3.3 shows the film stress in a 1.2 μm thick $SiO_{1.16}N_{0.32}$:H film deposited onto (100) Si during in-situ annealing in air at temperatures in the range from room temperature to 650°C. The as-deposited film exhibits a compressive stress of around 90MPa at room temperature. As the annealing temperature increases above 300°C (deposition temperature), the compressive stress decreases and at higher temperatures becomes increasingly tensile. The maximum tensile stress of approximately 1GPa is reached at an annealing temperature of 650°C. Once annealed to this temperature, relatively small and reversible changes of stress were consistently induced by the cooling and heating cycle of the sample due to differential expansion and contraction of the film and substrate. The increase in tensile stress reported in figure 3.3 is correlated with a loss of hydrogen from the film, up to 30 atomic percent of that which was unavoidably incorporated in the film during PECVD deposition (Table 3.1). Similar results have previously been reported and attributed to hydrogen release during network reordering[30-33].

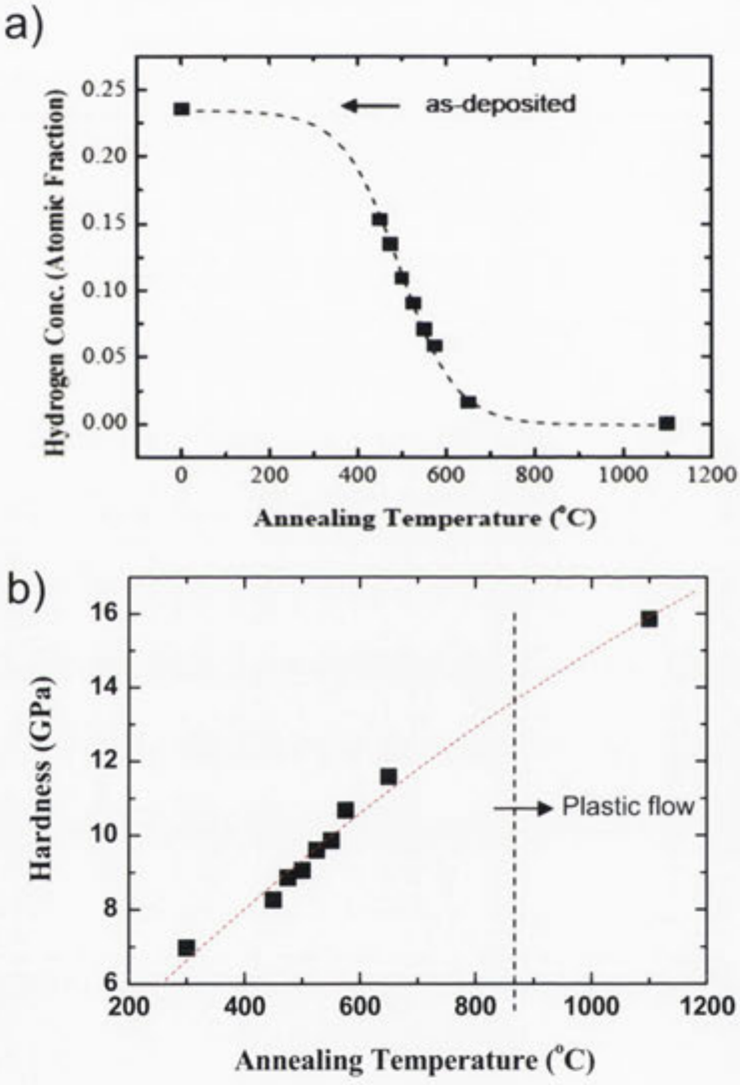

Figure 3.4: a) Hydrogen concentration and b) hardness of a $SiO_{1.16}N_{0.32}$:H film as a function of annealing temperature. Samples annealed in a quartz tube furnace with a flowing N_2 ambient.

Figure 3.4 shows the hydrogen concentration and hardness of a $SiO_{1.16}N_{0.32}$:H film as a function of annealing temperature. The data in Fig. 3.4 a) shows that hydrogen desorbs from the film over the temperature range 350-650°C. Comparison with the data in Fig. 3.4 b) shows that this is correlated with an increase in the hardness of the film, from around 6 to 12 GPa, over the same temperature range. As the hardness is directly related to the density of the film, this shows that network reordering, and the associated hydrogen release, are correlated with densification of the film. It should however be noted that additional processes such as elastoplastic flow[34] are expected to contribute to densification above about 850°C. Similar behaviour is observed for other SiO_xN_y:H films, although the magnitude of the stresses varies with composition. Clearly, accurate modeling of this behaviour could be used to predict particular states of stress, including the processing conditions required to produce zero-stress films.

3.3.2 Film failure and substrate damage

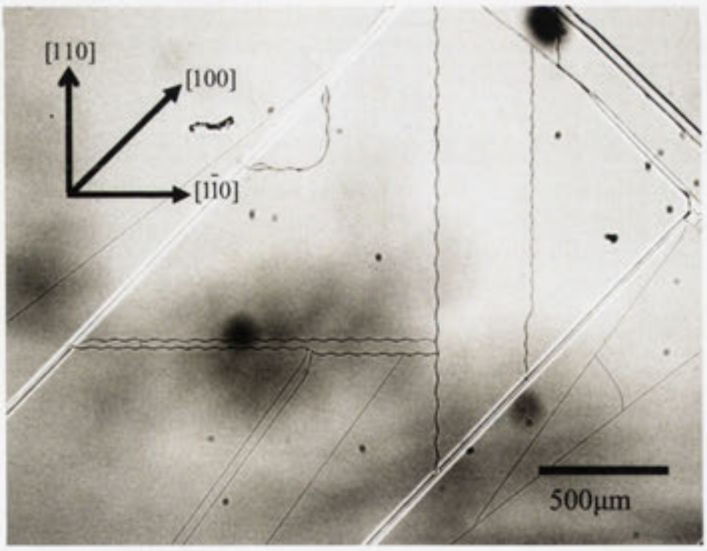

Figure 3.5: The optical micrographs show typical crack patterns for two distinct modes of crack propagation; straight and oscillating cracks.

The high levels of tensile stress observed in films annealed at temperatures around 500-600°C can result in film failure and damage to the Si substrate. The resulting cracks are also found to have a complex morphology that depends on the film thickness and sample structure. As an example, Figure 3.5 shows an optical micrograph of the crack patterns observed in a 1.2µm $SiO_{1.16}N_{0.32}$:H layer deposited onto a (100) Si substrate after annealing to 1100°C. Two distinct crack propagation modes are observed: (a) straight cracks propagating parallel to <001> directions in the Si substrate and (b) oscillating cracks, a novel mode of propagation, parallel to the <011> orientation in the Si substrate. The oscillating cracks are particularly interesting as they propagate over centimetre distances with near-constant period and amplitude. As the oscillation period is of the order of 100µm, this represents hundreds of oscillation cycles, indicative of a highly stable mode of crack propagation. Moreover, the fact that oscillating cracks propagate between straight cracks suggests that the latter form first, i.e. at lower tensile stress (lower annealing temperatures), and that the oscillating cracks form only at relatively high tensile stresses (higher annealing temperatures).

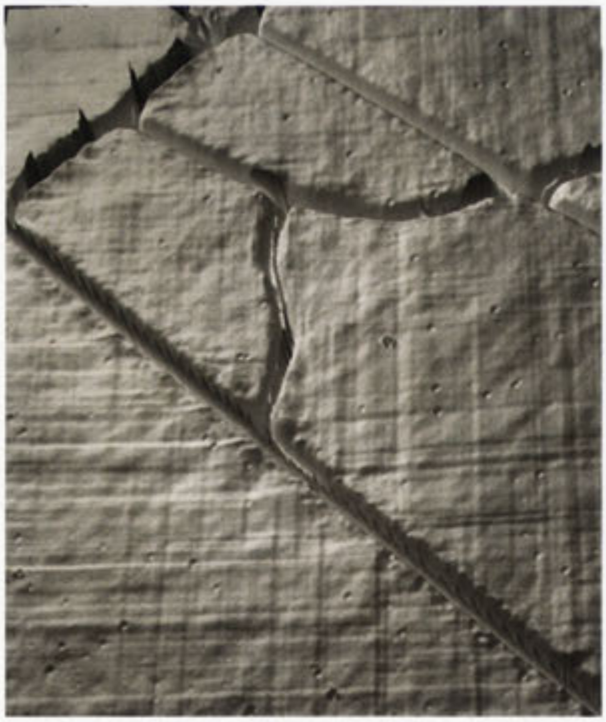

Figure 3.6: The optical profiler image of the dislocation network formed in the silicon substrate by the tensile stress in a $SiO_{1.16}N_{0.32}$:H layer after annealing at 1100°C.

Closer examination of the sample surface reveals a network of other defects residing between the cracks, as shown in Figure 3.6. This image from an optical profiler shows dense network of linear features running parallel to the <011> directions of the silicon substrate. This pattern is characteristic of misfit dislocations in the silicon substrate (The principal slip system in silicon is in the <110> direction on (111) planes) and is believe to result from the high tensile stress in the $SiO_{1.16}N_{0.32}$:H film and its strong adhesion to the silicon substrate. Such defects do not form at room temperature, where Si is essentially elastic, but are commonly observed during annealing of Si/GeSi strained-layer heterostructures and during the oxidation of silicon where the stresses are similar to those studied here. (Silicon nitride films were found to delaminate, rather than crack, as a consequence of their poorer adhesion).

Despite their excellent adhesion, once cracked, SRO films delaminate in the presence of water vapour[35, 36]. Susceptible samples left in a laboratory atmosphere undergo such delamination over a period of several days, with the films delaminating from the edge of the cracks.

3.3.3 Phase diagram of crack formation

The stability of films and the mode of crack propagation were found to be a sensitive function of the film composition, thickness and annealing temperature. Figure 3.7 summarizes the general modes of crack propagation observed in $SiO_{1.16}N_{0.32}$:H and $SiO_{0.84}N_{0.3}$:H films as a function of film thickness and annealing time. The data for $SiO_{1.16}N_{0.32}$:H films (Figure 3.7 a)) shows that no cracks are observed in films with a thickness of less than 0.6μm or for any thickness film annealed at less than 450°C for 1 hour. In contrast, only straight cracks are observed in films with thicknesses between 0.6 ~ 1.1μm when annealed above 450°C, while both straight and oscillating cracks are exhibited in the films with thicknesses between 1.1 ~ 1.4μm when heated to temperatures above 550°C.

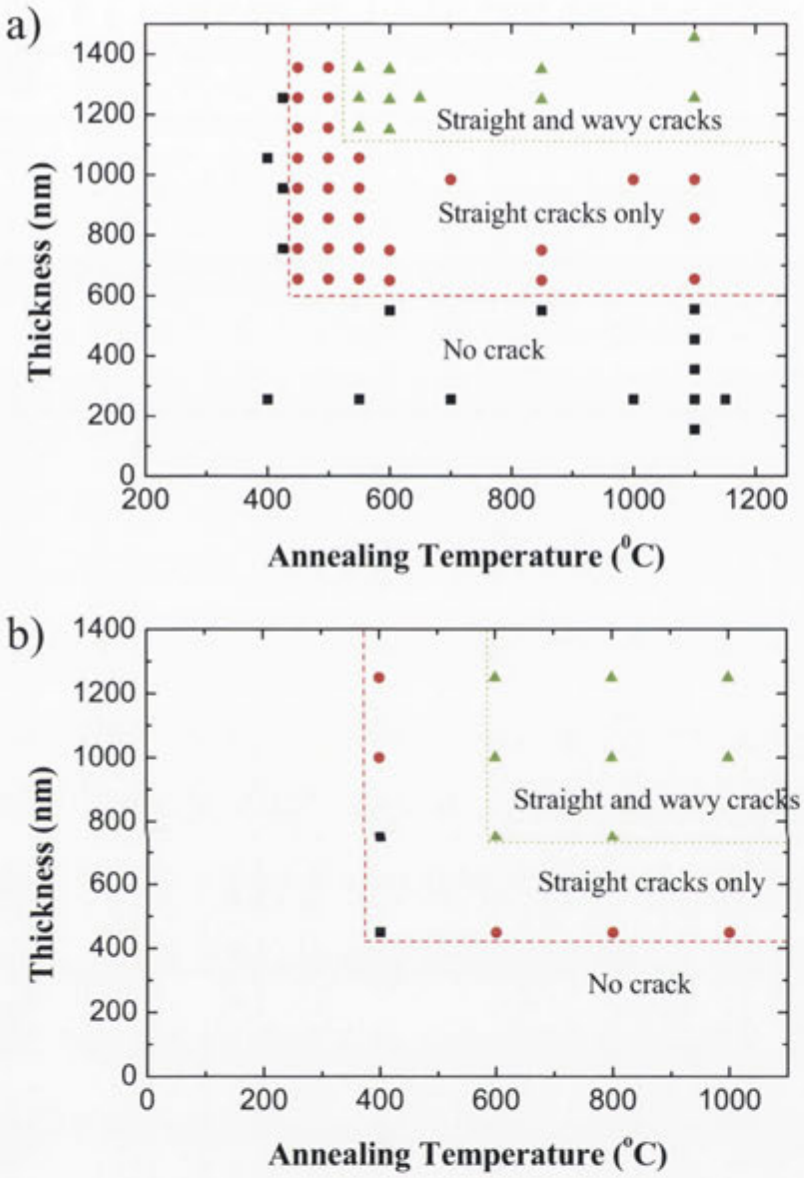

Figure 3.7: Phase diagram of crack formation depending on film thickness and annealing temperature a) $SiO_{1.16}N_{0.32}$:H film and b) $SiO_{0.84}N_{0.3}$:H film (Rectangular: no crack, circle: straight crack, and triangle: straight and wavy crack).

The data for the $SiO_{0.84}N_{0.3}$:H films (figure 3.7 b), is slightly more scattered but both straight and oscillating cracks are observed in the films with thicknesses between 0.75 ~1.25μm when annealed above 600°C. As the film stress increases with increasing film thickness and increasing annealing temperature it can be concluded from the data in Fig. 3.7 that the propagation of oscillating cracks requires higher stress than that required for the propagation of straight.

3.3.4 Substrate orientation dependence

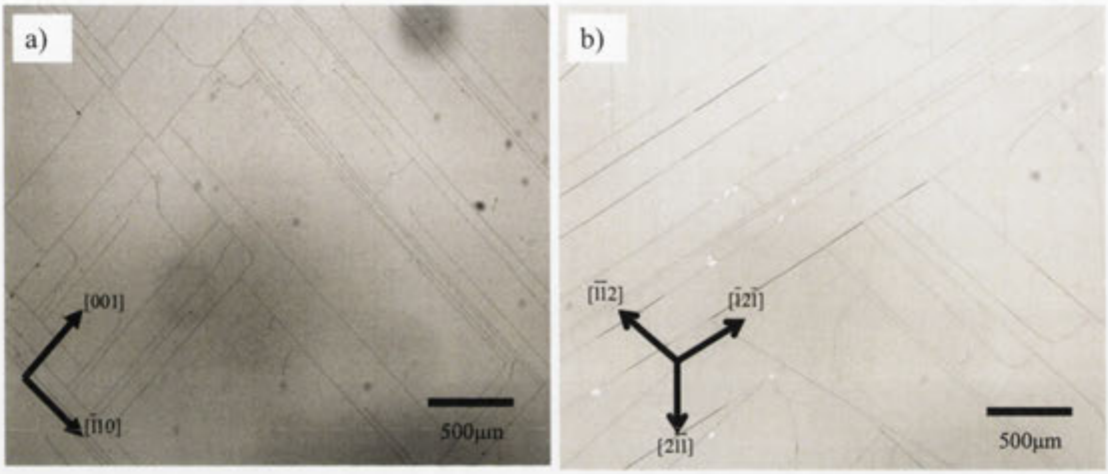

Figure 3.8: Optical microscopy images of crack formation on 1.2 μm thickness $SiO_{1.16}N_{0.32}$:H films onto a) (110) oriented Si and b) (111) oriented Si substrate after annealing at 600°C in N_2 for 1hour.

As discussed in the previous section, the mode of crack propagation depends on the film thickness and processing temperature. Because the two modes of crack propagation are aligned with specific crystallographic directions in the silicon substrate they are also expected to depend on the crystallographic orientation of the substrate. Figure 3.8 shows optical microscopy images of crack formations in 1.2μm $SiO_{1.16}N_{0.32}$:H films deposited onto (110) and (111) oriented substrates after annealing at 600°C in N_2 for 1hour. In contrast to films on (100)-oriented Si, only straight cracks are exhibited in both samples. i. e. No oscillating cracks are observed for these samples. The images show that straight cracks propagate in [001] and [011] directions on (110)-oriented Si and in [211] directions in films on (111)-oriented Si. These observations are consistent with previous results for xerogel silica films on silicon in which similarly oriented cracks were observed[37]. They are also roughly consistent with the fact that cracks are expected to propagate perpendicular to the direction of minimum plane-strain elastic modulus which suggests that they should propagate along [110] directions on (100) silicon, along [001] and [110] directions on (110) silicon, and along no particular direction on (111) silicon[38]. In fact, cracks run along the <112> directions on (111) silicon.

3.3.5 The morphology of cracks

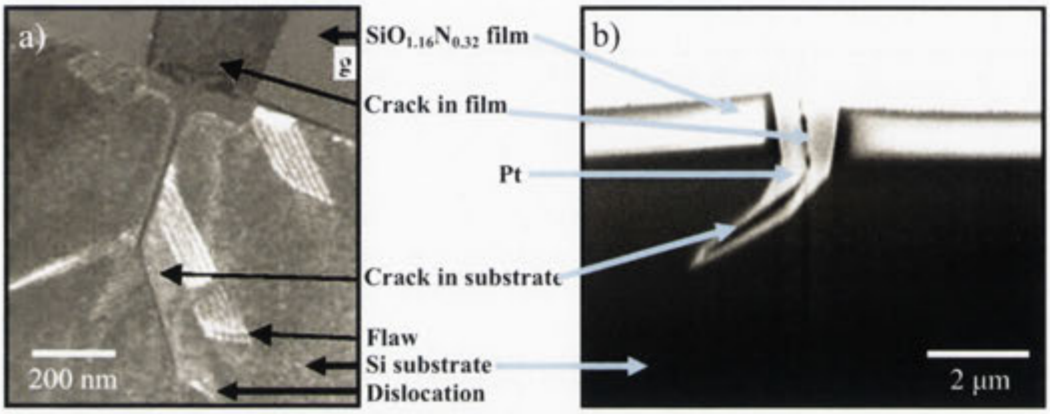

Figure 3.9: a) cross-sectional TEM image of straight crack and b) cross-sectional SEM image (produced by Focused Ion Beam) of oscillating crack propagated on 1.2μm thickness $SiO_{1.16}N_{0.32}$:H films onto (100) oriented Si after annealing at 600°C in N_2 for 1hour.

As discussed above, SRO films deposited onto (100) substrates exhibit two distinct crack propagation modes: straight cracks aligned along [001] directions and oscillating cracks aligned along [011] directions. Fig. 3.9 shows cross-sectional TEM (straight) and SEM (oscillating) images of cracks produced by a 1.2 μm $SiO_{1.16}N_{0.32}$ film after annealing at 600°C in N_2 for 1 hour. Note that these samples were prepared using a Focused Ion Beam (FIB) system, and Pt was used to protect the sample surface. This partially fills the cracks giving rise to the bright contrast in the SEM image. These images reveal that the both cracks extend through the film and into the underlying Si substrate where they follow crystallographic directions. The TEM image also reveals the presence of extended defects in the vicinity of the crack.

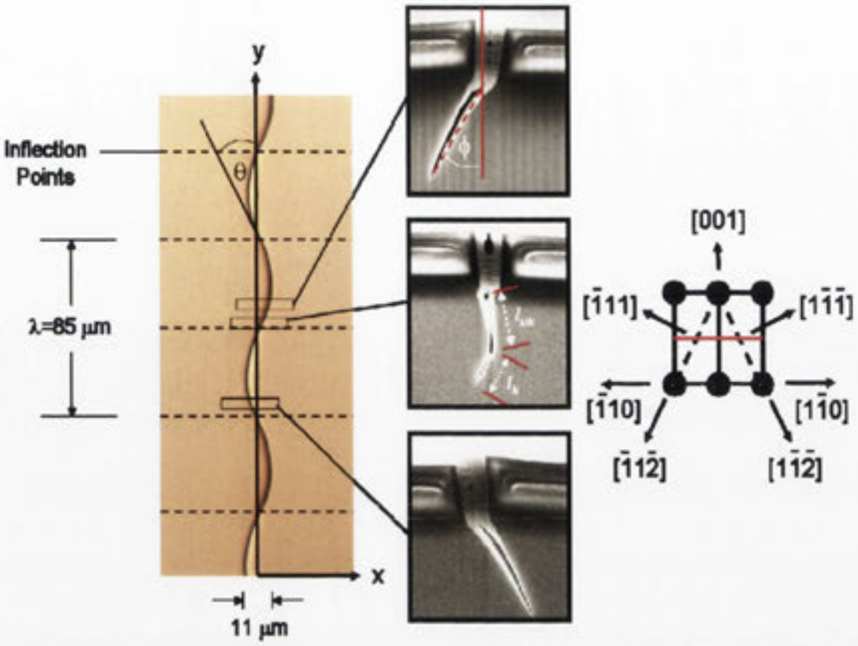

Figure 3.10: Cross-sectional SEM images of an oscillating crack at various positions (indicated by the rectangles) along the crack. Included schematic illustration shows the major crystallographic directions corresponding to the cross-sectional SEM images.

The oscillating cracks show more complex behaviour, as shown in Figure 3.10. Three cross-sectional SEM images taken at various positions along the crack length show that the orientation of the substrate-crack changes along its length. These sections clearly show that the orientation of the substrate crack oscillates between two extreme directions as the in-plane orientation of the crack propagates through half a period. Specifically, the substrate crack oscillates between two symmetric <112> directions (cracks on (111) planes) as the surface crack oscillates about a <011> direction. This complex structure is particularly intriguing given that <011>/(111) is a common slip system in silicon and that it represents a standard cleaving geometry along which linear cracks are known to propagate. Further details of this structure have been presented in reference[39].

3.3.6 The effect of a buffer layer between film and substrate

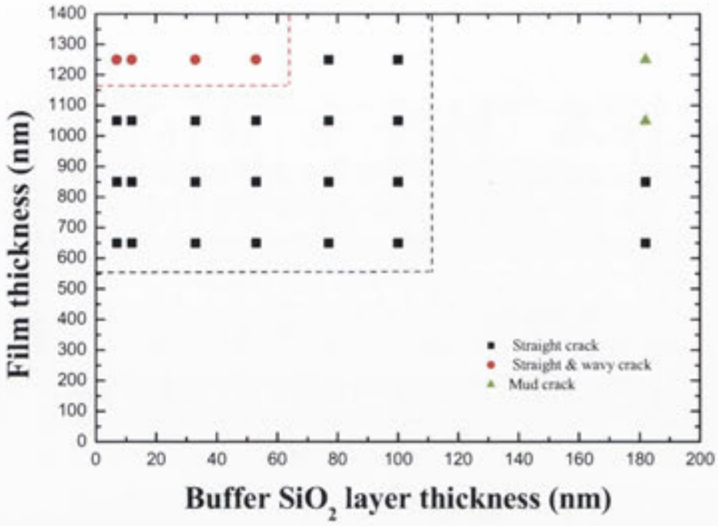

Figure 3.11: The phase diagram of straight and oscillating cracks on 1.2 μm $SiO_{1.16}N_{0.32}$:H film depending on buffer layer thickness after annealing at 600°C in N_2 for 1hour.

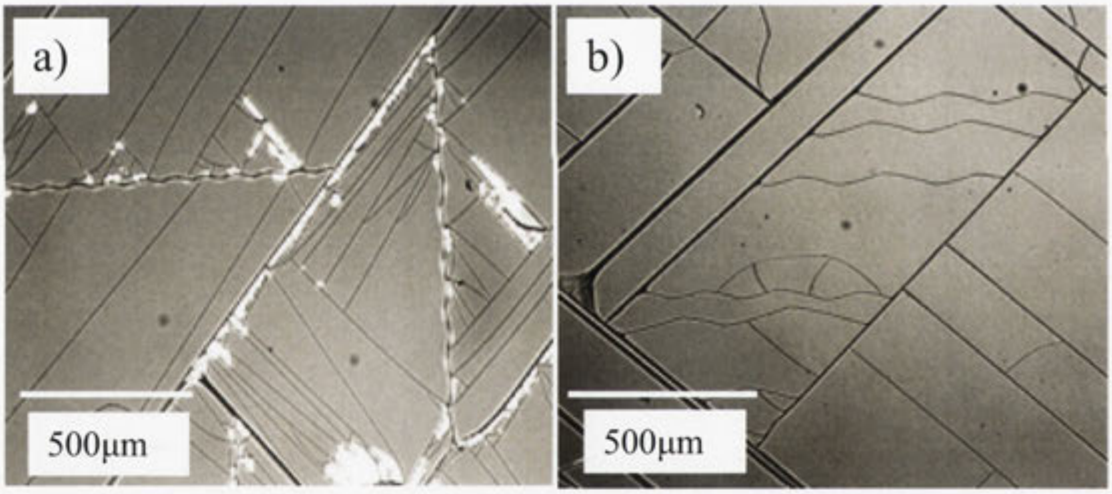

Figure 3.12: Optical microscopy images of $SiO_{1.16}N_{0.32}$ film after 1100°C for 1hour with SiO_2 buffer layer of a) 7nm thickness and b) 50nm thickness between film and substrate.

The propagation of cracks into the substrate clearly influences their form. In order to investigate this interaction, a thermal SiO_2 layer was added as a buffer layer between the SRO film and the Si substrate to decouple the film from the substrate. Figure 3.11 shows the phase diagram of crack formation in a $SiO_{1.16}N_{0.32}$:H film thickness as a function of SiO_2 buffer layer thickness. The samples were annealed at 600°C in N_2 for 1 hour. Both straight and oscillating cracks are observed in SRO films with thicknesses of more than 1.2μm and SiO_2 thicknesses of less than 50nm. Only straight cracks are observed in SRO films with thicknesses of less than 1μm, regardless of the thickness of the SiO_2 layer. Finally, unoriented "mud-crack" patterns were observed for thick (~1 μm) SRO films separated from the substrate by buffer layers with thicknesses around 180nm. In this case the SRO film is effectively decoupled from the substrate and crack propagation is not influenced by the substrate crystallography.

Interestingly, the wavelength and amplitude of oscillating cracks was found to depend on the thickness of the buffer layer, as shown in figure 3.12 (buffer layer with (a) 7nm and (b) 50nm thickness). These results are summarized in Fig. 3.13 which shows that both the wavelength and the amplitude of the oscillating cracks increase with increasing buffer layer thickness. The mechanism by which oscillating cracks propagate remains unclear but it is interesting to note that the increase in wavelength exhibits a $t^{1/2}$ dependence on the buffer layer thickness, t.

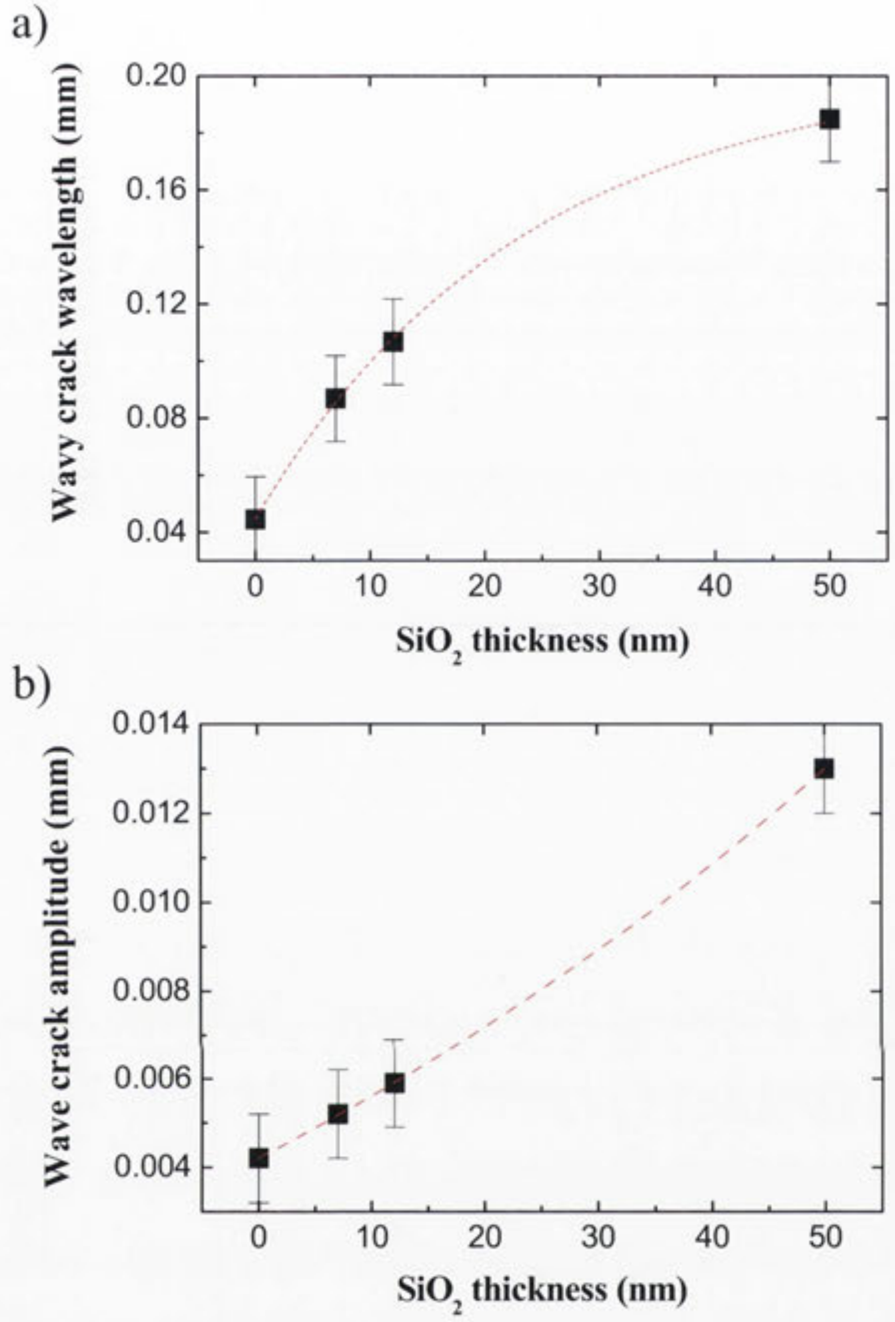

Figure 3.13: a) Wavelength and b) amplitude of oscillating cracks as a function of thickness of SiO_2 buffer layer.

3.3.7 The effect of ion irradiation

Ion irradiation is known that affect the stress in thin films and to improve the adhesion between films and substrates[40]. As a check of whether these effects influence the formation of cracks in SRO films, a 1.2μm thick $SiO_{1.16}N_{0.32}$:H film was deposited onto

(100) Si and part of it was irradiated with 400 keV Si^+ ions to a fluence of 1×10^{16} cm^{-2}. Figure 3.14 shows an optical microscopy image of the interface area between implanted (left) and the unimplanted area (right) after annealing at 600°C in N_2 for 1 hour. The implanted area clearly has a lower density of cracks and less delamination than the unimplanted film. The crack density and extent of delamination decrease with increasing implant fluence. This is consistent with a reduction in residual stress as previously reported for ion-irradiated a-Si:H films deposited by PECVD[40]. Ion-irradiation therefore provides a means of reducing film failure.

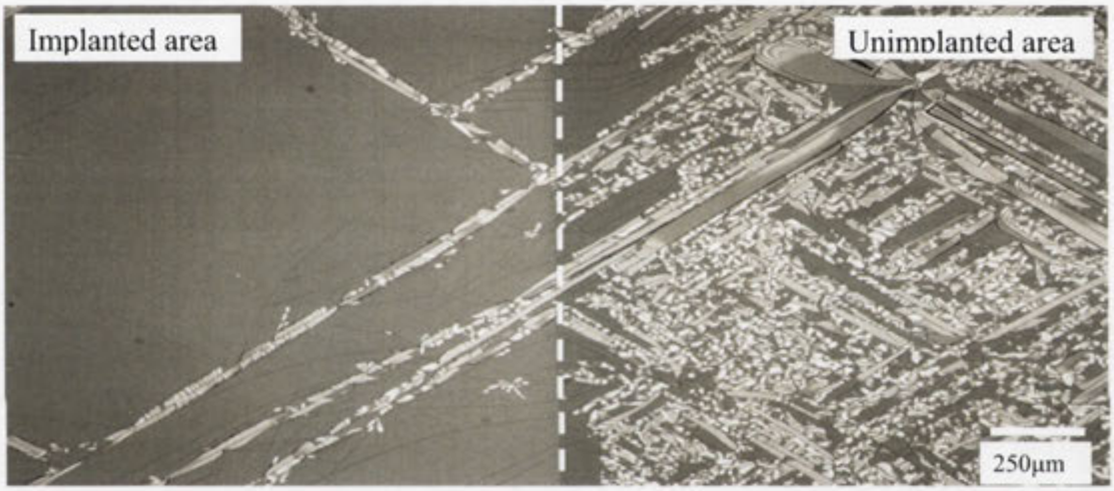

Figure 3.14: Typical optical microscopy image of the interface between Si^+ implanted area (left) and unimplanted area (right) in $SiO_{1.16}N_{0.32}$ film after annealed at 600°C.

3.4 Properties and applications of SRO films

3.4.1 C-V measurement of SRO film

Silicon-oxynitrides are employed in non-volatile memory devices to trap and store charge. The charge traps correspond to defect centres within the dielectric layer and can store the charge for in excess of 10 years. The SRO films employed in the current study also contain significant amounts of nitrogen, as well as hydrogen. The hydrogen desorption kinetics[41, 42], shown in Figure 3.4 a), suggests that much of the hydrogen is tightly bonded to Si, O or N. Its release should therefore introduce defect centres within the SRO film and it should be possible to control the density of such defects by controlling the H release. To test this hypothesis, C-V measurements were performed on samples annealed to different temperatures.

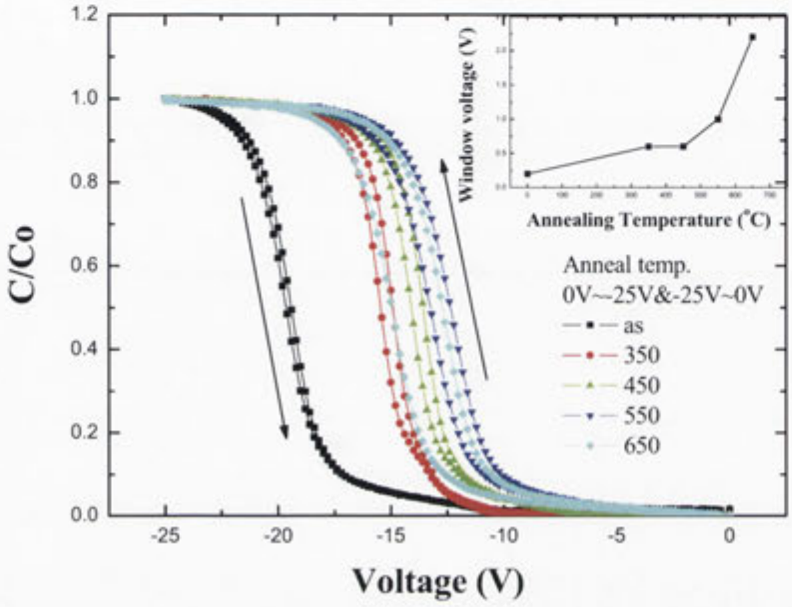

Figure 3.15: The capacitance-voltage (C-V) hysteresis of SRO film annealed at various temperature (0~650°C) after bidirectional sweeps and windows voltages of measured hysteresis verse annealing temperature (inset). Note: Window voltage means FWHM of the measured hysteresis loop.

Figure 3.15 shows normalized capacitance-voltage (C-V) hysteresis curves for a 1.2 μm thick $SiO_{1.16}N_{0.32}$:H film annealed at different temperatures up to 650°C. All measured C-V curves are shifted to negative voltages due to the high fixed positive charge in the film. Indeed, it is well known that silicon oxide/nitride films deposited by PECVD for passivation contain high densities of positive charge[43-45]. However additional charge trapping and detrapped is evident from the magnitude of the hysteresis during the successive voltage sweeps. From the data in Figure 3.15, little or no additional trapping is observed for the as-grown film during voltage sweeps in the range from 0V to -25V and back to 0V. However, after annealing there is a significant positive shift of the flat-band voltage (V_{fb}) and an increase in the hysteresis width of the C-V characteristics. This data is consistent with the annealing of fixed-charge traps and the generation of new traps that can readily be charged and discharged during C-V voltage sweeps[46, 47]. The density of the latter increases with increasing annealing temperature, for temperatures in the range 350 - 650°C and is well correlated with hydrogen release kinetics. This suggests that the increase in hysteresis is due to the trapping of charge at defects generated by hydrogen loss. It is worth noting that the observed hysteresis arises from electron injection from a deep inversion layer in the substrate and holes injection from a deep accumulation layer in the substrate.

The behaviour for samples annealed at 1100°C is shown in figure 3.16. In this case, the C-V characteristics show a greater positive shift of V_{fb} and the decrease of hysteresis width compared with samples annealed at 650°C. At this temperature, hydrogen is completely released and significant annealing of the resulting defects is expected. It is also possible that the SRO film has undergone some phase separation during annealing at 1100°C. This can produce small Si nanocrystallites within the film that act as charge traps[48, 49].

These results demonstrate that the density of charge traps can be controlled by thermal annealing and that these traps are likely produced by H desorption from the film[50, 51]. This conclusion is supported by previous studies of hydrogen passivation and depassivation of Si dangling-bond defects which clearly demonstrated that defects are produced by the H desorption process[52, 53].

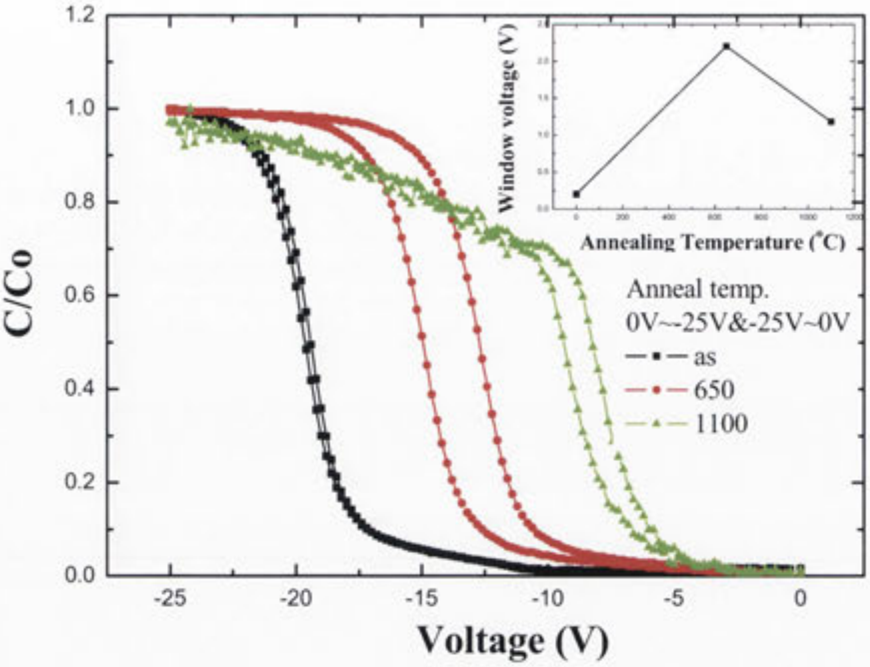

Figure 3.16: The capacitance-voltage (C-V) hysteresis of SRO film annealed at various temperature (0~1100°C) after bidirectional sweeps and windows voltages of measured hysteresis verse annealing temperature (inset).

3.4.2 Metal induced nanocrystals

As mentioned in the introduction, the charge trapping effect of NCs contained in SRO films is of use for non-volatile memory applications and is more stable and faster than conventional film devices[27]. Moreover, discrete charge storage can be applied in special applications such as single electron transistors (SET) and non-volatile memory devices[25, 26]. However, instead of semiconducting (Si or Ge) NCs, metallic (Au, Ag, Pt, and Co) NCs have been extensively investigated due to their additional advantages such as high work functions, low temperature process, easy control of position, etc[28,54]. Here we examine a relatively simple process for producing metal-based nanocrystals in a SRO film. Namely, a metal film is deposited on a SRO film and heated to diffuse the metal into the film where it is expected to react with excess Si to form metal-silicide nanocrystals. This is not possible for SiO_2 films due to the low diffusivity and solubility of metals in SiO_2. But the silicon-rich composition of the current films provides a possible route to achieving this aim.

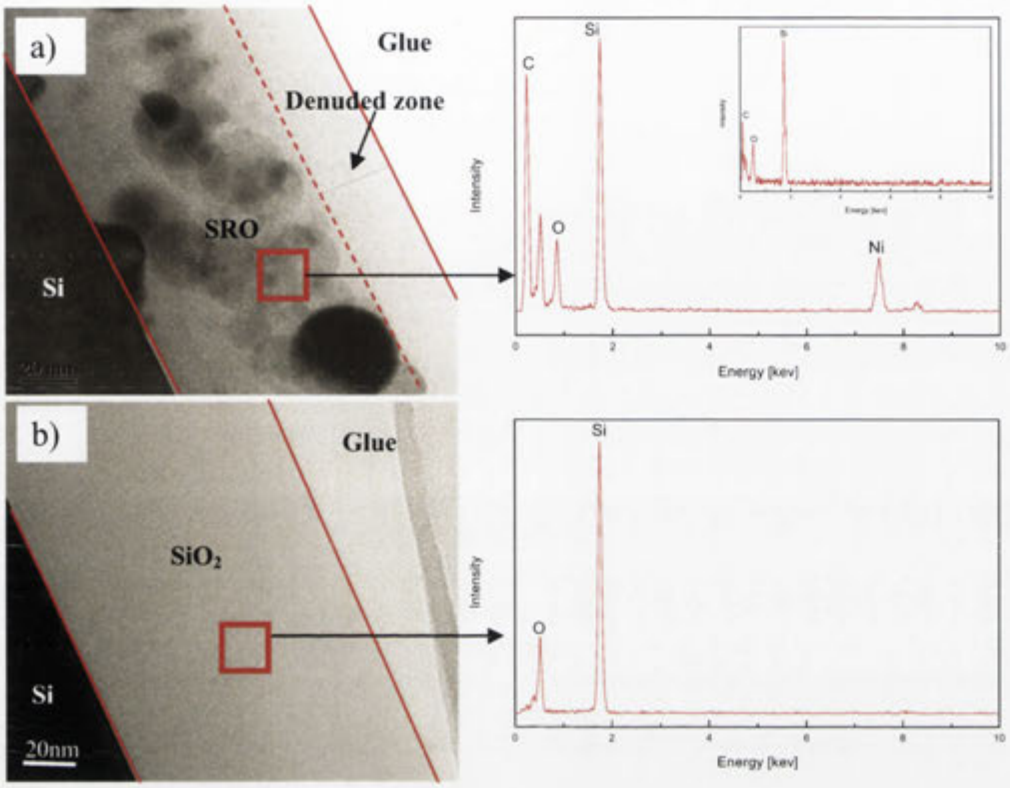

Figure 3.17: Cross-sectional TEM images of a) $SiO_{1.16}N_{0.32}$:H film and b) thermal SiO_2 film with Ni after annealing at 1100°C for 1 hour in N_2 ambient and EDX spectrum of each sample (inset denude zone).

Figure 3.17 shows cross-sectional TEM images of a $SiO_{1.16}N_{0.32}$:H film and a thermal SiO_2 film coated with Ni and annealed at 1100°C for 1h in a N_2 ambient. Nanocrystals are clearly observed in the SRO film but not in the SiO_2 film, as anticipated above. For the $SiO_{1.16}N_{0.32}$:H film, the Metal-NCs are distributed within the middle region of the film, with none observed in the region between the surface and a depth of about 30nm. This denuded region likely results from the competition between diffusion-limited reactions between Si and Ni and the concomitant formation of a SiO_2 surface layer from which Ni is excluded[55]. An EDX spectrum confirms the presence of Ni based NCs in the middle region and the lack of Ni near the surface. The denuded surface layer can be exploited as a control oxide (tunneling barrier) in a MIS memory device. According to previous research[56], depending on annealing temperature, Ni forms various stable silicide phases such as Ni_2Si (below 350°C), NiSi (at 350~750°C), and $NiSi_2$ (over 750°C). In our study, M-NCs were synthesized by annealing at a temperature of 1100°C, where the stable phase is expected to be nickel disilicide ($NiSi_2$).

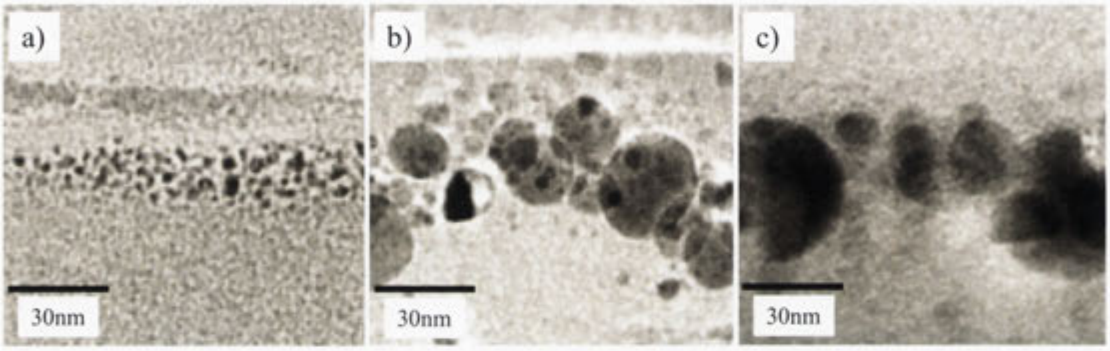

Figure 3.18: Cross-sectional TEM images of $SiO_{1.16}N_{0.32}$:H film with Ni after annealing at a) 800°C, b) 900°C, and c) 1100°C for 1 hour in N_2 ambient.

Figure 3.18 shows M-NCs fabricated in the $SiO_{1.16}N_{0.32}$:H film as a function of annealing temperatures at a) 800, b) 900, and c) 1100°C, respectively. The mean diameter of the M-NCs clearly depends on the annealing temperature, with the average diameter being ~3.3nm at 800°C, ~13.7nm at 900°C, and ~20.5nm at 1100°C.

Thermal processing of metal coated SRO films clearly provides a simple alternative route to the fabrication of nanocrystal-based thin-film structures. The size of the nanocrystals can be controlled by the annealing temperature, and a surface denuded zone can be formed under appropriate annealing conditions.

3.4.3 Nanowire growth with metal as catalyst

During the above study it was found that SRO films with high Si content produced additional surface features. For example, Figure 3.19 shows the surface of $SiO_{1.16}N_{0.32}$:H and $SiO_{0.65}N_{0.44}$:H films coated with 10 nm of Ni after annealing at

1100°C in N_2 ambient. The surface of the $SiO_{1.16}N_{0.32}$:H film is coated with Ni-based particles but the $SiO_{0.65}N_{0.44}$:H film is covered with a relatively low density of one-dimensional nanowires. According to previous studies[57-59], metals, including Ni and Au, can be used to grow one-dimensional nanostructures such as nanowires or nanotubes, and Ni has been used as a catalyst to grow silicon oxide nanowires on silicon substrates[60, 61]. The high Si content of the $SiO_{0.65}N_{0.44}$:H films is believed to facilitate a similar process in this case. Also, it is known that oxide decomposition is enhanced by Ni at high temperature[62]. These observations stimulated a more detailed study of nanowire growth and this work forms the basis of chapters 4 and 5 of this thesis.

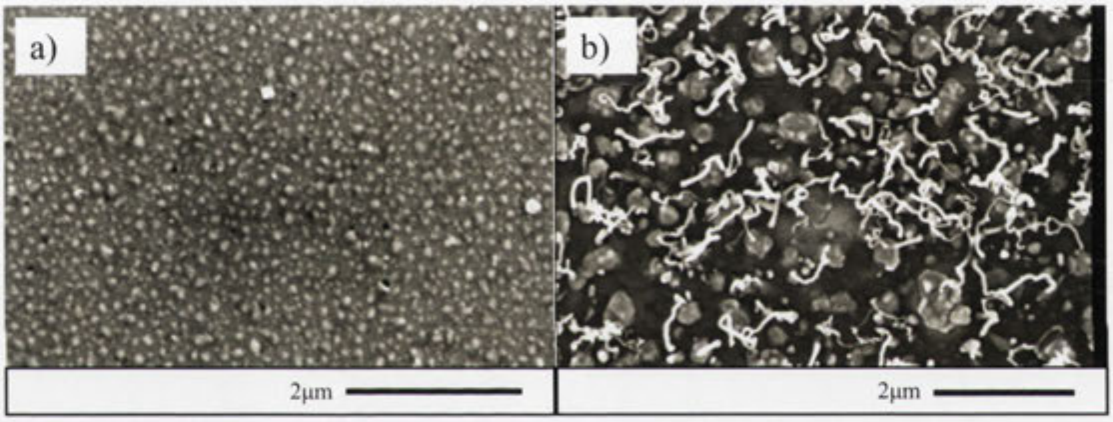

Figure 3.19: SEM images of the surface of Ni evaporated on a) $SiO_{1.16}N_{0.32}$:H and b) $SiO_{0.65}N_{0.44}$:H film after the annealing process.

3.5 Summary

This chapter has reported on mechanical properties of PECVD deposited silicon-rich-oxide films and surveyed potential applications of such films. Specifically, these films were shown to develop high tensile stress during annealing at temperatures up to 650°C, an effect that was shown to be correlated with an increase in hardness and a loss of hydrogen. For sufficiently thick films and high annealing temperatures, the stress is sufficient to cause film failure by cracking, and two distinct modes of crack propagation were reported for films on a (100) Si substrate: Straight cracks propagating along [100] directions in the underlying silicon substrate or oscillating cracks propagating along [110] directions in the underlying substrate. The wavelength and amplitude of oscillating cracks was modified by the addition of a SiO_2 buffer layer, and ion irradiation was shown to reduce the density of cracks.

Three specific applications of SRO films were surveyed. The first examined charge trapping in thin SRO films and showed that the concentration of programmable charge traps was correlated with hydrogen release. The second showed that metal-based nanocrystals could be formed within SRO layers by direct thermal reaction with a deposited metal layer and that under certain annealing conditions this reaction could produce a thin surface layer devoid of nanocrystals. The final study showed that thin metal films deposited onto SRO films with high Si content could produce one-dimensional nanostructures when annealed at elevated temperatures. This final observation provided the basis for the work outlined in the following chapters.

3.6 References

[1] H. Wong, *Microelectronics Reliability* **2002**, *42*, 317.
[2] B. Jalali, S. Yegnanarayanan, T. Yoon, T. Yoshimoto, I. Rendina, F. Coppinger, *Ieee Journal of Selected Topics in Quantum Electronics* **1998**, *4*, 938.
[3] R. M. de Ridder, K. Worhoff, A. Driessen, P. V. Lambeck, H. Albers, *Ieee Journal of Selected Topics in Quantum Electronics* **1998**, *4*, 930.
[4] C. David, D. Wiesmann, R. Germann, F. Horst, B. J. Offrein, R. Beyeler, H. W. M. Salemink, G. L. Bona, *Microelectronic Engineering* **2001**, *57-8*, 713.
[5] A. Monelli, F. Corni, R. Tonini, C. Ferrari, G. Ottaviani, L. Zanotti, G. Queirolo, *Journal of Applied Physics* **1996**, *80*, 109.
[6] H. J. Schliwinski, U. Schnakenberg, W. Windbracke, H. Neff, P. Lange, *Journal of the Electrochemical Society* **1992**, *139*, 1730.
[7] F. Ay, A. Aydinli, *Optical Materials* **2004**, *26*, 33.
[8] M. P. Hughey, R. F. Cook, *Materials research society symposium proceeding* **2003**, *766*, 345.
[9] Z. C. Xia, J. W. Hutchinson, *Journal of the Mechanics and Physics of Solids* **2000**, *48*, 1107.
[10] T. Ye, Z. Suo, A. G. Evans, *International Journal of Solids and Structures* **1992**, *29*, 2639.

[11] T. Yang, C. Shen, M. F. Li, C. H. Ang, C. X. Zhu, Y. C. Yeo, G. Samudra, S. C. Rustagi, M. B. Yu, D. L. Kwong, *Ieee Electron Device Letters* **2005**, *26*, 826.

[12] D. J. Dimaria, R. Ghez, D. W. Dong, *Journal of Applied Physics* **1980**, *51*, 4830.

[13] C. Falcony, J. S. Helman, *Journal of Applied Physics* **1983**, *54*, 442.

[14] D. J. Dimaria, D. W. Dong, C. Falcony, T. N. Theis, J. R. Kirtley, J. C. Tsang, D. R. Young, F. L. Pesavento, S. D. Brorson, *Journal of Applied Physics* **1983**, *54*, 5801.

[15] F. A. Sewell, H. A. R. Wegener, E. T. Lewis, *Applied Physics Letters* **1969**, *14*, 45.

[16] P. C. Y. Chen, *Ieee Transactions on Electron Devices* **1977**, *24*, 584.

[17] K. H. Wu, H. C. Chien, C. C. Chan, T. S. Chen, C. H. Kao, *Ieee Transactions on Electron Devices* **2005**, *52*, 987.

[18] F. Irrera, F. Russo, *Ieee Transactions on Electron Devices* **1999**, *46*, 2315.

[19] C. F. Lin, W. T. Tseng, M. S. Feng, *Japanese Journal of Applied Physics Part 1-Regular Papers Short Notes & Review Papers* **1998**, *37*, 6364.

[20] Z. R. Yu, M. Aceves, J. Carrillo, F. Flores, *Nanotechnology* **2003**, *14*, 959.

[21] M. Aceves, C. Falcony, A. ReynosoHernandez, W. Calleja, A. Torres, *Solid-State Electronics* **1996**, *39*, 637.

[22] W. Calleja, C. Falcony, A. Torres, M. Aceves, R. Osorio, *Thin Solid Films* **1995**, *270*, 114.

[23] S. Dusane, T. Bhave, S. Hullavard, S. V. Bhoraskar, S. Lokhare, *Solid State Communications* **1999**, *111*, 431.

[24] F. Iacona, S. Lombardo, S. U. Campisano, *Journal of Vacuum Science & Technology B* **1996**, *14*, 2693.

[25] K. Yano, T. Ishii, T. Hashimoto, T. Kobayashi, F. Murai, K. Seki, *Ieee Transactions on Electron Devices* **1994**, *41*, 1628.

[26] L. J. Guo, E. Leobandung, S. Y. Chou, *Applied Physics Letters* **1997**, *70*, 850.

[27] H. I. Hanafi, S. Tiwari, I. Khan, *Ieee Transactions on Electron Devices* **1996**, *43*, 1553.

[28] Z. T. Liu, C. Lee, V. Narayanan, G. Pei, E. C. Kan, *Ieee Transactions on Electron Devices* **2002**, *49*, 1606.

[29] G. G. Stoney, *Proc. R. Soc.* **1909**, *A 82*.

[30] M. P. Hughey, R. F. Cook, *Thin Solid Films* **2004**, *460*, 7.

[31] J. Thurn, R. F. Cook, *Journal of Applied Physics* **2002**, *91*, 1988.

[32] U. Kroll, J. Meier, A. Shah, S. Mikhailov, J. Weber, *Journal of Applied Physics* **1996**, *80*, 4971.

[33] K. S. Stevens, N. M. Johnson, *Journal of Applied Physics* **1992**, *71*, 2628.

[34] N. Iwashita, M. V. Swain, *Philosophical Magazine a-Physics of Condensed Matter Structure Defects and Mechanical Properties* **2002**, *82*, 2199.

[35] J. Moller, D. Reiche, M. Bobeth, W. Pompe, *Surface & Coatings Technology* **2002**, *150*, 8.

[36] T. Tsuchiya, A. Inoue, J. Sakata, *Sensors and Actuators a-Physical* **2000**, *82*, 286.

[37] L. A. Chow, Y. H. Xu, B. Dunn, K. N. Tu, C. Chiang, *Applied Physics Letters* **1998**, *73*, 2944.

[38] J. Turley, G. Sines, *Journal of Physics D-Applied Physics* **1971**, *4*, 264.

[39] R. G. Elliman, M. Spooner, T. D. M. Dall, T. H. Kim, N. H. Fletcher, *Philosophical Magazine* **2007**, *87*, 4893.

[40] P. Danesh, B. Pantchev, I. Savatinova, E. Liarokapis, B. Schmidt, *Vacuum* **2002**, *69*, 83.

[41] M. J. Powell, S. C. Deane, R. B. Wehrspohn, *Physical Review B* **2002**, *66*.

[42] Y. Deguchi, M. Ohnishi, Y. Takahashi, K. Ohnishi, *Electronics and Communications in Japan Part Ii-Electronics* **1997**, *80*, 30.

[43] Z. A. Weinberg, R. A. Pollak, *Applied Physics Letters* **1975**, *27*, 254.

[44] Z. A. Weinberg, *Applied Physics Letters* **1976**, *29*, 617.

[45] M. Aminzadeh, S. Nozaki, R. V. Giridhar, *Ieee Transactions on Electron Devices* **1988**, *35*, 459.

[46] R. E. Paulsen, R. R. Siergiej, M. L. French, M. H. White, *Ieee Electron Device Letters* **1992**, *13*, 627.

[47] D. M. Fleetwood, *Ieee Transactions on Nuclear Science* **1992**, *39*, 269.

[48] N. Daldosso, G. Das, S. Larcheri, G. Mariotto, G. Dalba, L. Pavesi, A. Irrera, F. Priolo, F. Iacona, F. Rocca, *Journal of Applied Physics* **2007**, *101*.

[49] F. Iacona, C. Bongiorno, C. Spinella, S. Boninelli, F. Priolo, *Journal of Applied Physics* **2004**, *95*, 3723.

[50] Y. Shi, K. Saito, H. Ishikuro, T. Hiramoto, *Journal of Applied Physics* **1998**, *84*, 2358.

[51] Y. H. Kwon, C. J. Park, W. C. Lee, D. J. Fu, Y. Shon, T. W. Kang, C. Y. Hong, H. Y. Cho, K. L. Wang, *Applied Physics Letters* **2002**, *80*, 2502.

[52] A. R. Wilkinson, R. G. Elliman, *Applied Physics Letters* **2003**, *83*, 5512.

[53] A. R. Wilkinson, R. G. Elliman, *Physical Review B* **2003**, *68*.
[54] P. H. Yeh, L. J. Chen, P. T. Liu, D. Y. Wang, T. C. Chang, *Electrochimica Acta* **2007**, *52*, 2920.
[55] J. H. Yoon, R. G. Elliman, *Colloids and Surfaces a-Physicochemical and Engineering Aspects* **2008**, *313*, 365.
[56] K. N. Tu, *Applied Physics Letters* **1975**, *27*, 221.
[57] Z. J. Zhang, G. Ramanath, P. M. Ajayan, D. Goldberg, Y. Bando, *Advanced Materials* **2001**, *13*, 197.
[58] M. Paulose, O. K. Varghese, C. A. Grimes, *Journal of Nanoscience and Nanotechnology* **2003**, *3*, 341.
[59] S. H. Li, X. F. Zhu, Y. P. Zhao, *Journal of Physical Chemistry B* **2004**, *108*, 17032.
[60] B. Park, K. Yong, *Surface Review and Letters* **2004**, *11*, 179.
[61] J. H. Hsu, M. H. Huang, H. H. Lin, H. N. Lin, *Nanotechnology* **2006**, *17*, 170.
[62] H. Dallaporta, M. Liehr, J. E. Lewis, *Physical Review B* **1990**, *41*, 5075.

Chapter 4

Growth and control of silica nanowires

Amorphous sub-stoichometric silica (SiO_x) nanowires can be grown on silicon substrates by coating the substrate with a thin metal film and annealing it in Ar or N_2 at temperatures above 1000^oC. Such nanowires can also be grown on silica substrates in situations where a silicon wafer is placed in close proximity to the silica substrate. These are unexpected results as there is no obvious vapour-phase source of oxygen or silicon to facilitate such growth (the vapour pressure of silicon at 1100^oC is too low to account for the observed growth). This chapter examines the mechanisms responsible for nanowire growth and explores the affect of processing conditions on the properties and resulting structure of the nanowires.

4.1 Introduction

Silica nanostructures are of great interest for applications that exploit both the intrinsic properties of silica (i.e. optically transparent, chemically inert and biocompatible) and the large surface-to-volume fraction of nanostructured materials such as environmental and biological sensing. Such applications are further enhanced by the fact that silica is a suitable host for optically active impurities, such as trivalent Er. In optically-doped nanostructures the dopant ions are always close to a surface due to the small physical dimensions of the structure. The optical transition rate is therefore expected to be particularly sensitive to the state of the surface and its neighbouring environment. It is not surprising therefore that there has been intense interest in recent years in the growth of silica nanostructures, including the growth of one-dimensional silica nanowires[1, 2] and nanotubes[3, 4].

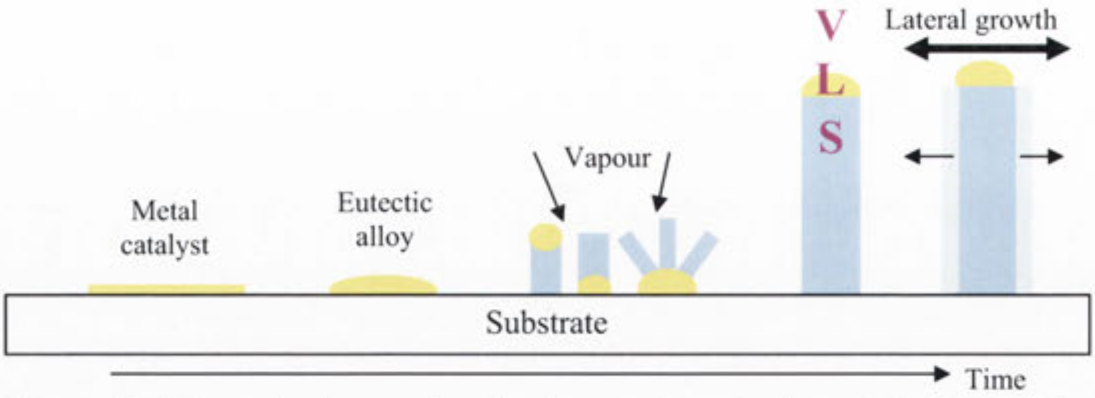

Figure 4.1: Schematic diagram showing the growth mechanism of the Vapour-Liquid-Solid process.

Nanowires can be grown with the aid of metal catalyst particles in which case the mechanism is designated by the state [solid(S), liquid(L), gas(G)] of the source, catalyst and nanowire, respectively[5-8]. Thus a vapour-liquid-solid (VLS) process, such as that illustrated in Fig. 4.1, involves a gaseous source of reactants, a liquid metal-alloy catalyst and a solid nanowire. In this case the catalyst absorbs gas-phase reactants becoming supersaturated with respect to the precipitation of a secondary phase. Once nucleated, these precipitates grow into wires as the catalyst continues to absorb and transport reactants from the gas phase. During VLS growth, gas-phase reactants can also deposit on the side walls of the nanowires resulting in lateral growth, as illustrated in Fig. 4.1.

During nanowire growth the catalyst particle can either 'ride' on top of the growing wire (float growth) or remain in contact with the substrate, in which case the wire extends from it (root growth), as shown in Fig. 4.2. The size-distribution and density of the resulting nanowires are determined largely by those of the catalyst particles. However, this relationship is not a simple one because the metal catalyst reacts with the substrate and source gases to form eutectic or mixed phases prior to nanowire nucleation and depending on its size can nucleate one-or more nanowires (i.e. single or multiprong growth,see Fig. 4.2). The mode of growth (i.e. root or float) also depends on the choice of catalyst metal and has important implications for the final structure and form of the nanowires.

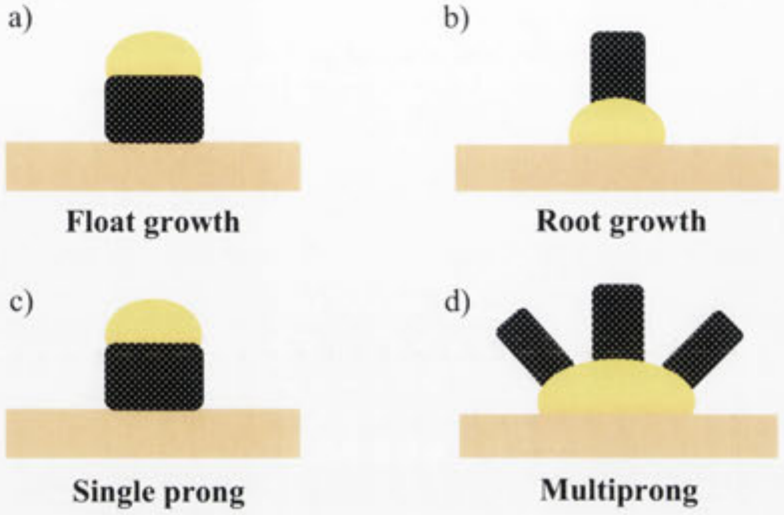

Figure 4.2: Different growth process modes (after Kolasinski[9]).

Yu et al[1]. first reported the large scale synthesis of silica nanowires using laser ablation of silica and silicon in the presence of a metallic Fe catalyst to promote growth via a VLS mechanism. Since then many alternative fabrication methods have been reported[10-13]. In the catalyst-based methods, several different metal catalysts have been utilized, including Au[14, 15], Ni[16], Fe[17] and Pd[18]. At the same time, there have been efforts to understand the nanowire growth mechanism, with different catalyst and non-catalyst models proposed and indentified, such as vapour-liquid-solid (VLS)[11], vapour-solid-solid (VSS)[19], oxide-assisted growth (OAG)[20] and solid-liquid-solid (SLS)[21]. The VLS mechanism, first proposed by Wagner et al.[22] for the growth of silicon nanowires in the early 1960s, is widely employed to grow nanowires and has recently been unambiguously demonstrated for silica nanowires by direct observation with in-situ TEM by Wu et al.[23].

Control over nanowire growth is an important requirement for future nanotechnology devices because the physical structure and chemical properties of nanowires are critically affected by diameter, length, atomic composition and nanowire density[24-26]. Consequently, various methods based on the VLS mechanism have been introduced and developed to synthesize nanowires. The diameter of nanowires is dependent on many factors, including the catalyst/substrate combination, process gases, growth temperature, or combinations of these parameters. Critically, the nanowire diameter is also directly related to the size of the metal seed particles[27]. For example, Wu et al. report that nanowires with very small diameter sizes can be grown by using well-defined Au nanoparticles as the catalyst[24]. Silica substrates with small diameter pores have also been used for the nucleation and growth of nanowires[28, 29].

Silica nanowires and silica/silicon core-shell nanowires can also be formed by the oxidation of silicon nanowires[30, 31]. Unlike silica nanowires grown directly on silicon, those derived from silicon nanowires reflect the crystallographic orientation of the latter. It has been observed that the preferred orientation of silicon nanowires is correlated with their diameter, with larger nanowires exhibiting a stronger preference for particular directions[24, 32]. The crystal orientation of the substrate is also critical for determining the growth direction of these nanowires. Ge et al.[33] demonstrated orientation-controlled growth of silicon nanowires on silicon (100), (110), and (111) substrates. The lateral distribution of nanowires can also be controlled by the designated positioning of metal catalyst particles and lithography and molecular beam epitaxy techniques have been used to grow nanowires at specific sites[34]. The growth of vertically and laterally aligned nanowire arrays were reported by Yang et al[35]. Hyper-branched structure of nanowires have also been synthesized by using Au particles on a prefabricated nanowire backbone[36].

4.2 Experimental details

The substrates investigated in this study include p-type silicon wafers of (100), (110) and (111) orientation and fused silica slides (for comparison); coated with a 100nm thick thermal SiO_2 layer or a 100nm thick silicon-rich-oxide ($SiO_{1.16}N_{0.32}$:H) film deposited by PECVD.

Metal catalyst particles were formed by three different approaches: 1) the islanding of thin Gold (Au) or Nickel (Ni) films deposited onto substrates by thermal evaporation or sputter deposition; 2) Au ion-implantation into (100) Si substrates employing 30keV Au^- ions (projected range ~20nm) implanted at fluences of $6x10^{14}$, $1x10^{15}$, $3x10^{15}$, $1x10^{16}$, $3x10^{16}$ ions/cm^2; and 3) Au colloids with diameters of 5, 10, 30, 50nm deposited using a poly-L-Lysine solution. This solution possesses a polar structure with positive surface charges to immobilize the Au colloidal particles and prevent coalescence. It evaporates during the annealing process and thus does not affect the resulting nanowire growth.

Samples were annealed in a fused-silica tube furnace at temperatures between 800 and 1100°C for various times between 5 minutes and 2 hours. During annealing the furnace was purged with flowing N_2, Ar, O_2 or forming (5% hydrogen in 95% Nitrogen) gas with a flow rate of 100 sccm; or in air (open ended tube). When being placed in the tube, the samples were in a quartz boat pushed slowly into a pre-heated furnace using a quartz rod. Also, the samples were pulled slowly out from the tube while the furnace preserved the heating temperature.

The structure and morphology of the samples, catalyst-particles and resulting nanowires were studied by scanning electron microscopy (SEM) [Hitachi field-emission scanning microscope S-4300 (FE-SEM) equipped with energy dispersive X-ray (EDX) detector and backscattering detector] and high-resolution transmission election microscopy (HRTEM) [Philips CM300 FEI microscope with Schottky field emission gun operating at 300kV] fitted with energy dispersive spectroscopy (EDS) [Oxford Instrument EDX] detector.

4.3 Experimental result

4.3.1 Nanowire growth – general observations

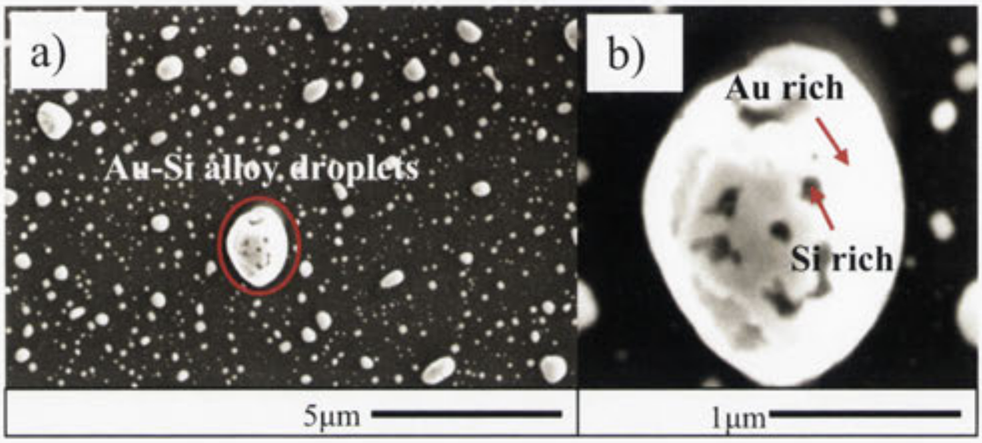

Figure 4.3: SEM images of a) Au-Si islands on Si after annealing at 900°C and b) the observation of phase separation in bigger Au-Si alloy droplets (backscattering image).

The annealing behavior of a 10nm Au film on (100) silicon serves as a useful model system for studying silica nanowire growth. During annealing to temperatures up to 1000°C in a N_2 ambient the deposited film breaks up into small islands and reacts with the silicon substrate to form Au-Si eutectic alloys.

Figure 4.3 a) shows SEM images of Au-Si islands on the surface of a Si substrate after annealing a (100) Si wafer with a 10nm surface layer of Au below 1000°C. Au forms a low melting-point (363°C) eutectic-alloy with silicon and during annealing at higher temperatures, reacts with the silicon to form molten alloy droplets. These droplets have a broad size distribution, with individual particles ranging in size from around 10nm to 1μm. Upon cooling to room temperature the alloy particles undergo phase separation into silicon-rich and gold-rich phases, as shown in Fig. 4.3b). These electron backscattering images are particularly well suited to distinguishing between high and low atomic number elements, with the high atomic number element appearing bright and the low atomic number element appearing dark. Interestingly, the smaller Au droplets are observed as single bright object, and an effect that is attributed to the fact that all of the Si from the liquid eutectic has precipitated onto the substrate surface during solidification[37].

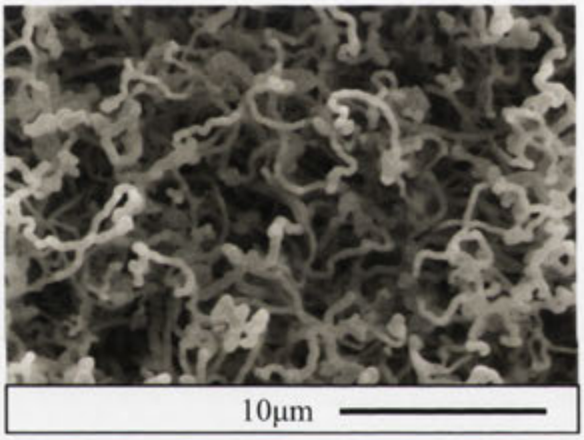

Figure 4.4: SEM image of silica nanowires grown on Si after annealing at 1100°C in N_2 gas for 1 hour.

Samples annealed at temperatures above 1000°C have a completely different appearance and structure. The samples appear white under ambient lighting conditions and SEM analysis confirms that they are coated with a dense array of amorphous silica nanowires, as shown in Fig. 4.4. The diameters of the nanowires range from 50nm to 2μm and their lengths are in excess of a few hundred μm. This behavior is observed for samples after annealing in both N_2 and Ar.

In order to investigate the chemical composition and growth mode of these nanowires, cross-sectional backscattered electron images and EDX analysis were performed. The samples were cleaved to reveal cross-sectional views of the nanowire layer and analysed with 10 kV electrons. Figure 4.5 a) shows an overall view of the layer illustrating the random growth direction of the wires and the presence of Au located proximal to the root of the wires near the substrate. Imaging and EDX analysis of the head(b), stem(c) and root(d) regions of the layer show that nanowires have a composition of SiO_x with x close to 1.8, and that Au remains at the stem of the nanowires (i.e. at the substrate interface). No EDX signal of Au was observed on the head or on the sidewalls of nanowires. This clearly shows that Root Growth is the dominant growth mechanism in this case. Interestingly, the interface between the Si substrate and nanowires is observed to be very rough. An explanation for this etching-like behavior is provided in section 4.4.3.

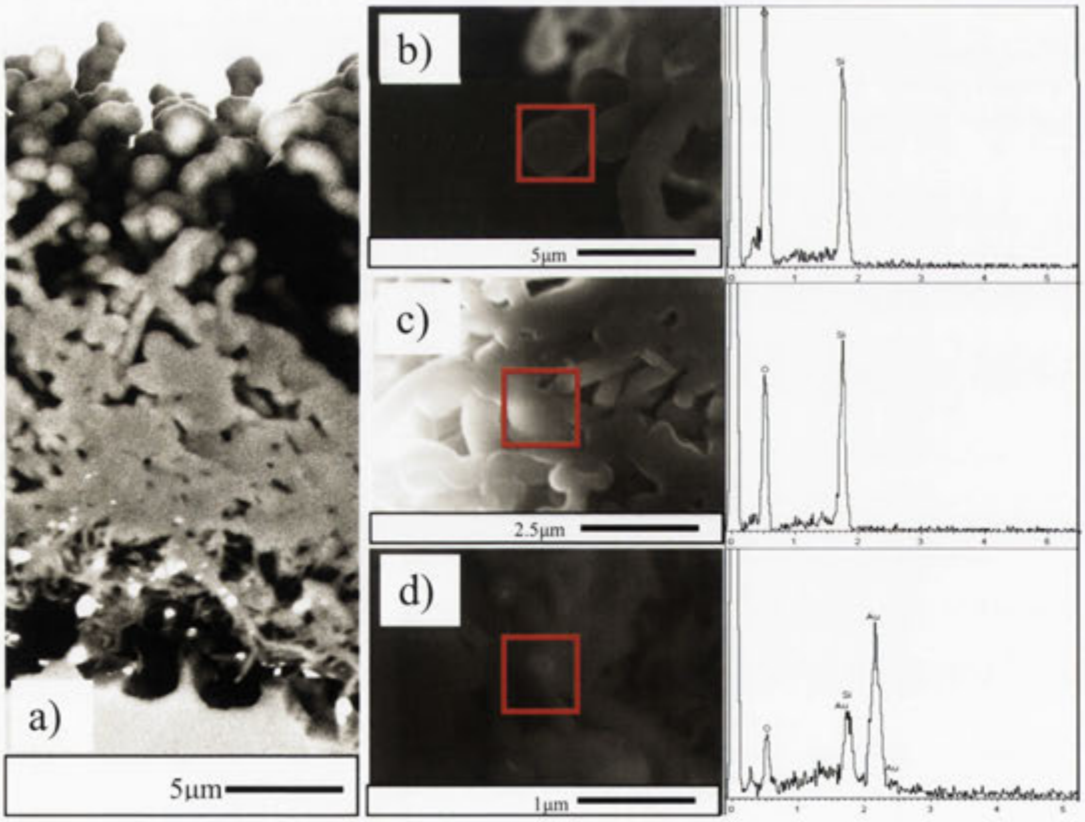

Figure 4.5: a) cross sectional backscattering image, b) head, c) stem, and d) root of silica nanowires and EDX analysis, respectively.

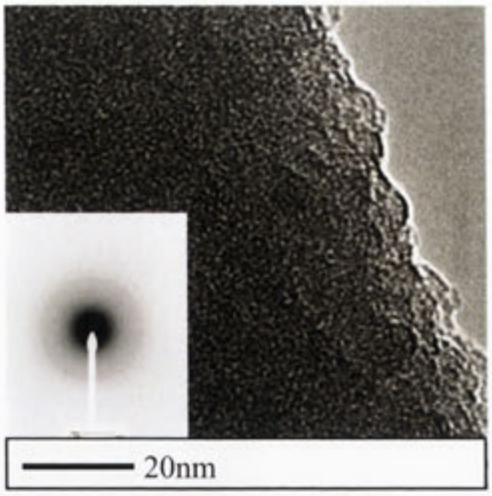

Figure 4.6: HRTEM image and amorphous nature of the electron diffraction (inset) of nanowires grown on Si after annealing at 1100°C in N_2 for 1hour.

Microstructural analysis of the nanowires using high-resolution transmission electron microscopy (HRTEM), as shown in Fig. 4.6, shows that the nanowires are amorphous silica. i.e. No fringe-patterns indicative of crystalline Si were observed inside the nanowires and electron diffraction (inset) showed a typical amorphous ring pattern. Interestingly, HRTEM also reveals that the surface morphology of the wires is relatively rough on the 5-10nm scale as seen in Fig. 4.6.

In summary, annealing metal (The work presented here was for Au-coated Si but similar results were observed for Ni, Pt and Pd coated Si) coated silicon at temperatures above about 1000°C in N_2 or Ar can produce dense arrays of amorphous silicon-rich silica ($SiO_{1.8}$) nanowires via a root-growth mechanism. It remains to identify the mechanism for growth and the source of the silicon and oxygen reactants.

4.3.2. Growth mechanisms of silica nanowires

The growth of silica nanowires during furnace annealing without any additional process gas (e.g. SiH_4) has variously been attributed to VLS[2, 38], SLS[15] or catalyst-free growth

OAG[39] mechanisms. For VLS growth, the source of oxygen has been assumed to come from decomposition of the native oxide, or from contamination of the annealing ambient with O_2 or H_2O. Similarly, the source of silicon has variously been assumed to derive from direct dissolution of the Si substrate; evaporation from the substrate; decomposition of the native oxide in the form of SiO_2 or SiO vapour; and from a reaction between residual oxygen and silicon in the form of SiO or SiO_2 vapour. These possibilities are summarized below:

A: Oxygen

- Oxygen derives from the native oxide on the Si wafer in the form of O_2, SiO_2 or SiO.
- Oxygen derives from the annealing ambient as a low concentration contaminant.

B: Silicon

- Si derives from the substrate by direct dissolution
- Si derives from the substrate by direct evaporation
- Si derives from the native oxide of the Si wafer in the form of SiO_2 or SiO
- Si derives from the substrate via a reaction between residual oxygen or water vapour and Si in the form of SiO or SiO_2 vapour.

Note: The furnace tube was ruled out as a source of silicon and oxygen because it is manufactured by melting naturally occurring quartz crystals of high purity at approximately 2000°C, which does not easily decompose.

4.3.3 Source of oxygen

It is well known[40] that annealing a thin oxide layer on Si film will form gaseous SiO vapour at temperatures above 800°C, according to the reaction:

$$Si_{(s)} + SiO_{2(s)} \rightarrow 2SiO_{(g)}.$$

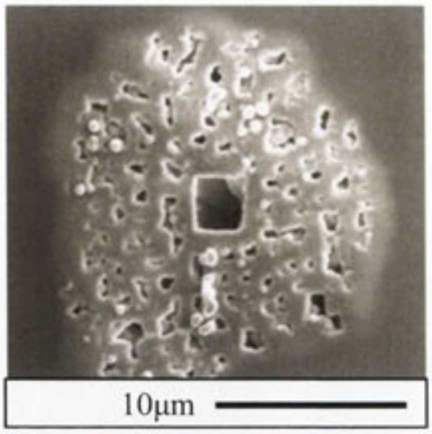

Figure 4.7: SEM image of the etching circles on Si wafer placed on top of Au coated wafer during annealing at 1100°C in N_2 for 1hour.

This reaction is often heterogeneous, beginning at defects and proceeding radically by decomposition at the exposed SiO_2/Si interface. This leads to circular etch patterns within the native oxide, as shown in Fig 4.7. This image is from a silicon wafer placed on top of a metal coated wafer during annealing at 1100°C in N_2 for 1hour. The presence of metal is expected to enhance such reactions.

However, due to its limited thickness of about 2~5nm, the native oxide on Si cannot provide volatile SiO in sufficient quantities to account for the observed volume of nanowires. This is confirmed by a simple calculation. i.e. A native oxide of thickness 5nm and bulk density ($6.6x10^{22}$ atomscm^{-3}) contains around 2.2×10^{16} (oxygen atom.cm^{-2}). By comparison, the number of oxygen atoms in a typical nanowire layer of thickness 200μm and 1% volume density is around 1.0×10^{19} (atom.cm^{-2}). For a 10% volume fraction, which is closer to that observed, this increases to around 1.0×10^{20} (atom.cm^{-2}). This suggests that the amount of oxygen contained within the nanowires is between 10^3 and 10^4 times the amount available from the native oxide so the native oxide is therefore not the primary source of oxygen.

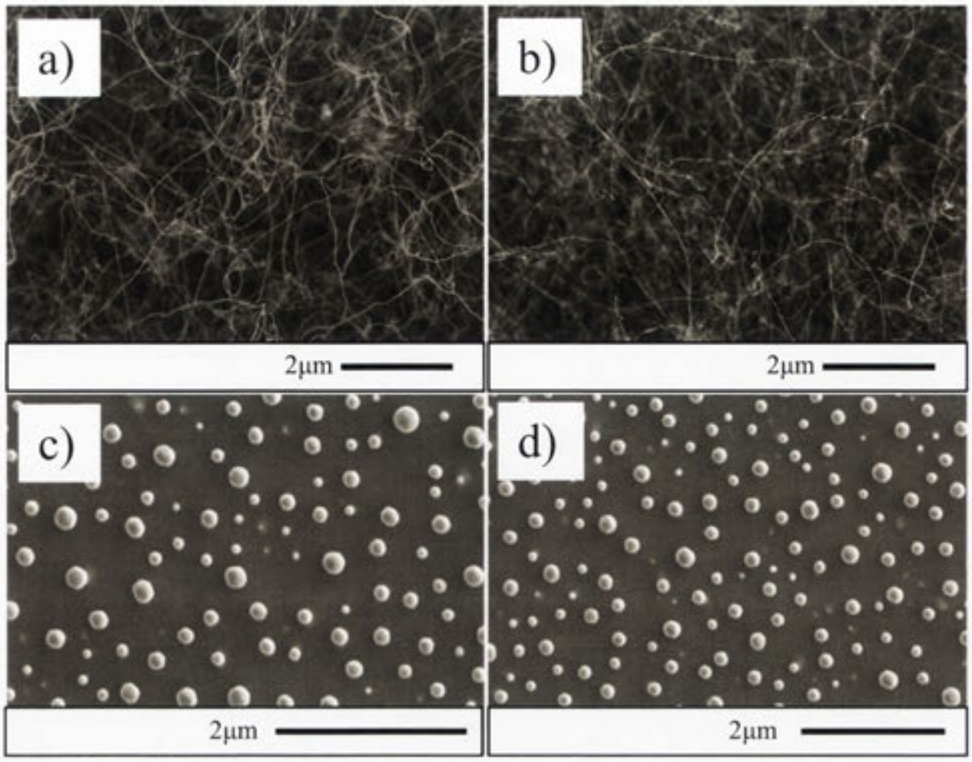

Figure 4.8: SEM images of the resulting morphologies on the Si substrate with metal catalysts after annealing at 1100°C for 1hour in a) nitrogen (or argon), b) forming gas (5% hydrogen in nitrogen), c) oxygen, and d) air ambient.

Nanowire growth based on direct reactions with oxygen might reasonably be expected to exhibit reaction rates that are proportional to the oxygen concentration. To test this scenario, samples were annealed in nitrogen, forming gas, oxygen and air. Figure 4.8 shows SEM images of the samples after annealing. These show that nanowires formed on samples annealed in nitrogen (a) and forming gas (b) but not on samples annealed in air (c) or pure oxygen (d). Clearly, too much oxygen inhibits the reaction responsible for nanowire growth.

With this evidence, a detailed review of the oxidation kinetics of silicon revealed the fact that the dominant oxidation reactions depend strongly on oxygen partial pressure. This is evident from early work by Gelain[41], who showed that the reactions between silicon and oxygen fall into two distinct regimes: At low oxygen partial pressures the dominant reaction is:

$$2Si + O_2 \rightarrow 2SiO$$

While at high oxygen partial pressures it is:

$$Si + O_2 \rightarrow SiO_2$$

The former results in etching of the silicon substrate and produces volatile SiO, while the latter produces a passivating layer of SiO_2 on silicon. The temperature/partial-pressure phase-space for these two reactions is shown in Fig. 4.9.

Reference to the manufacturer's specifications for the annealing gases employed in the present study show that they typically contain up to 3-10 ppm of O_2 and H_2O. This is shown as an effective partial pressure in Fig. 4.9 a) and, significantly, corresponds to a critical temperature of around 1000°C for the transition between the two reactions. i.e. For temperatures above 1000°C the reaction between silicon and the residual oxygen is expected to etch the silicon substrate and produce volatile SiO vapour, while at temperatures below 1000°C it is expected to produce a passivating SiO_2 layer. Annealing in pure oxygen or air is similarly expected to produce a passivating SiO_2 layer. Figure 4.9 a) show a graph (left) of oxygen pressure as a function of annealing temperature plotted by C. Gelain[41] and J.J. Lander[42] et. al and SEM images (right) of samples annealed at different temperature b) 800, c) 900, d) 1000, and e) 1100°C. Clearly, nanowire growth coincides with the regime in which SiO vapour is produced.

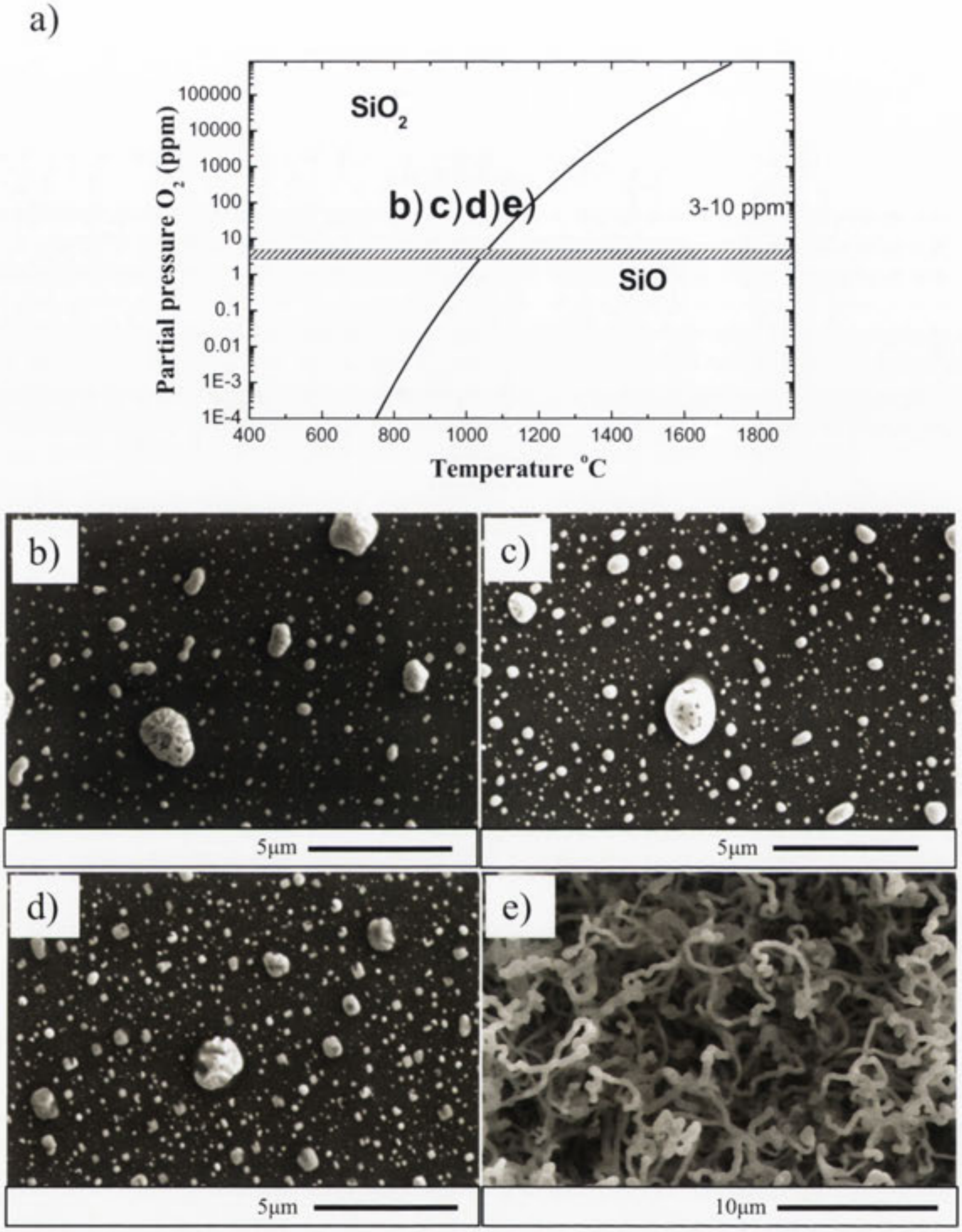

Figure 4.9: a) Oxygen pressure vs annealing temperature plotted by C. Gelain[41] and J.J. Lander[42] et. al and SEM images of samples annealed at b) 800, c) 900, d) 1000, and e) 1100°C.

These observations lead to the conclusion that residual oxygen or water vapour at the 3-10 ppm level is crucial for the observed nanowire growth. This conclusion is further supported by evidence presented in the following section.

4.3.4 Source of Si

A: Metal-coated silicon wafers

As discussed above the source of silicon can derive from: a) direct dissolution of the Si substrate; b) evaporation from the substrate; c) decomposition of the native oxide in the form of SiO_2 or SiO vapour; or d) from a reaction with residual oxygen to produce SiO vapour. Direct dissolution of the silicon substrate has already been demonstrated, as shown in Fig. 4.3, and is expected to be a significant source of silicon during root growth of nanowires. However, a catalyst particle in contact with the silicon substrate will continuously dissolve and deposit silicon from the substrate to maintain an equilibrium concentration. Such processes will not lead to nanowire growth as there is no driving force for the precipitation of new phases. This can only be achieved by an additional vapour-phase source of silicon where the driving force is provided by the free energy difference between the vapour and condensed phases of Si/SiO_2.

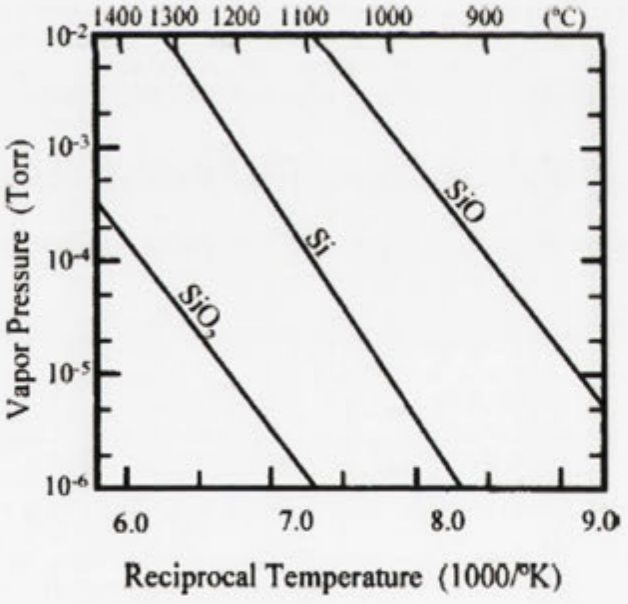

Figure 4.10: Equilibrium vapor pressures of silicon and its oxides (after Suzuki et al[40]).

A study by Suzuki et al[40] has shown that the vapour pressure of Si is two orders of magnitude lower than that of SiO over the temperature range employed for nanowire growth, as shown in Fig. 4.10. They have further shown that square etch pits are formed on the surface of silicon during reaction with oxygen at low partial pressures. This suggests that the reaction between silicon and residual oxygen can produce significant quantities of SiO.

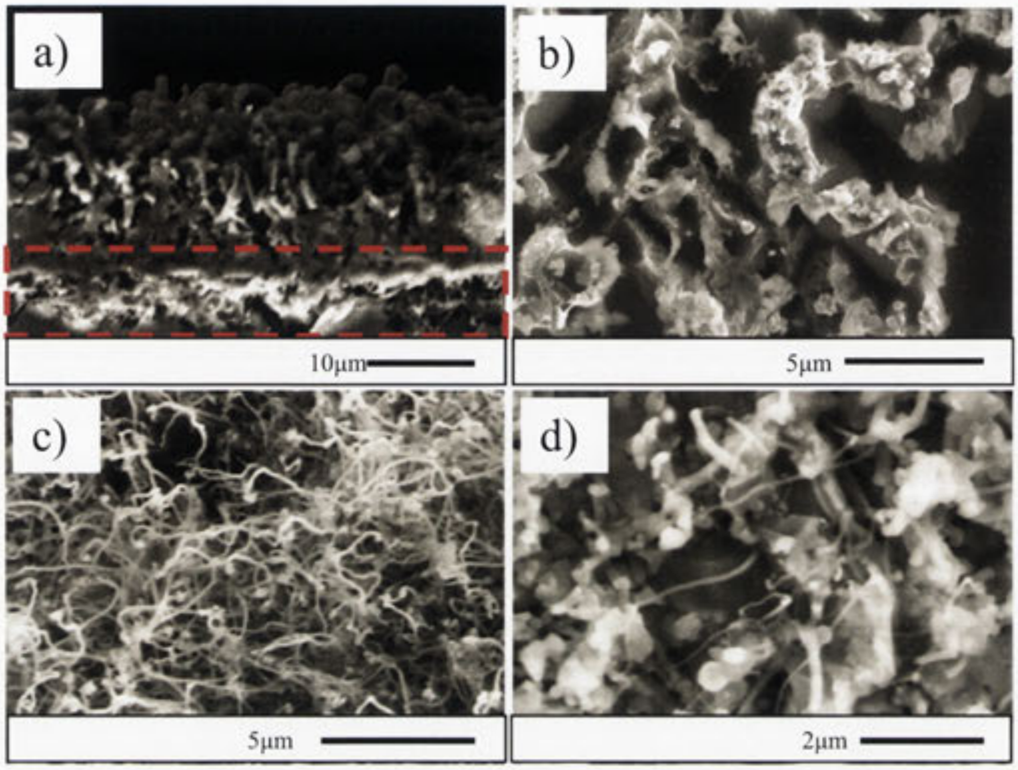

Figure 4.11: a) A cross-sectional SEM image of the nanowire-silicon interface before delamination (interface indicated by red box), b) SEM image of the Si substrate after the spontaneous delamination of the nanowire film, c) an SEM image of the top (free) surface of a self-supporting film, and d) an SEM image of the substrate-side of the delaminated nanowire film.

Such pitting is also observed in the current study and in extreme cases can lead to spontaneous delamination of a nanowire film, as discussed in more detail in secton 5.3.1. The substrate etching at the interface between the substrate and the growing nanowires is clearly evident in Figs. 4.11 a) and 4.11 b). Figure 4.11 c) and d) show to top and bottom surfaces of the nanowire film for comparison. These observations are consistentwith a model in which residual oxygen acts to etch the silicon substrate and form SiO vapour.

B: Metal-coated silica substrate

In order to confirm the role and origin of SiO in nanowire growth, a silica sample was coated with 10nm Au and annealed at 1100°C in a N_2 environment for 1 hour (the same annealing conditions used to grow nanowires previously on a Si substrate). No nanowires were observed, but Au islands were formed on the silica surface, as seen in Figure 4.12 a). The same sample was then annealed with a Si capping layer, (silica sample placed face (Au side) down on a (100) silicon wafer to provide a direct Si source during the annealing process). In this case silica nanowires were observed on the silica, as shown in Figure 4.12 b). These nanowires were distinctly different to those grown on silicon substrates in that they form by a float growth mechanism[9] (i.e. the catalyst particle resides at the tip of the nanowire). This is evident from the SEM image of Fig. 4.12 c) and inset EDX spectrum that clearly shows Au particles located on the tips of the nanowires[9]. In addition, the nanowires tended to be tapered, shorter and thinner than those grown on silicon, with lengths typically less than 1μm and diameters ranging from 50 nm to 200 nm.

Significantly, Fig. 4.12 d) shows that the surface of the Si capping layer was heavily etched during nanowire growth. This is consistent with the work reported by Suzuki et al[40] and supports a model in which nanowire growth is mediated by SiO vapour produced via the reaction between silicon and oxygen at low partial pressures. Etching of the silicon capping wafer also appears to be enhanced by the presence of the metallic catalyst as bare wafers annealed under similar conditions did not exhibit significant etching. The presence of Au on the capping wafer was confirmed by SEM imaging and is also evident from the presence of low concentrations of nanowires on the capping wafer surface, as shown in Fig. 4.12 d). This Au is assumed to evaporate from the silica substrate and deposit on the capping wafer during annealing at 1100°C. Au is likely to enhance SiO production because it is known to act as catalyst for the oxidation of Si surfaces[43].

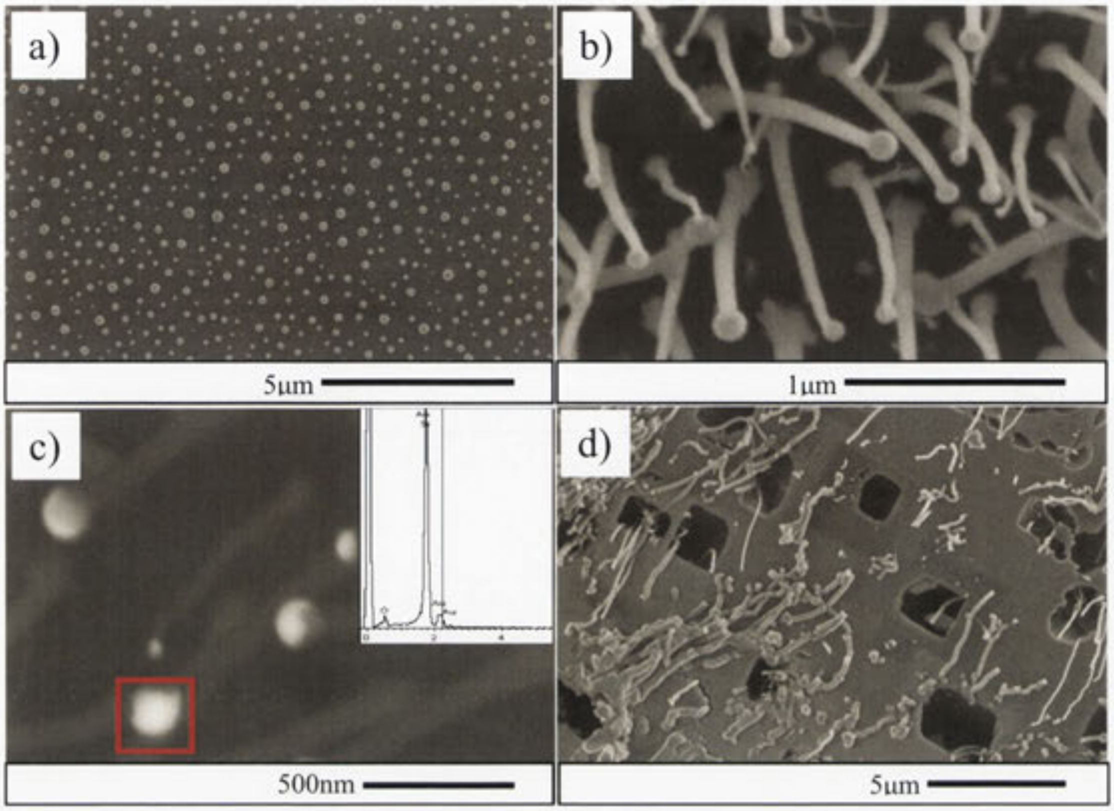

Figure 4.12: a) SEM image of Au particles on silica after annealing, b) SEM image of silica nanowires grown on silica substrate after annealing with Si capping layer, c) Backscattering image of silica nanowires grown on silica substrate after annealing with Si capping layer (inset EDX analysis) and d) SEM image of surface of Si capping layer after annealing.

The above data suggests that silicon dissolution from the substrate and vapour-phase SiO from a reaction between the silicon substrate and oxygen present at low partial pressures in the annealing ambient are the primary sources of silicon for nanowire growth.

4.3.5 Proposed growth mechanism of silica nanowires

The proposed nanowire growth mechanism is summarized schematically below with reference to Fig. 4.13. The discussion concentrates on the typical mode of growth observed in each case. Other variants are discussed in more detail in the latter part of this chapter.

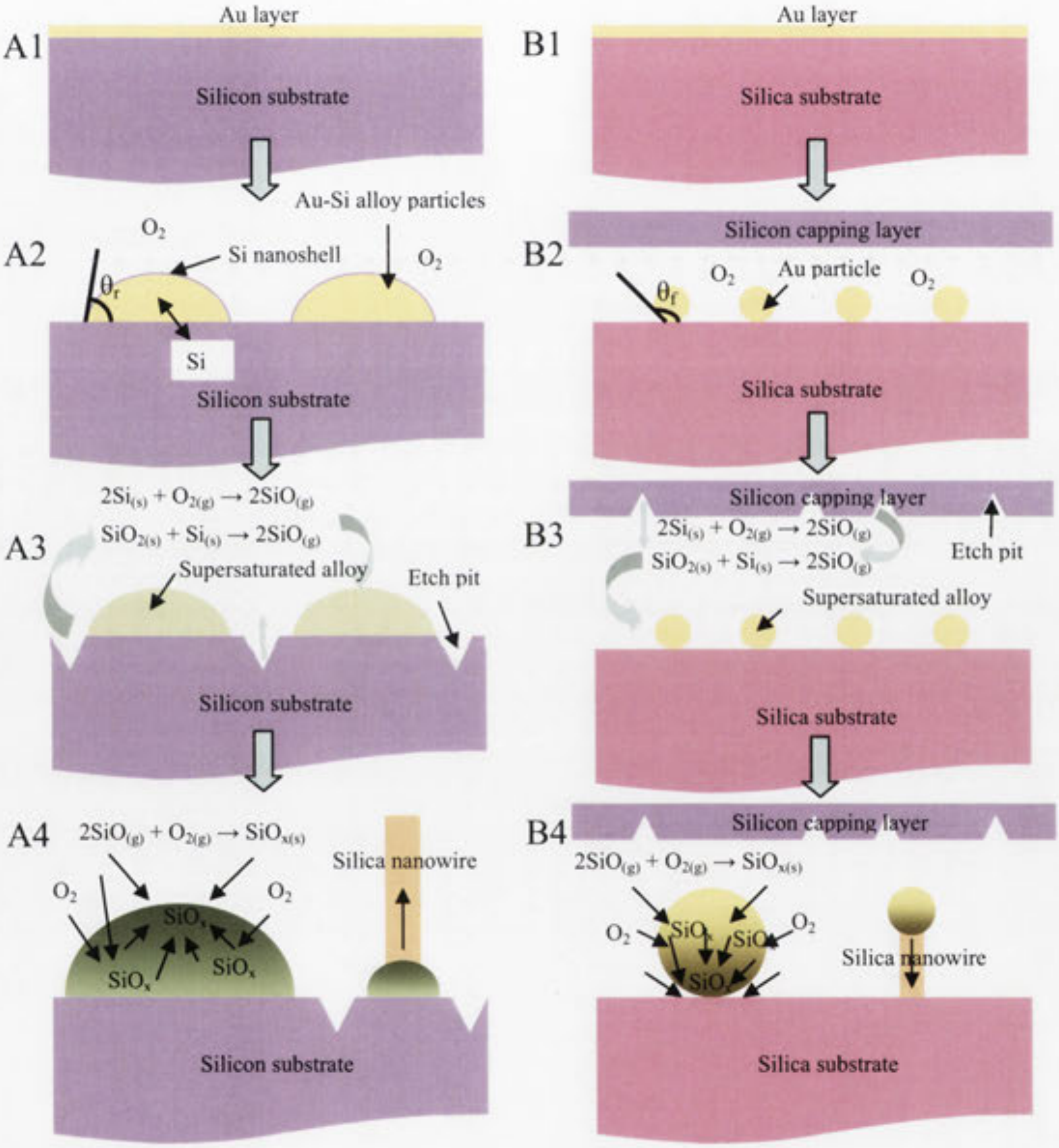

Figure 4.13: Schematic drawing of silica nanowires on Si (A1→A2→A3→A4) and Silica with capping layer (B1→B2→B3→B4).

A: Silicon substrate (no capping layer)

1) The deposition of gold on silicon produces a uniform, continuous thin film of gold across the silicon surface (Fig 4.13 A1).

2) During annealing the gold film breaks up into small islands and reacts with the silicon substrate to form Au-Si alloy droplets. Above the eutectic temperature (363°C) the droplets are molten and have a temperature-dependent composition as determined from the Au-Si phase diagram (Fig 4.14). At 1100°C this composition is approximately 42% Au: 58% Si. The volume of eutectic particles is larger than that of the initial gold particles due to the dissolution of silicon and may have a thin silicon-rich outer shell[44, 45]. The particles have a flattened hemispherical shape due to the small contact angle (θ_r) between the alloy and silicon (Fig 4.13 A2). In the absence of gas-phase reactants the liquid Au:Si eutectic particles continuously dissolve and redeposit silicon at the point of contact with the substrate to maintain their equilibrium composition.

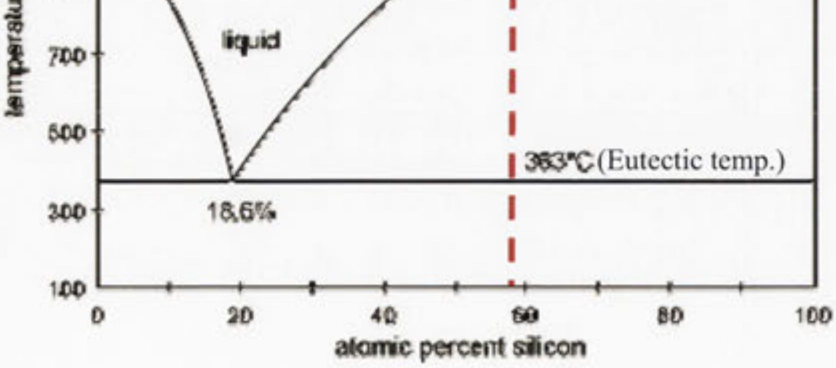

Figure 4.14: A Au:Si phase diagram.

3) The presence of Au on silicon enhances the reaction between silicon and the residual oxygen that is present in the annealing ambient at concentrations of ~3-10 ppm. At temperatures above ~1000°C this results in etching of the silicon substrate via the reaction $2Si+O_2 \rightarrow 2SiO$ and produces SiO vapour. [Although some SiO vapour is produced from decomposition of native oxide on Si ($SiO_{2(s)}+Si_{(s)} \rightarrow 2SiO_{(g)}$), much more SiO vapour is produced via the reaction of Si and O_2 ($2Si_{(s)}+O_{2(g)} \rightarrow 2SiO_{(g)}$) at high temperatures with low concentrations of oxygen.]. The vapour pressure of SiO is much higher than either Si or SiO_2 and is the dominant vapour source under the annealing conditions employed for nanowire growth (Fig 4.13 A3).

4) The liquid Au:Si eutectic particles now absorb SiO and O_2 vapour from the gas phase as well as exchanging Si with the substrate. This ultimately leads to the nucleation and growth of SiO_x nanowires and their extension from the droplet via a root-growth process (Fig 4.13 A4). The atomistic mechanisms for these processes remain unclear but some general conclusions can be drawn from the data. First, the fact that wires grow out of the catalyst particle suggests that growth occurs from the catalyst surface rather than from the catalyst-substrate interface. [Indeed, a SiO_2 precipitate formed within the catalyst would rapidly be expelled from it due to the high surface energy between Au and SiO_2.] The nucleation of SiO_2 is expected to proceed either directly by a reaction such as $2SiO+O_2 \rightarrow 2SiO_2$ or indirectly by the oxidation of a Si precipitate that may form within a silicon-rich surface layer on the catalyst particle.

- **Muliprong Growth**

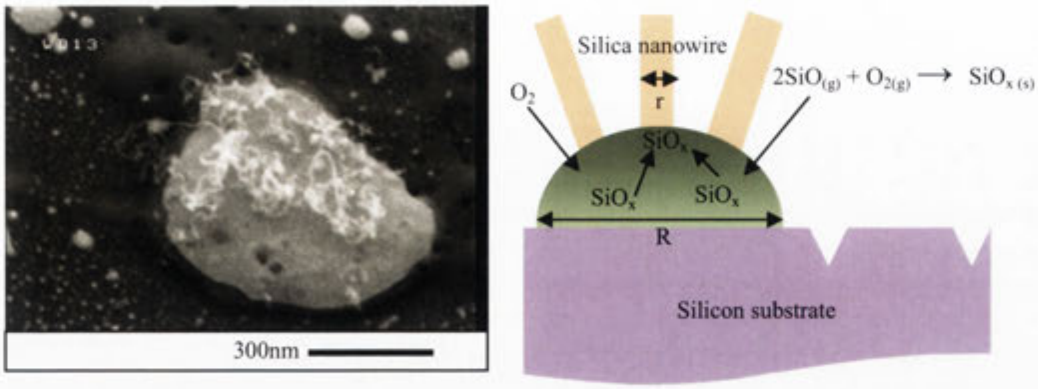

Figure 4.15: SEM image of multiprong mode of silica nanowires and schematic drawing(R>>r).

When the diameter (R) of an alloy particle is much larger than the diameter (r) of nanowires in the root growth mode, there is a high probability for more than one nucleation event to occur. Figure 4.15 shows an example of multiprong growth mode and a schematic drawing of such growth.

B: Silica substrate (with silicon capping layer)

1) The deposition of gold on silicon produces a uniform, continuous thin film of gold across the silicon surface (Fig 4.13 B1)

2) During annealing the Au film breaks up to form relatively small Au islands with large contact angle (θ_f) (Fig 4.13 B2). As the temperature exceeds 1000°C the reaction between the Si capping layer and residual oxygen produces SiO vapour according the reaction described above. Note that this is further facilitated by the evaporation of some Au from the silica substrate onto the capping layer.

3) The gas-phase reactants (SiO and O_2) are absorbed by the Au particles, which at 1100°C are molten (NB: The Au melting temperature is 1063°C). The concentration of

the reactants builds up in the catalyst particle until it exceeds the solubility of a condensed phase, at which point the solution is metastable with respect to the nucleation and growth of this phase. In this case the particle is in contact with a SiO_2 substrate and the reactants can grow SiO_x on this substrate without a nucleation step (Fig 4.13 B3).

4) Condensation of SiO_x at the catalyst-substrate interface forms the base of a SiO_x nanowire and the structure continues to grow by the absorption of gas-phase reactants and their transport to the interface. In this case the catalyst particle maintains its position at the tip of the growing wire and growth is via float growth. This mode of growth leads to a more direct correlation between the size of the catalyst particle and the nanowire diameter, and because the nanowires are anchors at the substrate they tend to be straighter and more regularly aligned (Fig 4.13 B4).

C: More general effects

It is important to note that the nanowire growth mode can be influenced by the source and concentration of the gas-phase reactants, with both root and float growth induced on silicon or silica substrates under appropriate growth conditions. For example, float growth is observed during nanowire growth on a Si substrate when it is annealed with a Si capping layer. In this case, both the substrate and capping layer act as sources of SiO and the concentration of residual O_2 between them is reduced by their physical proximity. Similarly, root growth can be induced on silica substrates by varying the spacing between the substrate and capping layer. This suggests that the dominant nucleation mechanism is sensitive to the concentration and/or concentration gradient of the gas phase reactants. These effects will be explored further in the next section.

4.4 Controlling the growth of nanowires

This section examines the relationship between experimental parameters and nanowire growth.

4.4.1 Growth temperature and time

A: Temperature dependence

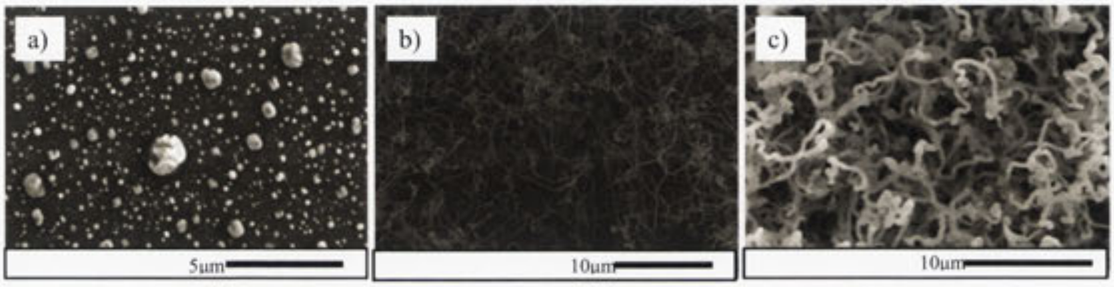

Figure 4.16: SEM images of 10nm Au on Si after annealing at a) 1000°C, b) 1050°C, and c) 1100°C in N_2 ambient.

The annealing temperature is a parameter that is expected to have a direct effect on the growth of nanowires. In particular, it will affect the Au:Si eutectic composition and the reaction rates for SiO production and nanowire growth. From an experimental perspective the range of temperatures investigated in this study was limited to a relatively narrow range between 1000 – 1100°C as nanowires do not form below 1000°C and 1100°C is an upper working limit for fused silica annealing tubes. None-the-less, significant temperature effects were observed, as shown in Figure 4.16. This shows SEM images of a 10nm Au layer on (100) Si substrates after annealing at a) 1000°C, b) 1050°C, and c) 1100°C. No nanowire growth was observed at temperatures at or lower than 1000°C. Although no formal statistical observation of the diameter of the nanowires was undertaken in this case, comparison of the images b) and c) clearly indicate a smaller average diameter and lower density of nanowires grown at 1050°C than is the case after annealing at 1100°C. This effect is most like a result of the increase in SiO concentration[46] as the composition is little different over this temperature range. This conclusion is further supported by the time dependence reported below.

B: Time dependence

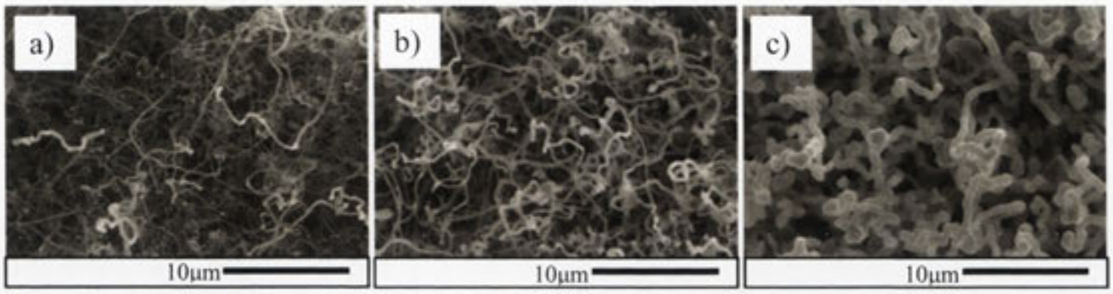

Figure 4.17: SEM images of 10nm Au on Si after annealing at 1100°C for a) 20 min, b) 40 min, and c) 120 min.

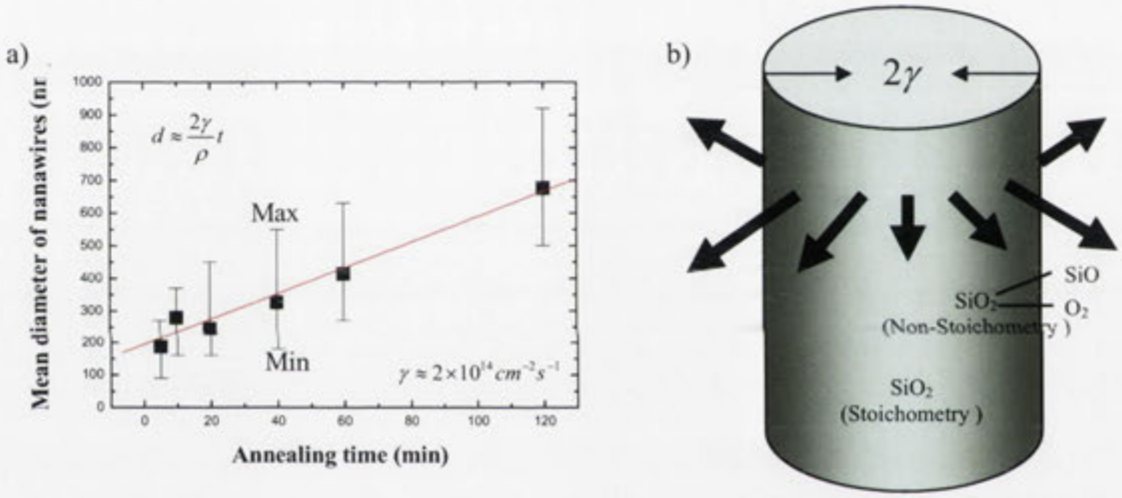

Figure 4.18: a) Diameter of nanowires as a function of annealing time and b) schematic illustration of lateral growth.

The annealing time is another critical factor involved in controlling nanowire growth. Figure 4.17 shows SEM images of nanowires after an annealing time of a) 20, b) 40, and c) 120 minutes. As shown in Figure 4.18 a), the diameter of the nanowires increases linearly with increasing annealing time (note: error bars were determined based on the standard deviation from mean diameter of nanowires). Clearly, the nanowires are undergoing lateral growth that must involve adsorption of SiO vapour onto the nanowire surfaces. As the average stoichiometry of the nanowires is ~$SiO_{1.8}$ this must involve a process in which SiO vapour is adsorbed and reacted chemically with O_2 directly on the nanowire surface via a reaction such as: $2SiO + O_2 \rightarrow 2SiO_2$. The exact stoichiometry of the deposited layer will depend on the efficiency of this reaction and it is plausible that the nanowires have a stoichiometric core (SiO_2) (due to the near equilibrium growth conditions in the liquid eutectic catalyst particle) and non-stoichiometric shell (SiO_x) (due to the incomplete reaction between the adsorbed SiO and residual oxygen), as shown schematically in Figure 4.18 b).

The linear dependence of the nanowire diameter on annealing time is consistent with such a mechanism. For example, for a cylindrical nanowire exposed to a fixed concentration of vapour, the rate of change of volume can be written as: $dV/dt=\gamma A/\rho$, γ is the atomic (or molecular) flux deposited onto the cylinder surface (in $cm^{-2}.s^{-1}$), $A=2\pi rl$ is the approximate surface area of the cylinder, with r the radius and l the length of the cylinder, and ρ is the atomic (molecular) density of the deposited film ($atoms.cm^{-3}$). Since the volume of the cylinder is $V=\pi r^2 l$, the change in the nanowire radius is: $r=2\gamma t/\rho$. i.e. a linear increase with time, as observed. A linear fit to the data in Fig. 4.18 yields a value for γ of around $2\times10^{14} cm^{-2}s^{-1}$ or around 0.1 monolayer per second.

4.4.2 Catalyst formation and the different methods of catalyst preparation

A: Catalyst formation

During the VLS growth mechanism, the metal catalyst plays a critical role in the nucleation and growth of nanowires. In addition, Morales et al[27] have shown a direct correlation between the diameter of the nanowires and the size of the seeding particles. In order to understand the relationship between alloy particles and nanowire growth, three different experimental procedures for introducing the Au catalyst were employed: deposited Au films, ion-implanted Au, and colloidal particles.

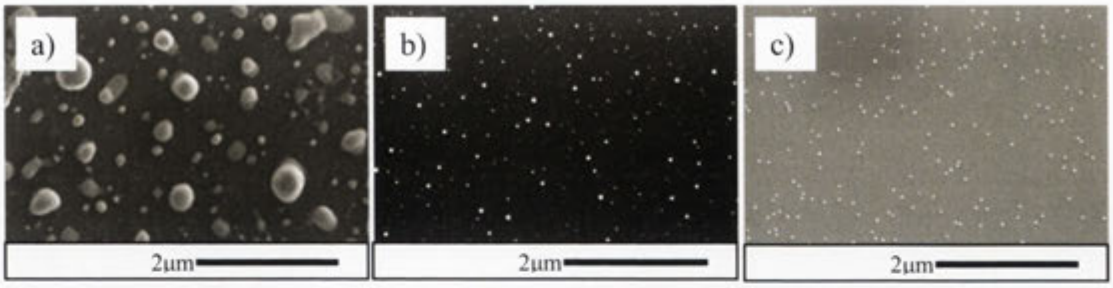

Figure 4.19: SEM images of Au-Si islands after annealing at 900°C depending on formation of Au a) sputtered (10nm thick), b) implanted (3x 10^{16} ion/cm^2 dose), c) colloidal particles (30nm size).

Figure 4.19 shows SEM images of Au-Si islands formed on Si after annealing at 900°C for each of these methods; a) sputtered, b) implanted, and c) colloidal particles. As explained previously, no nanowire growth is expected at this temperature as there is no SiO vapour produced. The size distributions of the particles is clearly very different for each of these cases, reflecting the different amounts of gold available and different formation and coarsening processes. For the sputtered Au films, Au-Si catalyst particles form by islanding and reaction with the silicon substrate, exhibit both very large and very small particles as a direct consequence of their high surface mobility and coarsening (Ostwald ripening) effects[37]. In the case of the Au implanted samples, the volume of Au-Si islands is controlled by the implant fluence and is typically much lower than that available by thin film deposition. During annealing, the implanted Au is segregated to the Si surface and reacts with the silicon to form Au:Si eutectic particles where they remain relatively immobile, thus creating a uniform coverage of small particles[47]. In regard to the colloidal Au catalyst, the coverage is very low and the particle size distribution is predetermined by the colloid preparation. During annealing there is little interaction between the colloid particles, partly because they are so dilute and partly because a lysine layer is used to initially pin the particles on the surface.

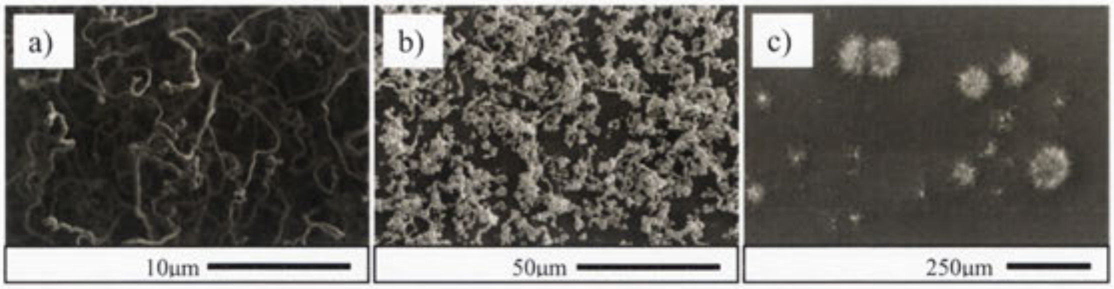

Figure 4.20: SEM images of nanowires after annealing at 1100°C depending on formation of Au a) sputtered (10nm thick), b) implanted ($3x10^{16}$ ion/cm^2 dose), c) colloidal particles (30nm size).

Figure 4.20 shows SEM images of nanowires produced on the samples after annealing at 1100°C. Clearly, each of the prepared samples exhibits its own distinctive Au-Si island formation and corresponding nanowire coverage.

B: Sputtered Au thickness

As discussed above, the density and size distribution of nanowires depend on the method employed for introducing catalyst formation. Sekhar et al[38] have previously shown that the thickness of a deposited Pt catalyst can be used to control the density of silica nanowires, and Elechiguerra et al[48] have reported the growth of denser arrays of thinner nanowires with increasing catalyst layer thickness (using Pt/Au catalysts). In order to investigate such effects in the current study, samples were prepared with different Au thicknesses, ranging from 0.1 to 20nm. Samples were then annealed at 900°C and 1100°C to study the size of catalyst particles and resulting nanowires.

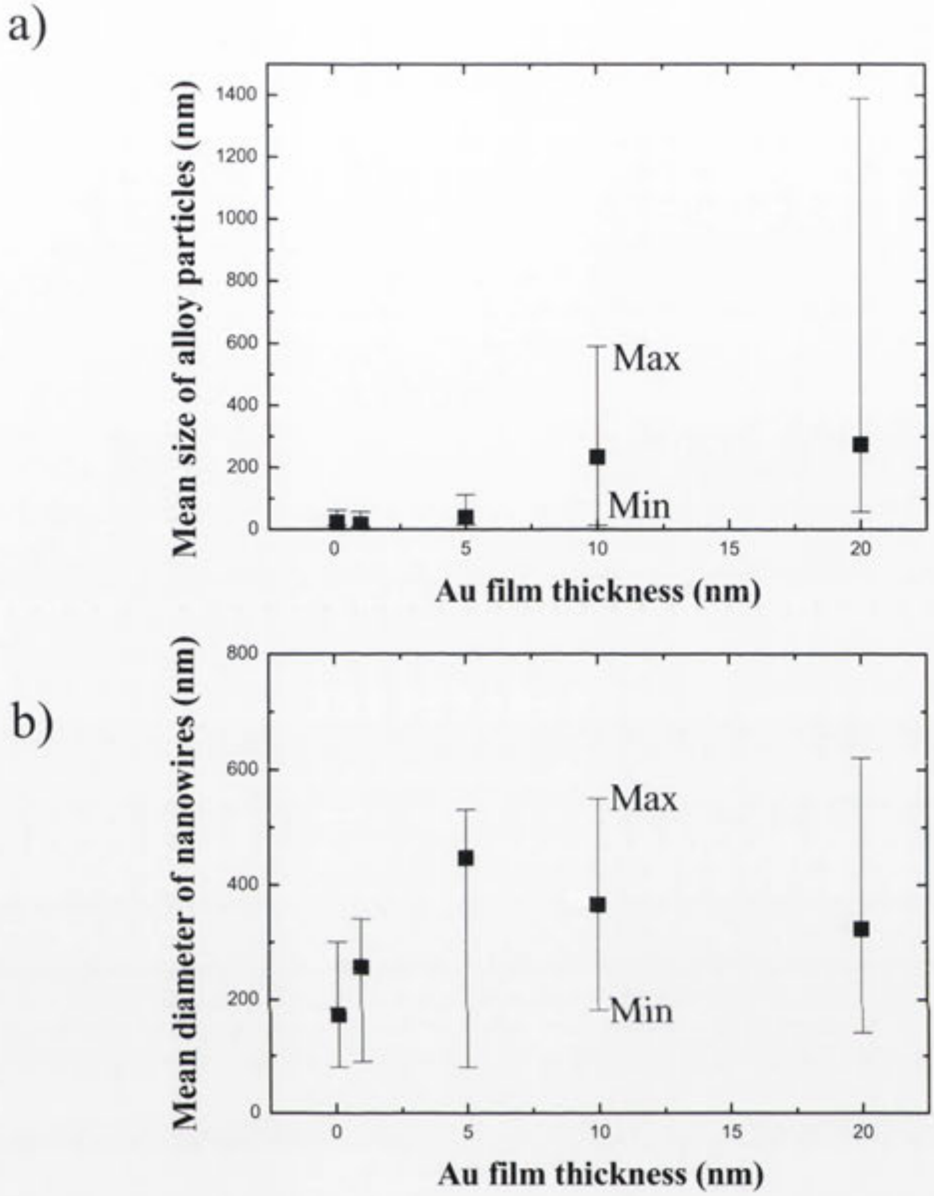

Figure 4.21: Plots of a) mean size of alloy particles versus Au layer thickness after annealing at 900°C, and b) mean diameter of nanowires versus Au layer thickness after annealing at 1100°C.

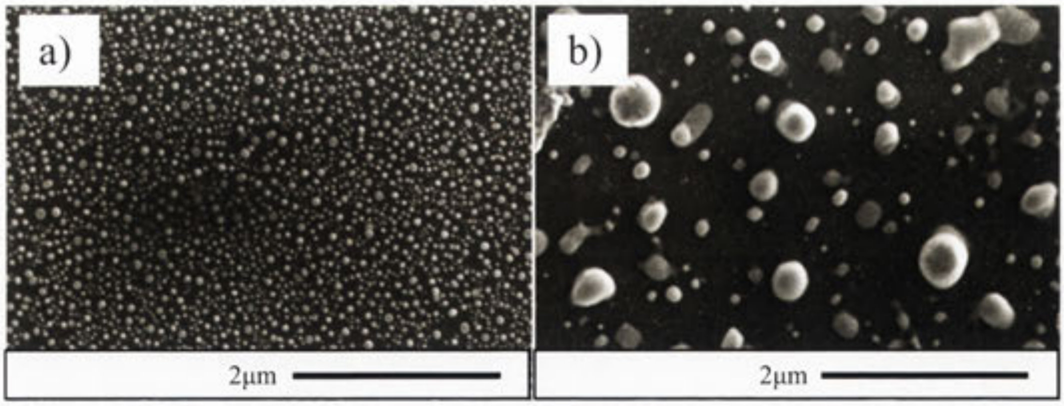

Figure 4.22: Au-Si alloy formed after annealing at 900°C with a) 5nm Au and b) 10nm Au film on Si.

Figure 4.21 shows the mean size of the alloy particles as a function of Au layer thickness and also the mean diameter of nanowires as a function of Au layer thickness. The vertical bars at each point represent the maximum and minimum diameter of nanowires. As the thickness of the Au layer increases, the mean diameter of the alloy particles initially increases and then saturates at ~250nm for layers between 10 and 20nm. However, it is difficult to compare the different distributions with a single statistic due to the large variation in size and changes to bi- and tri-modal distributions (see figure 4.22). Such a comparison is best done by comparing the histograms in Fig 4.23. All such analysis show that increasing the layer thickness increases the maximum size of the particles obtained during annealing.

In contrast, the mean diameter of nanowires grown from these samples first increases and then decreases with Au thickness, although again the distributions are complex and the maximum diameter of nanowires generally increases (see figure 4.24). This observation can be explained by different growth modes of the nanowires and is directly related to the size of alloy particle(s). As discussed previously, the probability for multiprong growth increases with increasing particle size. As an extreme example, Figure 4.25 b) shows multiple wires growing from a single large catalyst particle. In this case the wire diameters are a small fraction of the particle diameter. This is stark contrast to the wire shown in Fig. 4.25 a) which represents single-prong growth of a nanowire. Because the thicker Au layers produce larger catalyst particles, the fraction of nanowires produced by multiprong growth will also increase with film thickness. As these wires are typically much thinner than those produced by single prong growth, the average nanowire diameter will decrease.

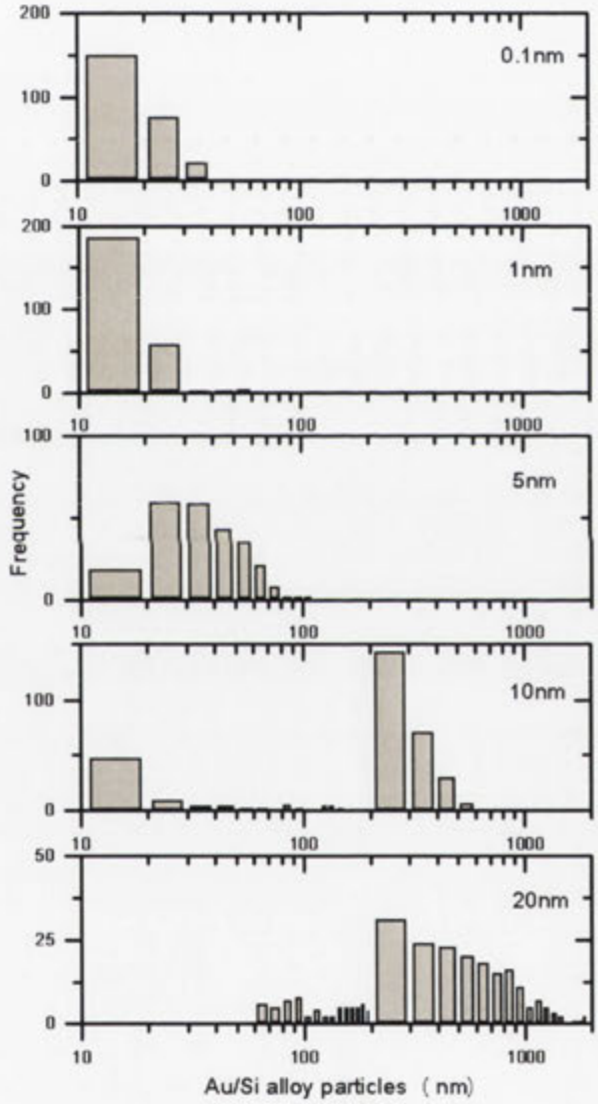

Figure 4.23: Histogram showing the size distribution of Au-Si alloy particles as a function of Au film thickness.

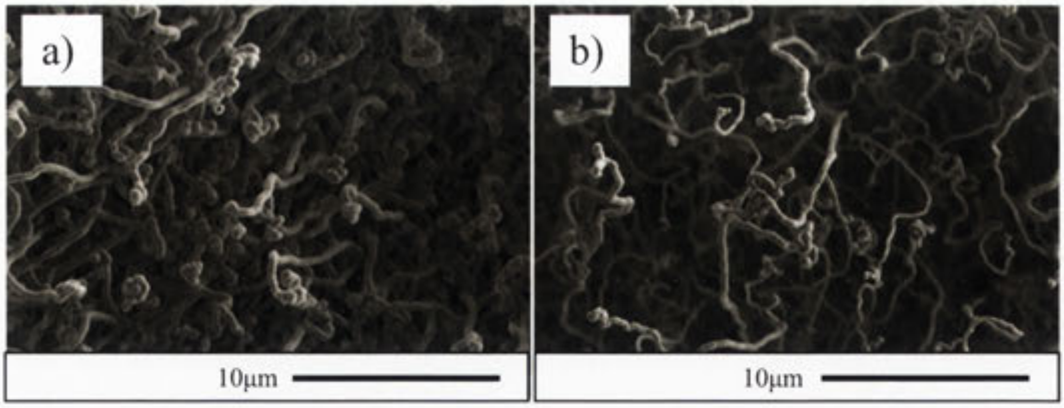

Figure 4.24: Silica nanowires grown after annealing at 1100°C with a) 5nm Au and b) 10nm Au film.

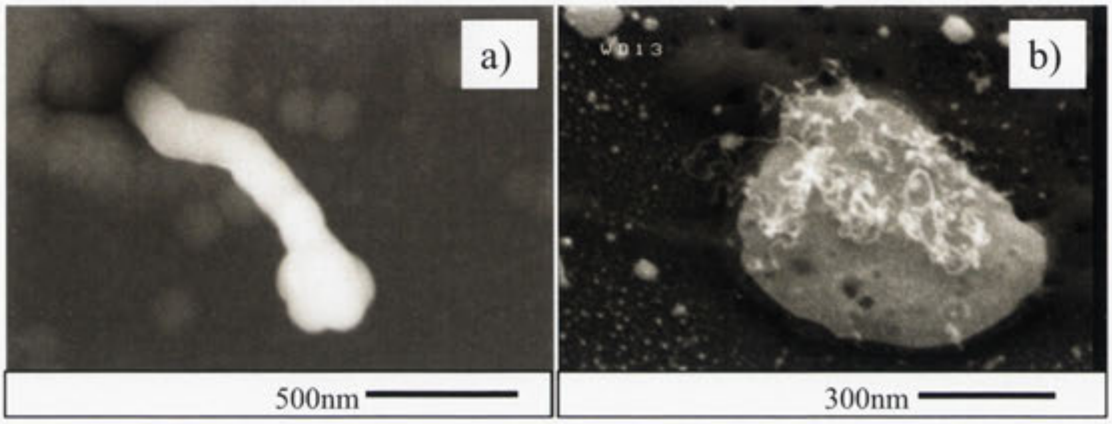

Figure 4.25: SEM images of a) single mode and b) multiprong mode growth of nanowires.

C: Implanted Au fluence and colloid Au size

For comparison, similar measurements were performed as a function of implant fluence for Au-implanted silicon samples, and as a function of Au colloid diameter in the case of colloidal-deposition.

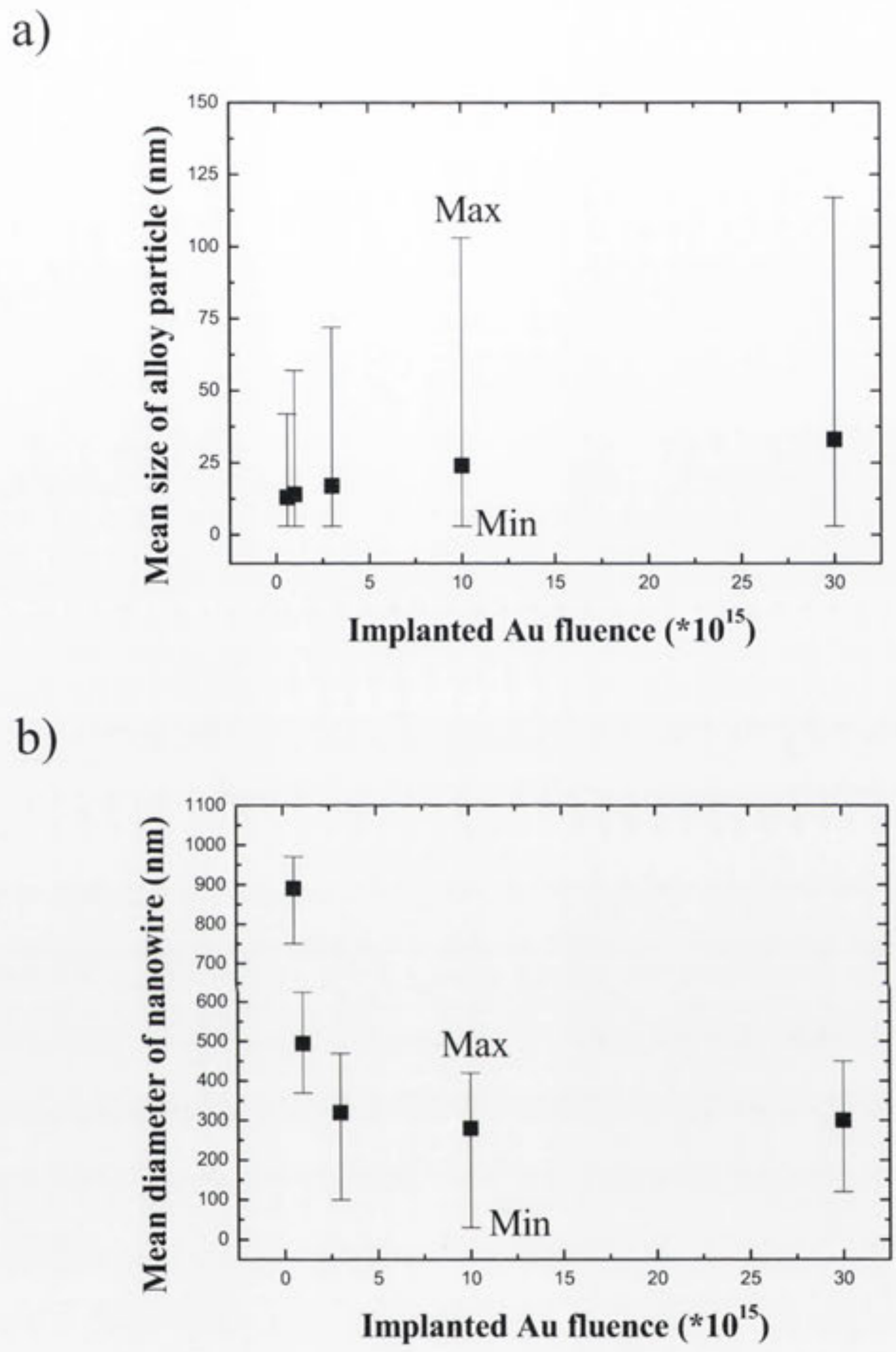

Figure 4.26: Plots of a) mean size of alloy particles versus implanted Au fluence and b) mean diameter of nanowires versus implanted Au fluence.

Figure 4.26 shows: a) mean Au-Si catalyst size and b) mean diameter of nanowires as a function of a implanted Au fluence onto (100) Si samples. As for the studies above, the catalyst particles were formed by annealing at 900°C for 1 hour and nanowires were synthesized by annealing at 1100°C for 1 hour, both in a flowing N_2 ambient. Comparison with the thin film data reveals some important similarities and distinct differences, again largely related to details of the catalyst size distribution. In this context it should be noted that an implant fluence of 3×10^{16} $Au.cm^{-2}$ is equivalent to a ~5nm thick thin-film in terms of total Au content. Taking this into account, a comparison of the mean catalyst particle sizes shows that they are similar to within about 20-30% (except for the lowest fluence implant where the difference is a little higher). In contrast, the mean nanowire diameter is much larger (4-5 times) at the lowest fluences than for the equivalent thin film samples, and appears to saturate at a diameter similar to that observed for thicker deposited films. Moreover, over the range of interest, the mean nanowire diameter decreases with increasing fluence while increasing with increasing deposited film thickness. The reason for these differences remains unresolved but they mainly occur for films with very low equivalent thickness where the density of catalyst particles is extremely low. Under these circumstances it is possible that the catalyst particles undergo additional coarsening between 900 and 1100°C and that this occurs preferentially for the implanted samples due to a higher surface mobility of eutectic particles in this case. In these samples Au is pre-mixed with Si and is segregated to the silicon surface as a thin layer of eutectic, whereas Au films undergo islanding and react locally with the Si substrate to form eutectic particles. The latter produces a slight depression under the eutectic particles which tends to reduce their mobility. Further work is required to resolve this issue.

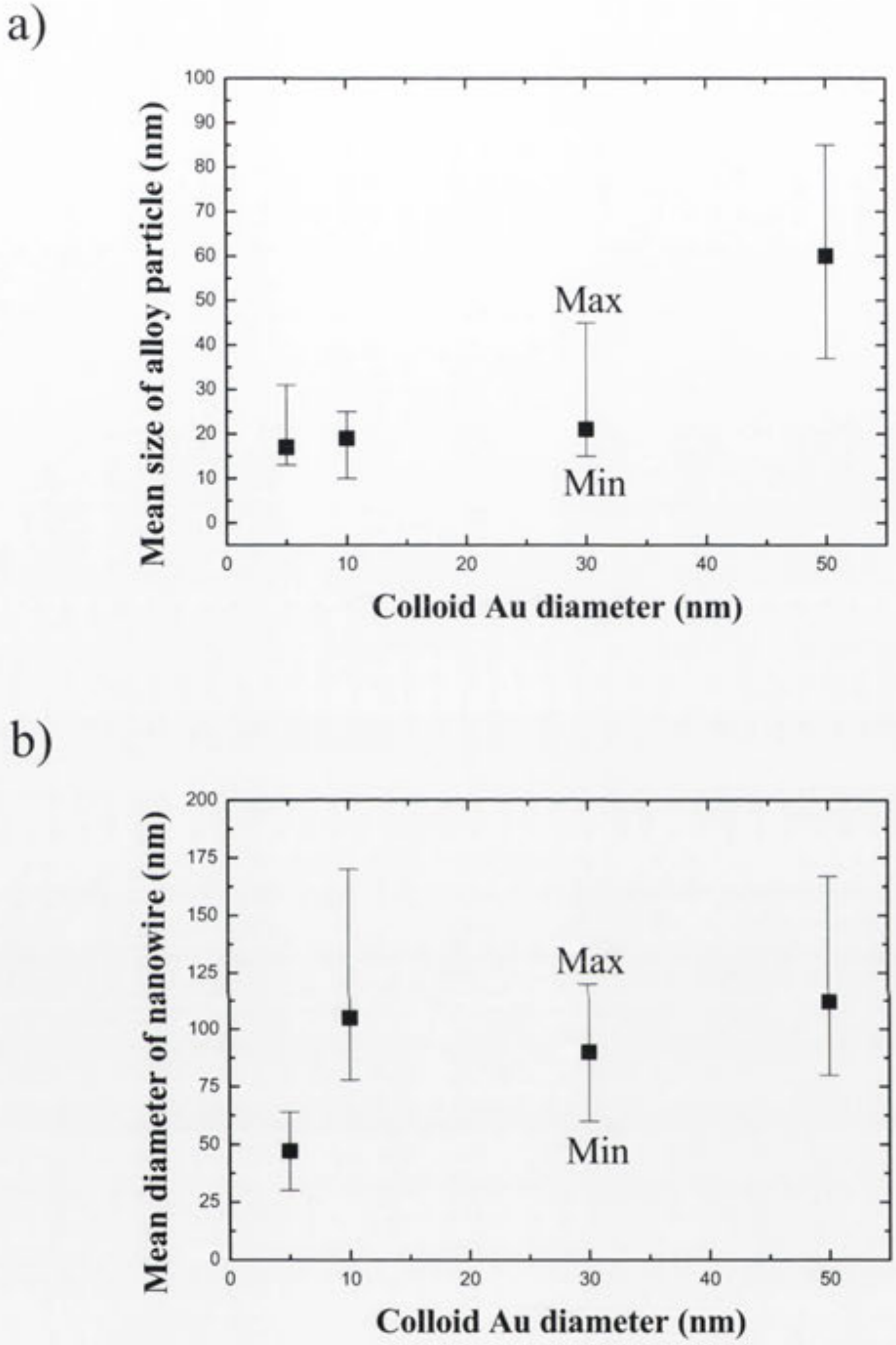

Figure 4.27: Plots of a) mean size of alloy particles versus colloid Au diameter and b) mean diameter of nanowires versus Au colloids.

The situation for colloidal Au particles is summarized in Fig. 4.27. In this case the colloidal particles have a uniform size distribution and are sufficiently dilute that they do not interact. After annealing at 900°C the size of Au colloidal particles increases slightly due to alloying with Si, as shown in Fig. 4.27 a). This is due to particles adsorbing additional Si from the Si substrate and because of changes in shape associated with changes in wetting behaviour (contact angle)[37]. The size of the corresponding nanowires after annealing at 1100°C is shown in Figure 4.27 b). In this case the size of the nanowires show no clear trend with particle size, although there is a factor of ~2.3 between the mean nanowire diameters of the smallest and largest catalyst particles compared to a factor of ~3.5 for the corresponding catalyst particles. In this context we note that correlations of the type presented here are fraught with difficulties. For example, the size of catalyst particles depends on their silicon content and when cooled to room temperature for observation they undergo phase separation such that small particles are almost completely denuded of silicon (it precipitates at the interface with the substrate) while larger particles separate internally, as discussed earlier. This combined with changes in particle shape can lead to an underestimate of the small-particle component of the particle size distribution. Comparing nanowire size distributions with those of the catalyst particles is also complicated by the fact that the wires often exhibit significant lateral growth, as discussed in section 4.4.1. As this depends on the vapour-phase concentration of SiO produced by reaction with the silicon substrate it is a sensitive function of the exposed Si area and nanowire density.

4.4.3 Other parameters influencing nanowire growth

The self-sourcing nanowire growth technique investigated in this work relies on the production of a vapour-phase source of SiO produced by a reaction between O_2 and Si. The concentration of vapour available therefore depends on the concentration and proximity of the silicon source, and on the reaction rates between oxygen and silicon. This section serves to highlight the significance of such effects rather than provide a detailed and systematic investigation of them.

A: Crystal orientation

Silicon nanowires (SiNWs) with small diameters tend to grow primarily along <110> directions, whereas SiNWs with larger diameters tend to grow along <111> directions. As a consequence, well-aligned SiNW arrays form ordered networks on single crystal substrates corresponding to low-free-energy structures, and their orthographic projections on (100), (110), and (111) substrates form rectangular patterns, parallel straight lines, and triangular network, respectively[33]. In the present study, the growth direction of silica nanowires is not correlated with the crystal orientation of the substrate and no differences for different diameter wires are observed. This supports a model in which SiO_2 nanowires are nucleated directly rather than via the growth and subsequent oxidation of silicon nanowires.

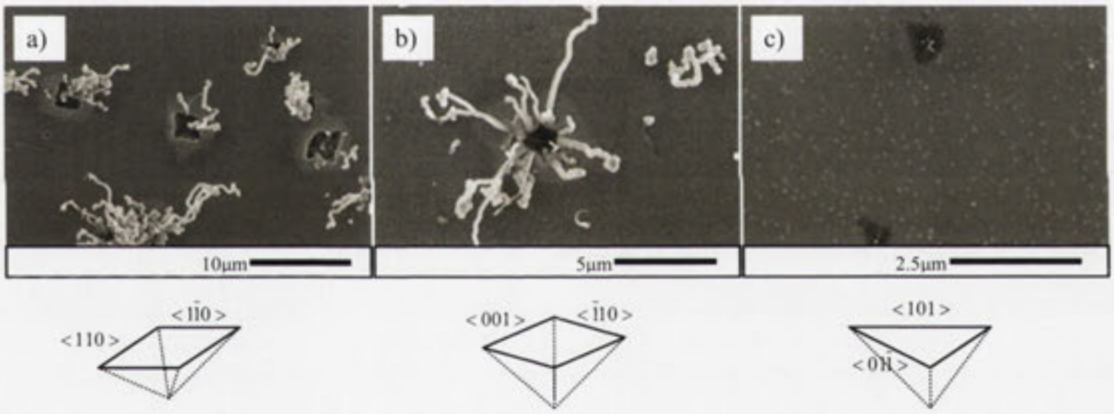

Figure 4.28: SEM images of etch pits depending on crystal orientation of a) (100), b) (110), and c) (111) substrate and schematic illustrations, respectively.

However, the substrate orientation might reasonably be expected to play some role in the nucleation and growth of silica nanowires due to variations in the reactivity of differently oriented Si surfaces. Such differences are evident from the shapes of etch pits produced in the silicon substrate by reaction with residual oxygen, as shown in Figure 4.28. These samples were coated with Au colloid particles prior to annealing in N_2 atmosphere at 1100°C for 1 hour. The etch pits show well defined facets on (100),

(110) and (111) surfaces consistent with previous studies[40]. Significantly, no etch pits were observed on substrates when annealed without Au, confirming the catalytic role of Au in enhancing the $2Si+O_2 \rightarrow 2SiO$ reaction. The effect of oxygen etching will be discussed further in chapter 5.

B: Alternative substrates

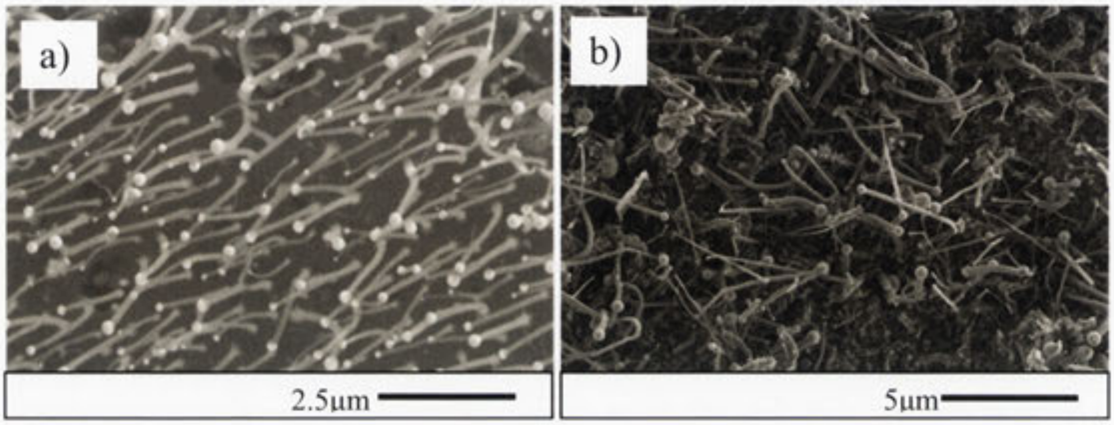

Figure 4.29: SEM images of nanowires grown on a) silica and b) silicon rich oxide film($SiO_{1.16}N_{0.32}$:H) after annealing at 1100°C in N_2 ambient for 1 hour with Si capping layer.

Thin films such as silicon dioxide or silicon-rich oxide are useful substrates in many practical biological and environmental sensing applications and in micro-electro-mechanical (MEMS) systems. The incorporation of silica nanowires into such structures is therefore of interest. Although a Si substrate often exists under the thin film, no nanowires are observed without the provision of an additional Si source because the thin film prevents the formation of Au-Si alloy particles and the chemical reaction required to produce the requisite SiO vapour source. On the other hand, float growth of nanowires is observed after annealing (at 1100°C in N_2 ambient for 1hour) 10nm Au coated layers on 100nm thermal silicon dioxide and silicon rich oxide ($SiO_{1.16}N_{0.32}$:H deposited by PECVD) films onto Si substrate covered with a Si capping layer, as shown in figure 4.29.

C: Source proximity effects

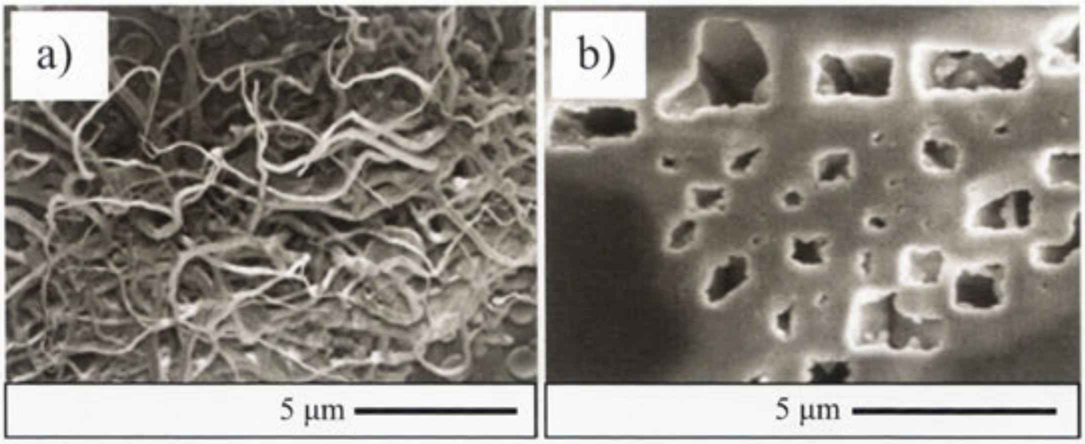

Figure 4.30: SEM images of a) nanowires grown on silica after annealing 10nm Au film on silica at 1100°C in N_2 ambient for 1 hour with Si capping layer depending on distance (>100 μm) between silica and Si capping layer and b) Si capping layer.

The growth of nanowires from secondary sources of SiO is also affected by the distance between film and capping (source) layer. For example, high densities of extremely thin nanowires are observed on silica substrates when the distance between the silica film and capping layer is appropriately adjusted, as shown in figure 4.30 a). For separations of about 25μm, float growth of nanowires (Figure 4.29 a) is observed. However, at larger separations, > 25μm, high densities of thin wires are observed. No nanowires are observed on the Si capping layer annealed with sample of Figure 4.30 a), as shown in Figure 4.30 b), but it does exhibit severe etching due to the reaction with O_2 to produce SiO. Increasing the separation between the substrate and capping layer affects the concentration and concentration gradient of SiO vapour at the point of growth. However, the details of this effect are complicated by the fact that the proximity of the capping layer affects the local O_2 partial pressure between the wafers, as well as the distribution of SiO vapour emitted from the capping wafer. (i.e. increasing the separation between the substrate and capping-layer increases the O_2 partial pressure between wafers and thereby increases the production of SiO, but the SiO concentration also decreases with distance from the capping layer and therefore decreases at the point of growth with increasing separation.) Clearly such effects can have a dramatic influence on the density and structure of the resulting nanowires and can be used to produce optimal structures for particular applications. The trends reported above are summarized in the schematic of Figure 4.31.

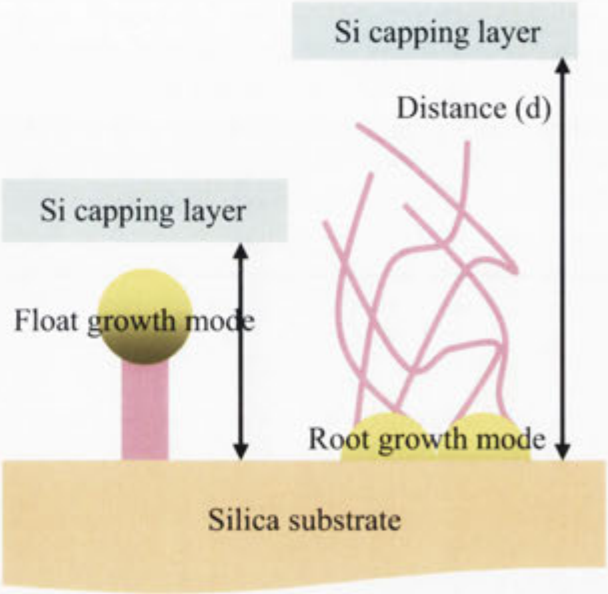

Figure 4.31: Schematic illustration of growth mode of silica nanowires grown on silica after annealing with Si capping layer depending on the distance between capping layer and substrate.

D: Concentration gradient of vapour source

The mode of growth (root versus float) and the density and structure of nanowires is a sensitive function of growth conditions and is influenced by both the concentration and concentration gradient of gas phase reactants. This is evident from Figure 4.32 which shows a typical SEM image of nanowires grown on Si after annealing with a Si capping layer. In this case both the silicon substrate and capping layer act as sources of SiO vapour but the concentration of residual O_2 decreases with increasing distance from the edge of the sample due to the proximity of the substrate and capping wafer. In this case, float growth of nanowires is observed over most of the growth area (part A), as shown in Fig 4.32 a). These nanowires have a relatively low density and typical lengths of

5~6μm and diameters of 150~250nm. This is consistent with the fact that the SiO production rate in this region is reduced by the availability of O_2. On the other hand, figure 4.32 b) shows a SEM image of nanowires taken at the edge (part B) of the same sample. In this case nanowire growth occurs via root growth (i.e. no Au is observed on the head of the wires). These wires have an average length of 40~50μm and an average diameter of 1~1.5μm. They are also present at high density relative to those in region A. Significantly, the wires also show strong alignment along the direction of maximum SiO concentration gradient, as determined from the sample geometry. i.e. The alignment is most evident within 0.2-0.3 mm of the sample edge. Figure 4.32 d) shows a schematic of the SiO concentration gradient in each area (part A and B) during annealing with a Si capping layer. (The concentration of O_2 is expected to decrease with increasing distance from the sample edge).

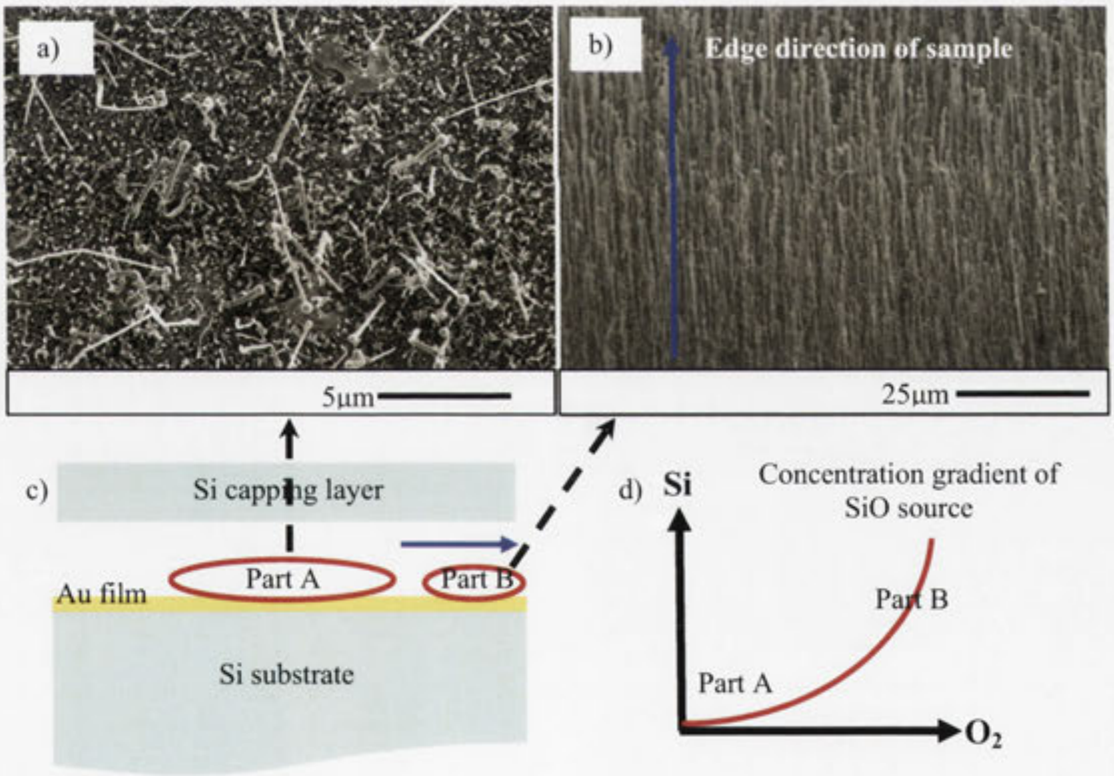

Figure 4.32: a) SEM image of float growth nanowires observed on most of the sample, b) SEM image of root growth nanowires observed in edge area of sample, c) schematic illustration of sample structures, and d) expected concentration gradient of SiO source in part A and B.

4.5 Summary

In summary, this chapter has investigated the synthesis of silica nanowires on Au-coated substrates using a simple self-sourcing process and highlighted some of the experimental dependencies of the growth process. Details of the synthesis process were investigated and a model of nanowire growth proposed. The latter is based on the production of SiO as a vapour phase source of Si and O via by a reaction between Si and residual oxygen, present in the annealing ambient at 3-10ppm, described by: $2Si+O_2 \rightarrow 2SiO$. The dominance of this reaction over the competing reaction: $Si+O_2 \rightarrow SiO_2$ is a strong function of oxygen concentration and temperature and for the fixed oxygen concentration employed in this study, limits growth to the temperature range $>1000^{o}C$. The SiO vapor produced is absorbed by metal (Au) catalyst particles and facilitates nanowire growth via a VLS growth mechanism. The formation of catalyst particles and the relationship between the size of these particles and that of the resulting nanowires was explored in some detail. More subtle growth modes were also investigated, including the growth of nanowires on substrates other than silicon in which a secondary source of SiO was produced by including a Si capping wafer in the vicinity of the substrate. The influence of experimental parameters on the structure and morphology of the nanowires was also reported.

Although the work reported here has concentrated on the use of Au as the metallic catalyst, similar results were observed for other catalysts, including Ni, Pt and Pd.

4.6 References

[1] D. P. Yu, Q. L. Hang, Y. Ding, H. Z. Zhang, Z. G. Bai, J. J. Wang, Y. H. Zou, W. Qian, G. C. Xiong, S. Q. Feng, *Applied Physics Letters* **1998**, *73*, 3076.

[2] X. C. Wu, W. H. Song, K. Y. Wang, T. Hu, B. Zhao, Y. P. Sun, J. J. Du, *Chemical Physics Letters* **2001**, *336*, 53.

[3] S. O. Obare, N. R. Jana, C. J. Murphy, *Nano Letters* **2001**, *1*, 601.

[4] Y. D. Yin, Y. Lu, Y. G. Sun, Y. N. Xia, *Nano Letters* **2002**, *2*, 427.

[5] N. Wang, Y. Cai, R. Q. Zhang, *Materials Science & Engineering R-Reports* **2008**, *60*, 1.

[6] B. K. Teo, X. H. Sun, *Chemical Reviews* **2007**, *107*, 1454.

[7] S. Kuchibhatla, A. S. Karakoti, D. Bera, S. Seal, *Progress in Materials Science* **2007**, *52*, 699.

[8] W. Lu, C. M. Lieber, *Journal of Physics D-Applied Physics* **2006**, *39*, R387.

[9] K. W. Kolasinski, *Current Opinion in Solid State & Materials Science* **2006**, *10*, 182.

[10] Y. F. Zhang, Y. H. Tang, N. Wang, D. P. Yu, C. S. Lee, I. Bello, S. T. Lee, *Applied Physics Letters* **1998**, *72*, 1835.

[11] J. Westwater, D. P. Gosain, S. Tomiya, S. Usui, H. Ruda, *Journal of Vacuum Science & Technology B* **1997**, *15*, 554.

[12] H. I. Liu, D. K. Biegelsen, F. A. Ponce, N. M. Johnson, R. F. W. Pease, *Applied Physics Letters* **1994**, *64*, 1383.

[13] N. Ozaki, Y. Ohno, S. Takeda, *Applied Physics Letters* **1998**, *73*, 3700.

[14] S. H. Li, X. F. Zhu, Y. P. Zhao, *Journal of Physical Chemistry B* **2004**, *108*, 17032.

[15] M. Paulose, O. K. Varghese, C. A. Grimes, *Journal of Nanoscience and Nanotechnology* **2003**, *3*, 341.

[16] Z. J. Zhang, G. Ramanath, P. M. Ajayan, D. Goldberg, Y. Bando, *Advanced Materials* **2001**, *13*, 197.

[17] H. F. Zhang, C. M. Wang, E. C. Buck, L. S. Wang, *Nano Letters* **2003**, *3*, 577.

[18] D. Dwivedi, R. Dwivedi, S. K. Srivastava, *Sensors and Actuators B-Chemical* **2000**, *71*, 161.

[19] Y. J. Zhang, N. L. Wang, R. R. He, J. Liu, X. Z. Zhang, J. Zhu, *Journal of Crystal Growth* **2001**, *233*, 803.

[20] Y. F. Zhang, Y. H. Tang, N. Wang, C. S. Lee, I. Bello, S. T. Lee, *Journal of Crystal Growth* **1999**, *197*, 136.

[21] D. P. Yu, Y. J. Xing, Q. L. Hang, H. F. Yan, J. Xu, Z. H. Xi, S. Q. Feng, *Physica E* **2001**, *9*, 305.

[22] R. S. Wagner, W. C. Ellis, *Applied Physics Letters* **1964**, *4*, 89.

[23] Y. Y. Wu, P. D. Yang, *Chemistry of Materials* **2000**, *12*, 605.

[24] Y. Wu, Y. Cui, L. Huynh, C. J. Barrelet, D. C. Bell, C. M. Lieber, *Nano Letters* **2004**, *4*, 433.

[25] Y. Cui, X. F. Duan, J. T. Hu, C. M. Lieber, *Journal of Physical Chemistry B* **2000**, *104*, 5213.

[26] R. G. Elliman, A. R. Wilkinson, T. H. Kim, P. K. Sekhar, S. Bhansali, *Journal of Applied Physics* **2008**, *103*.

[27] A. M. Morales, C. M. Lieber, *Science* **1998**, *279*, 208.

[28] N. R. B. Coleman, M. A. Morris, T. R. Spalding, J. D. Holmes, *Journal of the American Chemical Society* **2001**, *123*, 187.

[29] N. R. B. Coleman, N. O'Sullivan, K. M. Ryan, T. A. Crowley, M. A. Morris, T. R. Spalding, D. C. Steytler, J. D. Holmes, *Journal of the American Chemical Society* **2001**, *123*, 7010.

[30] D. Shir, B. Z. Liu, A. M. Mohammad, K. K. Lew, S. E. Mohney, *Journal of Vacuum Science & Technology B* **2006**, *24*, 1333.

[31] N. Fukata, T. Oshima, N. Okada, K. Murakami, T. Kizuka, T. Tsurui, S. Ito, *Journal of Applied Physics* **2006**, *100*.

[32] A. I. Hochbaum, R. Fan, R. R. He, P. D. Yang, *Nano Letters* **2005**, *5*, 457.

[33] S. P. Ge, K. L. Jiang, X. X. Lu, Y. F. Chen, R. M. Wang, S. S. Fan, *Advanced Materials* **2005**, *17*, 56.

[34] B. Fuhrmann, H. S. Leipner, H. R. Hoche, L. Schubert, P. Werner, U. Gosele, *Nano Letters* **2005**, *5*, 2524.

[35] D. Gao, R. R. He, C. Carraro, R. T. Howe, P. D. Yang, R. Maboudian, *Journal of the American Chemical Society* **2005**, *127*, 4574.
[36] D. Wang, F. Qian, C. Yang, Z. H. Zhong, C. M. Lieber, *Nano Letters* **2004**, *4*, 871.
[37] B. Ressel, K. C. Prince, S. Heun, Y. Homma, *Journal of Applied Physics* **2003**, *93*, 3886.
[38] P. K. Sekhar, S. N. Samhandam, D. K. Sood, S. Bhansali, *Nanotechnology* **2006**, *17*, 4606.
[39] X. M. Meng, J. Q. Hu, Y. Jiang, C. S. Lee, S. T. Lee, *Applied Physics Letters* **2003**, *83*, 2241.
[40] T. Suzuki, *Journal of Applied Physics* **2000**, *88*, 6881.
[41] C. Gelain, A. Cassuto, P. Le Goff, *Oxidation of Metals* **1971**, *3*, 139.
[42] J. J. Lander, J. Morrison, *Journal of Applied Physics* **1962**, *33*, 2089.
[43] A. Cros, J. Derrien, F. Salvan, *Surface Science* **1981**, *110*, 471.
[44] D. Bahloul-Hourlier, P. Perrot, *Journal of Phase Equilibria and Diffusion* **2007**, *28*, 150.
[45] N. Ferralis, R. Maboudian, C. Carraro, *Journal of the American Chemical Society* **2008**, *130*, 2681.
[46] H. Z. Zhang, D. P. Yu, Y. Ding, Z. G. Bai, Q. L. Hang, S. Q. Feng, *Applied Physics Letters* **1998**, *73*, 3396.
[47] T. Stelzner, G. Andra, E. Wendler, W. Wesch, R. Scholz, U. Gosele, S. Christiansen, *Nanotechnology* **2006**, *17*, 2895.
[48] J. L. Elechiguerra, J. A. Manriquez, M. J. Yacaman, *Applied Physics a-Materials Science & Processing* **2004**, *79*, 461.

Chapter 5

Hybrid metal-silica nanowire structures and their optical properties

This chapter presents results on the synthesis and characterization of metal:silica-nanowire hybrid nanostructures including the fabrication of self-supporting nanowire films, optically-doped nanowires, structures based on secondary nanowire growth, metal-decorated nanowires, and metal peapod and core-shell structures. Such structures have enormous potential as optically-based sensing elements based on plasmon resonance effects and luminescence emission, and as large surface area catalyst substrates.

In order to fabricate these hybrid structures the nanowire growth was controlled by various methods including the use of optically active metals as catalysts for growth, the use of capping layers to promote float growth, and post growth metal deposition and annealing. The optical properties of selected structures were also examined using Fourier-transform infra-red spectroscopy (FTIR), optical absorption, and photoluminescence analysis.

5.1 Introduction

During the past decades, hybrid nanostructures have attracted attention because of their novel optical and electronic properties and their potential for applications such as nanoscale optoelectronics[1-3], sensors[4, 5] and 1D quantum devices[6, 7]. Noble-metal nanoparticles encapsulated in a dielectric matrix are particularly interesting for ultrafast optical switching devices[8, 9] owing to their nonlinear and fast optical response near the surface-plasmon-resonance(SPR) frequency and in quantum devices[6, 7] due to the effect of quantum tunneling between conducting particles near percolation threshold. Various methods such as the sol-gel process, metal-dielectric deposition by co-sputtering, metal-ion implantation into dielectric matrix, and pulsed laser deposition have been applied for metal-dielectric nanocomposite synthesis[10-12]. More recently, interest has turned to chains of one dimensional noble metal-dielectric nanoparticles, rather than the thin film or bulk form, because it has been shown theoretically and experimentally that electromagnetic energy can be transported below the diffraction limit of light, along such chains of closely spaced noble nanoparticles through a coupled-plasmon mode[13, 14]. These 'Peapod' type structures are one of best known examples of one-dimensional hybrid nanostructures and their unusual properties offer a promising opportunity to achieve a wide variety of functionalities[15, 16]. Recently, Hu et al reported the fabrication of self-organized gold-peapod silica nanowires using a microreactor system and demonstrated SPR-induced conductivity in these structures[17].

Core-shell or multi core-shell nanostructures are also of great theoretical and technological interest. Silica is commonly employed for the fabrication of such 0-dimensional structures because of its thermal and chemical stability and ease of control of the deposition process. A variety of materials, including Au, Ag, Fe, metal oxides and semiconductors have been coated with silica shells or supported by a silica core. These structures are formed by surface modification and/or functionalization of the nanostructures during synthesis process or post-processing[18-20]. Thermal evaporation techniques[21] or metal ion or colloid reduction in solution[22-25] can be employed for fabrication of such core-shell structures and such structures are good candidates for investigating plasmon resonance effects[26].

The composition of nanowires has a profound impact on their performance as fabricated nanodevices. In order to control the composition of the nanowires, doping methods such as implantation or sputtering have been employed during or after nanowire growth. The electrical properties of nanowires have been controlled with boron or phosphorous during growth process[27-31], and optical doping was performed by ion-implantation of rare-earth ions to enhance photoluminescence emission[32, 33]. Since the strong intrinsic luminescence from as grown silica nanowires have been reported[34], several studies have been performed on optical doping and functionalization of such materials[33, 35, 36]. Self-organized growth of optically doped nanowires and associated hybrid structures and their luminescence had also reported by Choi et al[37].

5.2 Experimental details

The substrates employed for this study consisted of (100) orientated silicon wafers, fused silica plates, 100nm thick SiO_2 film grown on (100) Si by thermal oxidation, and 100nm thick silicon rich oxide films (SRO) deposited onto (100) Si by PECVD. Gold (Au), Nickel (Ni), and Erbium (Er) catalyst layers of ~10nm thickness were deposited on the substrates by sputter deposition. In one particular case, co-deposition of Au and Er was employed for in-site doping of the nanowires. Samples were annealed at temperatures close to 1100°C for 1 hour in N_2 ambient at 100sccm to induce the growth of silica nanowires. In some cases, the samples were placed face (metal side) down on a (100) silicon wafer which was used to provide an indirect Si vapour source, during the annealing process. A few samples were re-annealed at temperatures close to 1100°C for 15~20min in N_2 ambient after the removal of the Si capping layer. For fabricating hybrid structures and postdoping experiments, Er and Au were re-sputtered on as-grown silica nanowires and subsequently re-annealed at temperatures close to 1100°C for 1 hour in O_2 or N_2 ambient.

The morphology of the nanowires and the relationship between the catalyst and the nanowires were observed by scanning electron microscopy (SEM) [Hitachi field emission scanning microscopy (FE-SEM)] equipped with an energy dispersive X-ray (EDX) detector and backscattering detector. High resolution transmission election microscopy (HRTEM) with energy dispersive spectroscopy (EDS) was also utilized to analyze the structure and the composition of nanowires.

Absorption FTIR spectra were measured with a Perkin-Elmer FTIR system 2000 spectrometer at room temperature and UV-visible absorption spectra were measured with spectrophotometer (Varian cary 5000) in the range 300~1200nm. In addition, the optical properties of nanowires were studied by photoluminescence (PL). The UV-visible emission was measured under excitation with a 325nm emission from a He-Cd laser. The luminescence emission was collected using a grating monochromator and a GaAs photomultiplier. Standard lock-in techniques were also used for signal detection. PL measurement in the infra-red range (1400-1600nm) was performed under 488nm excitation from an Ar-ion laser. Emitted light was collected by using Triax 320 spectrometer equipped with a high sensitivity liquid-nitrogen-cooled germanium detector. Standard lock-in techniques were also employed for these PL measurements.

5.3 Experimental results

5.3.1 Self-supporting nanowire films

As discussed in Chapter 5, nanowire synthesis under the conditions employed in the current study involves etching of the Si substrate via a reaction with O_2 to produce SiO, i.e. $2Si+O_2 \rightarrow 2SiO$. This produces facetted etch pits in the Si surface. During extended annealing the density and extent of these etch pits increases to the point where they overlap and decouple the growing film from the substrate. This process can be accelerated by re-depositing metal onto the nanowire film and reheating at 1100°C to diffuse the metal to the active interface. This enhances the etching process via the catalytic action of the metal. Figure 5.1 a) shows such a self-supporting film of silica nanowires. Figure 5.1 b) and c) show front and reverse side of this film. Silica nanowires, similar to what has been seen previously, were observed from front side with a small number of wires on reverse side. This film is flexible and mechanically robust and can readily be handled with a pair of tweezers. The role of the etching is clearly evident in Fig. 5.1 d) which shows a cross-sectional SEM image of the sample prior to complete layer release, and in Fig. 5.1 e) which shows a plan view image of the Si surface after film release. Such films have enormous potential as biological or environmental sensors due to their large surface to volume fraction and this process is the subject of a provisional patent.

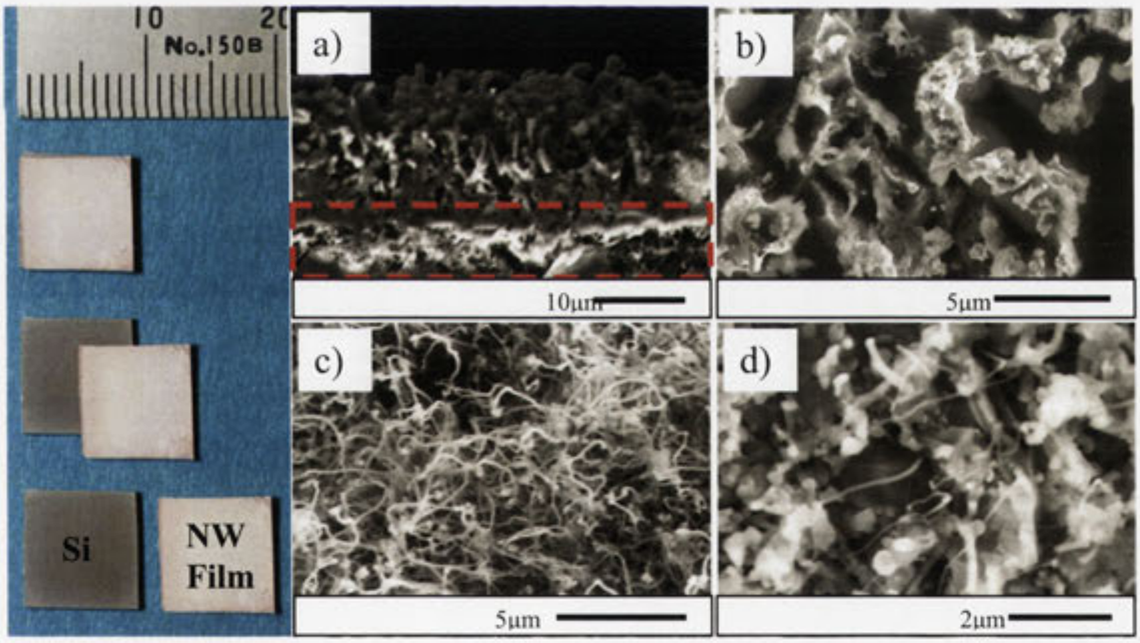

Figure 5.1: (*left panel*) Photographs of a spontaneously delaminated nanowire film and the the silicon substrate on which it was grown. (*right panels*) a) cross-sectional SEM image of the substrate-nanowire interface (red box), b) an SEM image of the Si substrate after film delamination, c) an SEM image of the top surface of the nanowire film, and d) an SEM image of the substrate-side of the self-supporting nanowire film.

5.3.2 Intrinsic optical properties of silica nanowires

A: FTIR

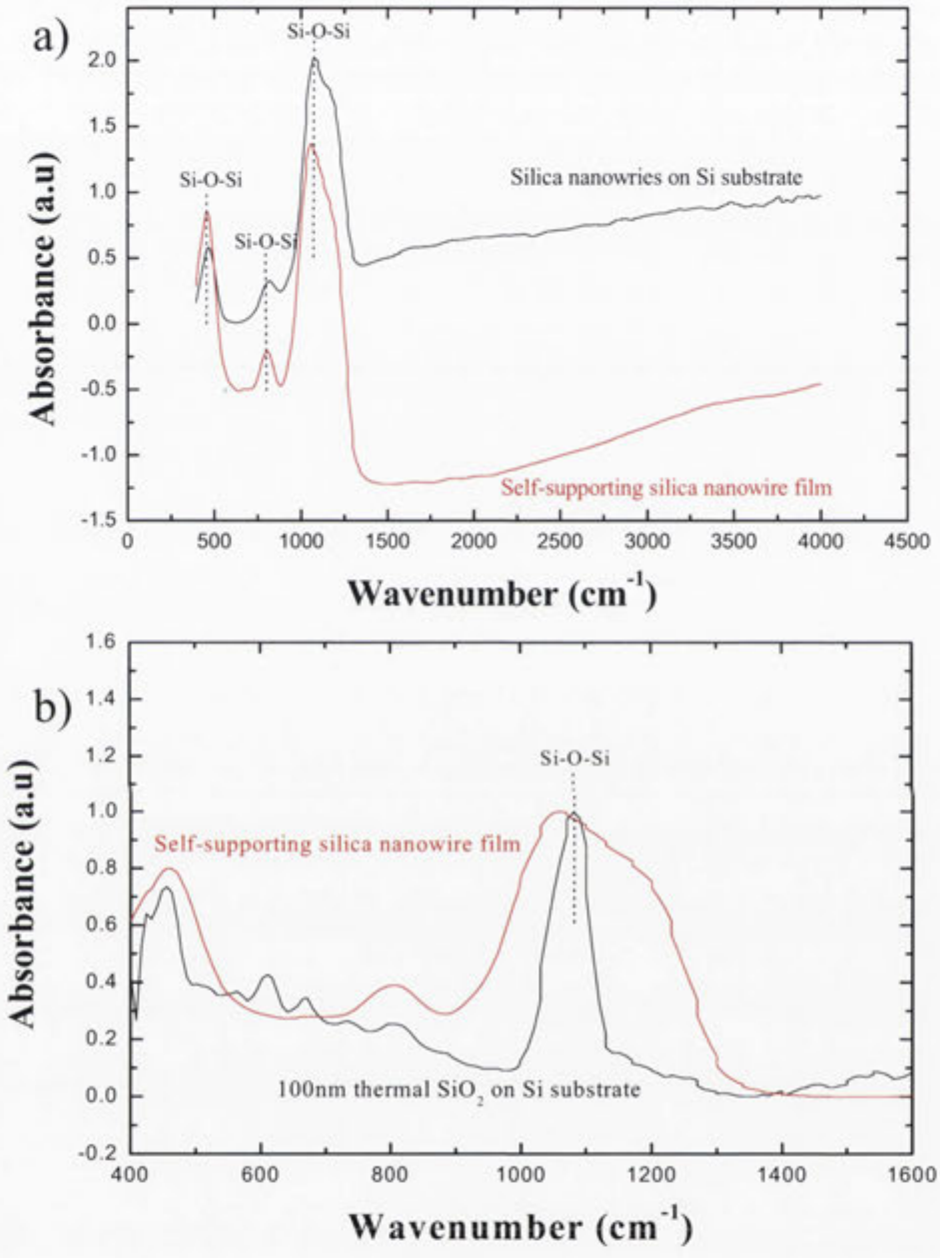

Figure 5.2: FTIR spectra for a) a nanowire film on a silicon substrate (black line) and a self-supported (red-line) nanowire film, and b) scaled FTIR spectra for a self-supported nanowire film (red-line) and a 100nm thermal SiO_2 on Si substrate (black-line).

Figure 5.2 shows FTIR spectra of a self-supporting nanowire film, an as-grown silica nanowire layer and 100nm thermal SiO_2 on a Si substrate for comparison of structural difference. The FTIR spectra are similar in both cases of nanowires and show three intense absorption peaks located at 470, 800, and 1100cm^{-1}. The peak at 470cm^{-1} is attributed to the asymmetric Si-O-Si bending vibration; that at 800cm^{-1} to the symmetric stretching vibration, and the peak at 1100cm^{-1} to the asymmetric stretching vibration[38, 39]. The FTIR spectrum of a thermal oxide is included for comparison and shows an absorption peak at 1100cm^{-1} that is much narrower than that measured for nanowire samples. The significant broadening of this Si-O-Si bending mode peak for the nanowire sample reflects the additional vibrational freedom of surface atoms and is a direct consequence of the large surface-to-volume ratio of these samples.

B: Photoluminescence

It has previously been reported that silica nanowires emit stable and high brightness blue light[34]. In order to test this, photoluminescence measurements were performed on our silica nanowire samples. Figure 5.3 shows typical PL spectra collected from as-grown silica nanowires on Si substrate, self-supporting nanowire film, and 100nm thermal SiO_2 on Si substrate under 325nm excitation. Nanowire samples show strong and broad PL emission in the UV-blue emission range which can be fitted with three emission bands peaked at 370, 405, and 478nm, respectively, as shown in figure 5.3 b). Similar emission peaks have previously been reported for high purity silica prepared under different conditions[40-46]. Emission at 3.3(~370nm), 3.1(~405nm), and 2.6eV(~478nm) is generally attributed to oxygen–deficient defect centers[40, 44, 46-49]. These emissions are relatively intense in the case of nanowire samples, consistent with their substoichiometric composition. i.e. The average composition is $SiO_{1.8}$ which implies a high concentration of oxygen-deficient centres. Importantly, these defects are in close proximity to the sample surface due to the small dimensions of the nanowires and as a consequence the luminescence is expected to be sensitive to the presence of surface adsorbates –an important consideration for potential optical sensing applications.

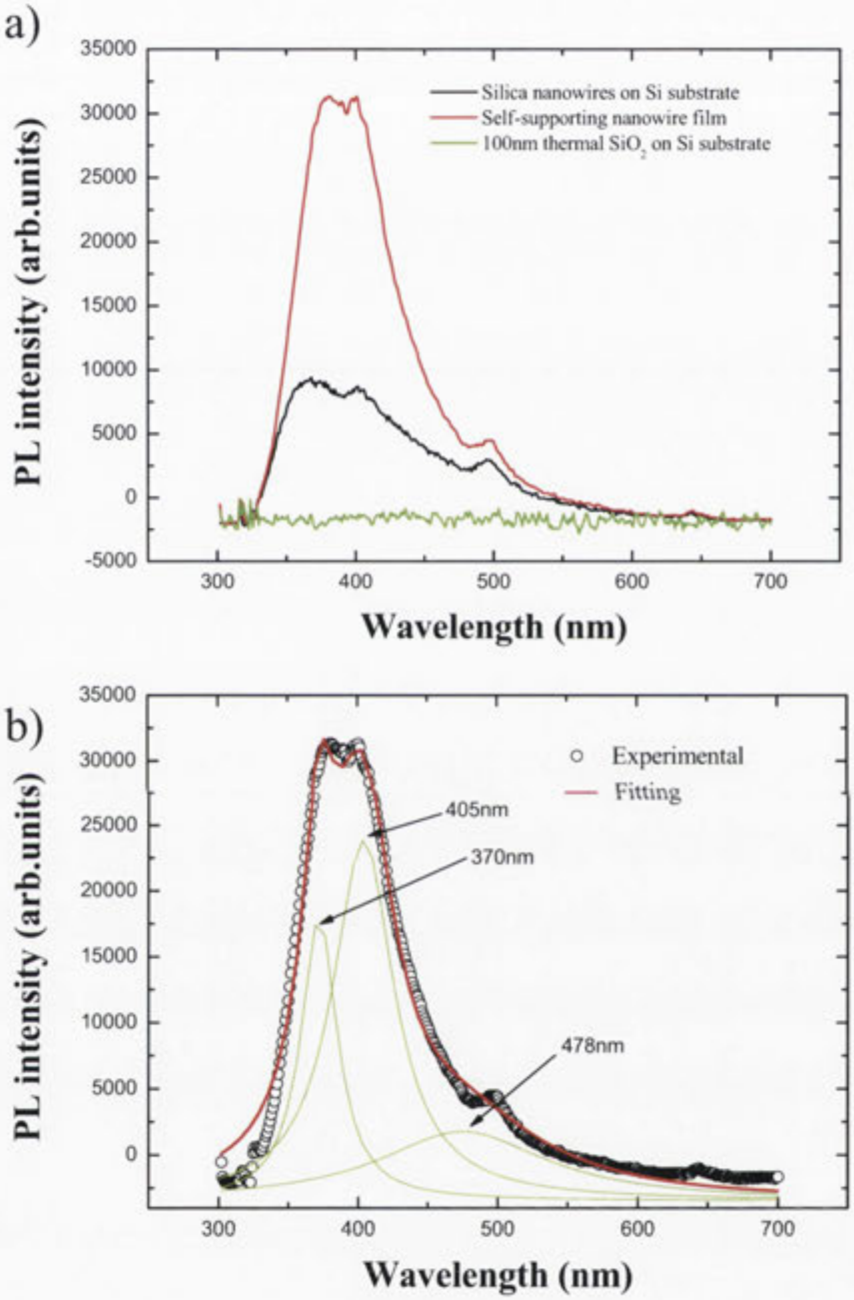

Figure 5.3: a) PL of the as-grown silica nanowires on Si substrate (black line), self-supporting nanowire film (red line), and 100nm thermal SiO_2 on silicon substrate and b) PL of the self-supporting nanowire film with fitting lines.

5.3.3 Extrinsic doping of nanowires

Doping is one method available to change the composition or functionality of nanowires. In general, nanowire doping can be achieved by in-situ doping (during the growth process) or by post-doping (after growth process) with various techniques such as implantation or sputtering/diffusion. As part of this study we have demonstrated both in-situ[33] and post[36]-doping of silica nanowires with the rare-earth element Er. In-situ doping was achieved by using Er as a constituent of the catalyst particles, either by implanting silicon substrates with Er or by depositing thin metal films of Er or Au:Er onto silicon prior to annealing at 1100°C. As discussed below, the implanted Er and deposited Au:Er films acted as effective catalysts for nanowire growth but the deposited Er film did not. Ex-situ doping was achieved by ion-implanting pre-formed nanowires with Er ions and annealing at 900°C to optically activate the Er. The work on ion-implanted samples has already been published elsewhere[36] and is not repeated here.

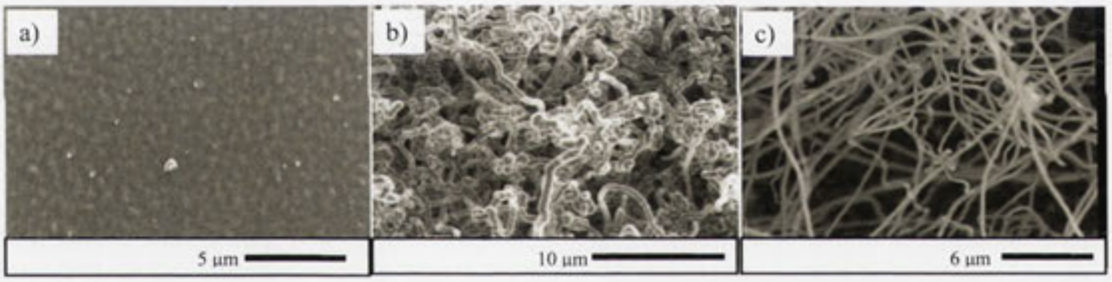

Figure 5.4: a) 10nm Er coated on Si substrate after annealing at 1100°C in N_2 for 4 hours, b) 30nm Au:Er (1:4 ratio) coated on Si substrate after annealing at 1100°C in N_2 for 1hour, and c) 6×10^{14} cm^{-2} ErO$^-$ ions implanted (30keV) on Si substrate (projected range of 20nm) after annealing at 1100°C in N_2 for 4 hours.

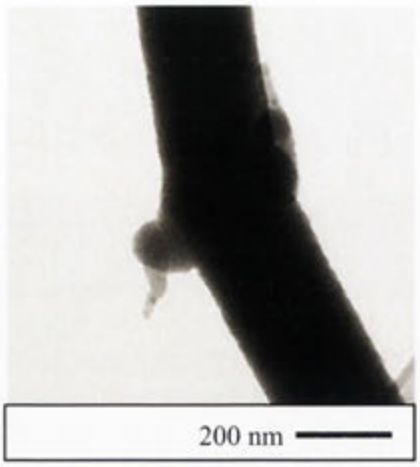

Figure 5.5: a) TEM image of nanowire grown by co-sputtered layer of Au and Er as a catalyst coated on Si substrate after annealing at 1100°C in N_2 for 1hour.

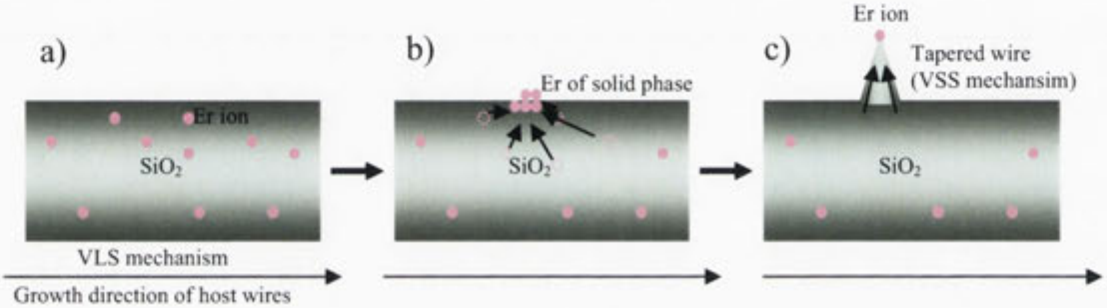

Figure 5.6: Schematic illustration for growth model of tapered nanowires explained by two-stage growth mechanism: a) primary nanowires absorbed Er atoms grown by Au:Er catalyst coated on Si substrate after annealing at 1100°C in N_2 (First-stage: VLS mechanism), b) During annealing process solid phase Er atoms are incorporated in host wires, and c) Finally, tapered nanowires (float growth mode) nucleated by Er atoms as catalyst on the surface of primary nanowires (Second-stage: VSS mechanism).

Figure 5.4 compares SEM images of three samples annealing at 1100°C in N_2: one coated with 10nm of Er metal; and one coated with 30 nm of Au and Er (1:4 ratio); and one ion-implanted with 30 keV ErO^- ions to a fluence of 6×10^{14} cm^{-2} (projected range of 20nm). No nanowires are observed on the sample coated with Er. In contrast, the sample coated with Au and Er has a dense array of silica nanowires and the ion-implanted sample has a low density of silica nanowires. The lack of nanowires on the Er coated sample is attributed to the fact that Er has a high melting temperature (1522°C) and forms a protective coating on silicon wafer rather than forming small islands. This prevents the formation of SiO_2 via the reaction between residual oxygen and the silicon substrate. The addition of Au aids the film breakup and enables nanowire growth. However, the morphology of the nanowires is quite different to those produced by Au only. In particular, the wires have a twisted and corrugated form. The mean diameter of the nanowires is around 700nm and their lengths exceed 10s of micrometers. Significantly, TEM images prepared from the same sample show small tapered wires emanating off host wire, as shown in figure 5.5. No such secondary growth is observed for Au-only catalysts. This suggests that the tapered nanowires are nucleated by Er particles. (A conclusion that is supported by the observation of profuse secondary growth of tapered wires in the case of Er-coated silica nanowires annealed at 1100°C as discussed further in section 5.3.5). The growth of these tapered nanowires can be explained by a two-stage growth mechanism, as shown in Figure 5.6. First, primary nanowires grow by the vapour-liquid-solid mechanism with Au as the primary catalyst. During this process, Er atoms are adsorbed on, or incorporated in the host nanowires. Second, the Er diffuses and clusters on the nanowire surface to form small precipitates that act as catalyst particles for the secondary growth nanowires (Vapour-Solid-Solid mechanism). Because Er (and related compounds) has a high melting point it is expected to remain in the solid-phase during nanowire growth. As a result the nanowire growth rate is expected to be much slower than that induced by the liquid Au catalyst. This is consistent with the growth of relatively short, tapered nanowires as the tapering is directly related to the ration of transverse and lateral growth.

Attempts to measure or image the Er at the tips of the nanowires was unsuccessful but we have observed small Er catalyst particles on the tip of Er-catalyzed nanowires (float growth) grown from Er-implanted Si substrates[33].

A: Photoluminescence

The presence of optically active Er can also be detected from photoluminescence measurements of the 1.5 μm Er^{3+} emission, corresponding to the $^4I_{15/2}$-$^4I_{13/2}$ transition. Figure 5.7 shows a photoluminescence spectrum from silica nanowires nucleated by Au:Er thin-film catalysts. The emission is characteristic of Er^{3+} in silica (a direct comparison is shown in Fig. 5.22 b))

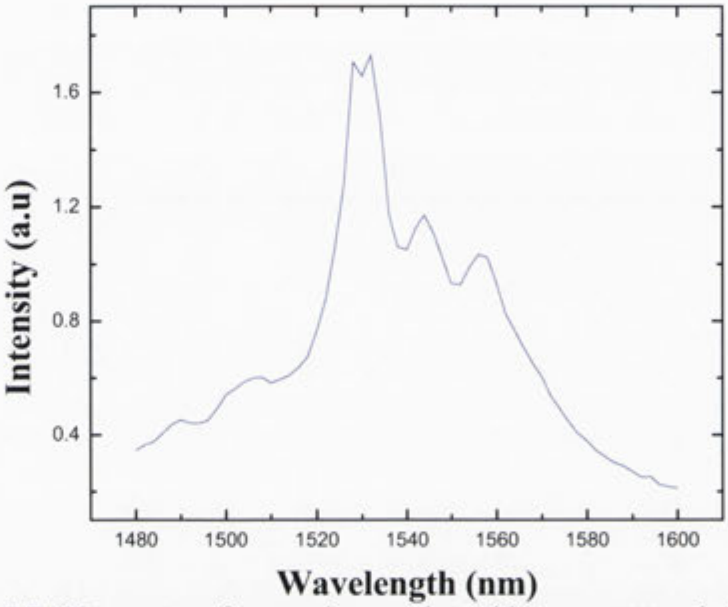

Figure 5.7: PL spectra of nanowires nucleated by co-sputtered Au and Er (1:4 ratios) as catalyst on Si substrate after annealing at 1100°C in N_2 for 1hour.

5.3.4 Au peapod structures

Under certain growth conditions, such as is observed in the presence of a capping layer or when thick catalyst films are employed, it is common to find nanowires with encapsulated metal particles in them, often in the form of regularly spaced particles of similar diameter. As an example, Figure 5.8 a) shows a SEM image of encapsulated Au particles observed following root growth of nanowires. In this case the wires were grown by coating a silicon wafer with 10 nm of Au and annealing at 1100°C in N_2 for 1 hour with Si capping layer (Corresponds to part B of the sample shown in Fig 4.32).

The nature of the particle is evident from EDX analysis (Figure 5.8 b)) and the bright contrast evident in the electron backscattering image (inset).

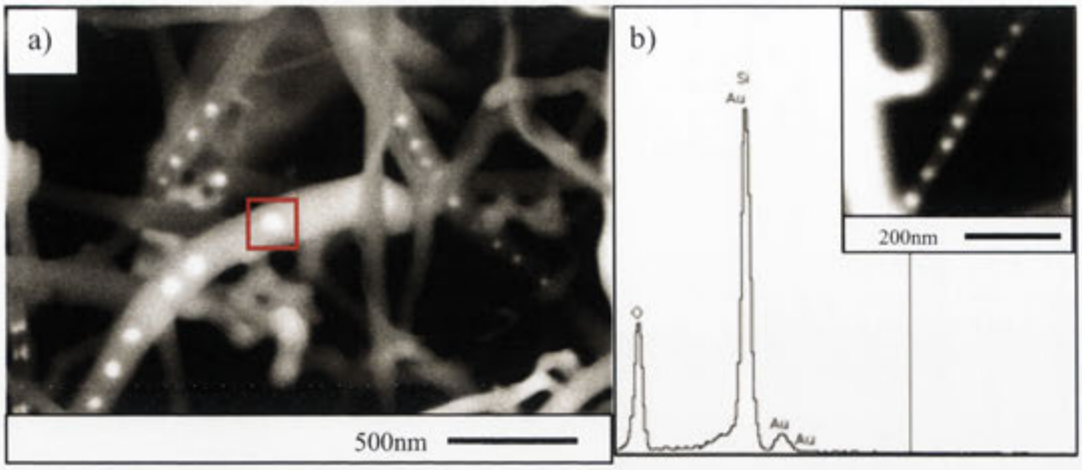

Figure 5.8: a) SEM image of typical Au peapod structures observed in root growth of nanowires (Corresponds to part B of the sample shown in Figure 4.32) grown by 10nm Au film on Si substrate after annealing at 1100°C in N_2 for 1 hour with silicon capping layer.

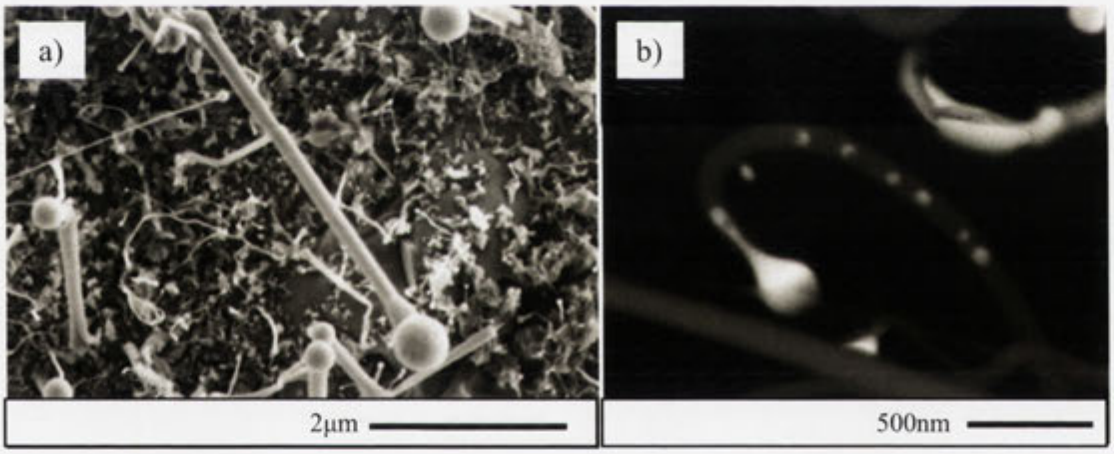

Figure 5.9: a) SEM image of float growth mode of nanowires grown by 10nm Au coated Si after annealing at 1100°C in N_2 for 1hour with Si capping layer, b) Backscattering electron image of Au peapod structure observed from nanowires of float growth after re-annealing at 1100°C in N_2 for 20 min without its capping layer (Corresponds to part A of the sample shown in Fig. 4.32).

Similar behaviour is observed during float growth, as shown in Figure 5.9. In this case the wires of float growth (in Figure 5.9 a)) were grown by coating a silicon wafer with

10 nm of Au and annealing at 1100°C in N_2 for 1 hour with Si capping layer (Corresponds to part A of the sample shown in Fig. 4.32) then re-annealing the sample under the same conditions (temperature and ambient but annealing time for 20min) as those employed for the initial growth but without its capping layer (in Figure 5.9 b)). The Au catalyst particle is clearly evident at the tip of the wire, as is its distinctive form.

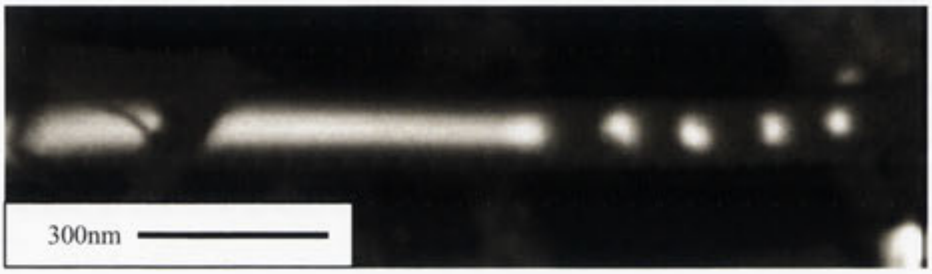

Figure 5.10: Au wire in silica nanowires grown by coating a silicon wafer with 10 nm of Au and annealing at 1100°C in N_2 for 1 hour with Si capping layer then re-annealing the sample under the same temperature and ambient but annealing time for 20min without its capping layer (The growth direction is towards the right and the wire is capped by Au head, which is not included in the image).

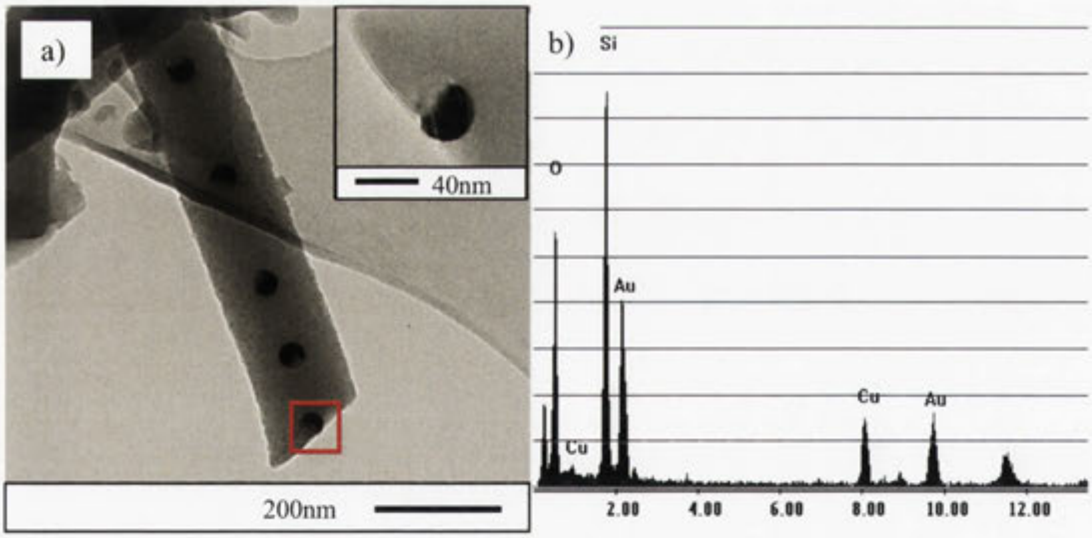

Figure 5.11: a) TEM image of Au peapod structures grown by coating a silicon wafer with 10 nm of Au and annealing at 1100°C in N_2 for 1 hour with Si capping layer then re-annealing the sample under the same temperature and ambient but annealing time for 20min without its capping layer (inset Au particles within the nanowire) and b) EDX spectrum of Au nanoparticle.

Previous studies have reported Au peapods in silica nanowires fabricated from the thin-film sandwich structures annealed in a microwave reactor[17]. The proposed mechanism in this case involved the formation of a gold wire in a hollow silica tube which subsequently transformed into droplet-like Au nanoparticles via Rayleigh instability. The hollow silica matrix was suggested to be non-stoichometric, with a silicon-rich stoichiometry. Silica nanowires containing central Au wires have also been observed in the present study, as shown in Figure 5.10, and there is evidence that Au nanoparticles can form from such wires. However, TEM images of other nanowires, such as that shown in Figure 5.11, show no evidence of a core-shell structure (i.e. they exhibit uniform contrast across the diameter of the nanowire in regions between Au nanoparticles)

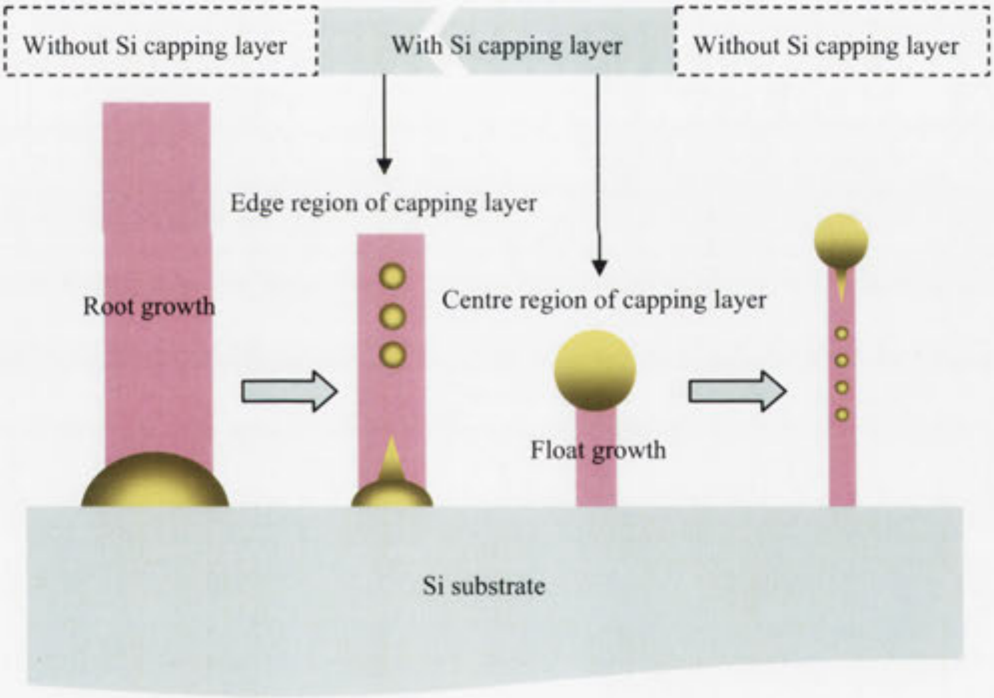

Figure 5.12: Schematic illustration of observed Au peapod structures. First, Au particles in the root growth mode are observed in edge region of sample. Second, Au particles in float growth mode are observed in centre region of sample after re-annealing of float growth nanowires under the same condition without Si capping layer.

Our experimental observations are summarized in Figure 5.12, which shows schematics of Au peapod formation during float and root growth and the affect of capping layers. As discussed in chapter 4, the nanowire growth mode can be changed from float growth to root growth by using a Si capping layer as a secondary source of SiO vapour. The growth mode was also shown to be sensitive to the distance between the capping layer and silicon/silica substrate due to its affect on the concentration of O_2 available for reaction with Si (i.e. SiO concentration). The production of pea-pod structures is sensitive to these influences suggesting that it is controlled by reaction kinetics as well as the mode of growth.

According to an earlier report, insufficient oxygen supply[50] and chemical reduction[51] induced by the formation of Au-Si eutectic can give rise to structurally imperfect silica and further facilitate silicon migration. In addition, it has recently been reported that Au located on the head of silicon nanowires (float growth mode) can migrate down the centre of the wire during subsequent oxidation of the nanowires[52, 53]. Similar behaviour could be expected during the growth of silicon-rich silica nanowires, or silica nanowires with silicon-rich cores, and may explain why the growth of pea-pod structures is so sensitive to the local vapour concentration. In this case peapods would form from the Au-rich core by a Rayleigh instability[54, 55]. However, as shown above, many of our observations are inconsistent with this as a general model. Specifically, the size and spacing of "peas" varies from that expected from wire decomposition, and the spatial distribution of the peas often has limited extent. To address these inconsistencies an alternative model of pea-pod formation was developed.

The proposed model is based on combination of two main driving forces. The first driving force is the change in composition of reactants (SiO and oxygen) that affected the kinetic energy of Au droplet. In the float growth mode, when nanowires are nucleated by Si capping layer, kinetics of supersaturated Au droplets sustain nanowire growth because of their equilibrium concentration (Au-Si-O), as shown in Figure 5.13 (a). However, after removing Si capping layer, the Au droplets absorb more O_2 and become unstable [Au(-)-Si(↓)-O(↑)] (Figure 5.13 (b)). In order to return to the equilibrium state, the oxygen-rich Au droplets expel excess Au and O_2, as shown in Figure 5.13 (c) (Si content in oxygen-rich Au droplet is minimum proportion of elements for renewed equilibrium).

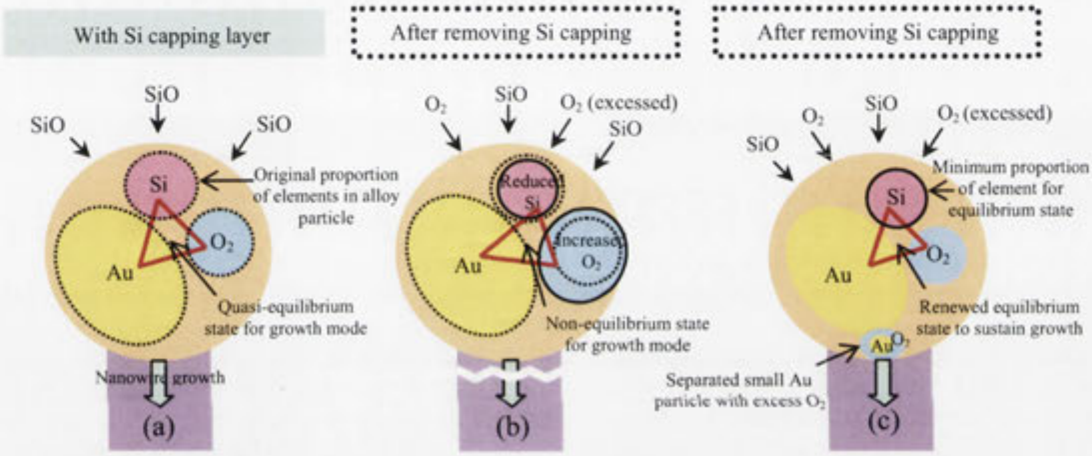

Figure 5.13: Schematic diagram of the proposed kinetics in Au droplet for pea-pod growth model: (a) Equilibrium state (Au-Si-O) for nanowire growth in original growth condition; (b) Non-equilibrium state by changing in composition of the reactant due to excess O_2 after removing Si capping layer and (c) Renewed equilibrium state after separating small Au particles and excess O_2 to sustain growth to maintain growth mode.

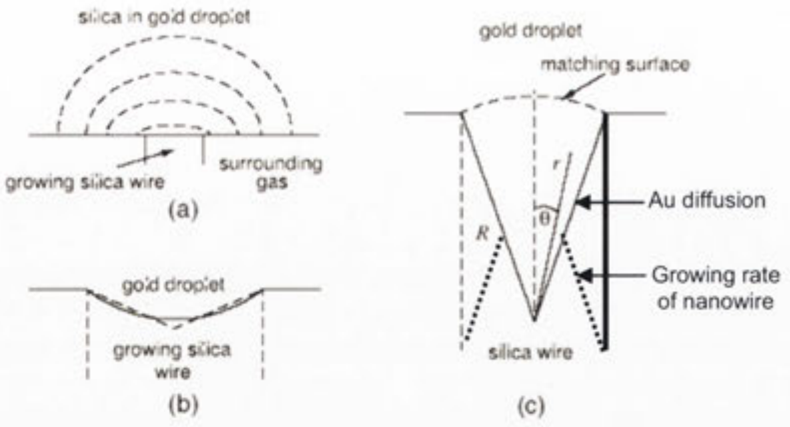

Figure 5.14: (a) Simple initial approximation of a growing disc, representing the interface between the silica wire and the gold droplet, on an inert flat plane. Broken curves are contours of equal concentration. (b) Diffusive growth leads to a central depression in the nanowire that can be approximated as conical. (c) Coordinates for analysis of conical growth. The solution inside the cone must be matched to the solution in the droplet on the matching surface.

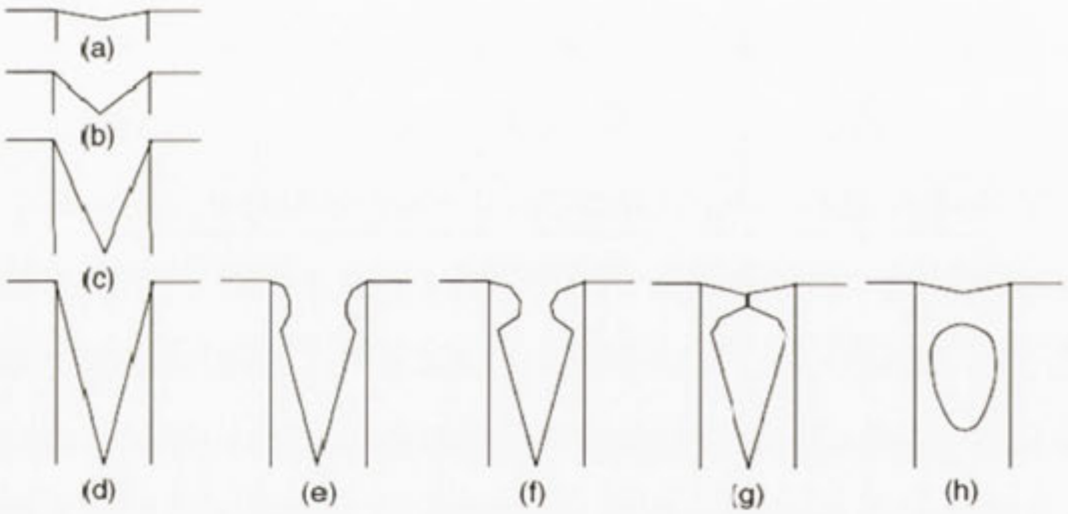

Figure 5.15: Evolution sequence of the catalyst/nanowire interface predicted by diffusive model[56].

The second driving force is diffusive transport of reactants within the Au catalyst particle and the realization that the maximum growth rate of silica occurs at the periphery of the catalyst particle where the concentration gradient of reactants is greatest. The initial evolution of the system is shown in Figure 5.14. The Au droplet adsorbs SiO vapour and oxygen from the surrounding atmosphere and this diffuses to the growing silica nanowire (Figure 5.14 a)). Because the concentration gradient is larger near the edge of this circular interface than at the centre, the edges grow more rapidly and the interface develops an almost conical depression in the growing nanowire (Figure 5.14 b-c)). This establishes the conditions for a periodic evolution of the structure as shown in Figure 5.15. As the aspect ratio of the cone increases beyond a critical value its top begins to close under the influence of diffusion and ultimately seals off, leaving a small volume of liquid gold within the wire. The enclosed liquid gold then gradually evolves to a spherical droplet under the influence of its interfacial free energy. This process then repeats in a regular manner if the gas environment remains stable, giving a chain of gold droplets with a short length of solid silica separating them from each other. This diffusion model and an analytical approximation to its solution and explained in more detail in the original reference[56]. Suffice it to say that the model predicts the formation of periodic pea-pod structures without the requirement to first form a metal wire. It also predicts a dependence on reaction kinetics, as the concentration gradients responsible for the differential growth rate at the catalyst-nanowire-interface depend on this kinetics.

5.3.5 Metal decorated nanowires

As discussed in the introduction to this chapter, metal decorated nanostructures are of great interest as high-surface area catalysts and optically-based sensors. The latter is usually based on surface enhanced Raman scattering or plasmon resonant absorption from the metal, but can also be extended to include Plasmon-enhanced luminescence from optically active nanowires. Silica is an ideal substrate for such applications due to its optical transparency, chemical inertness, and biocompatibility. Various approaches to the fabrication of such metal-decorated nanostructures were explored as part of this project.

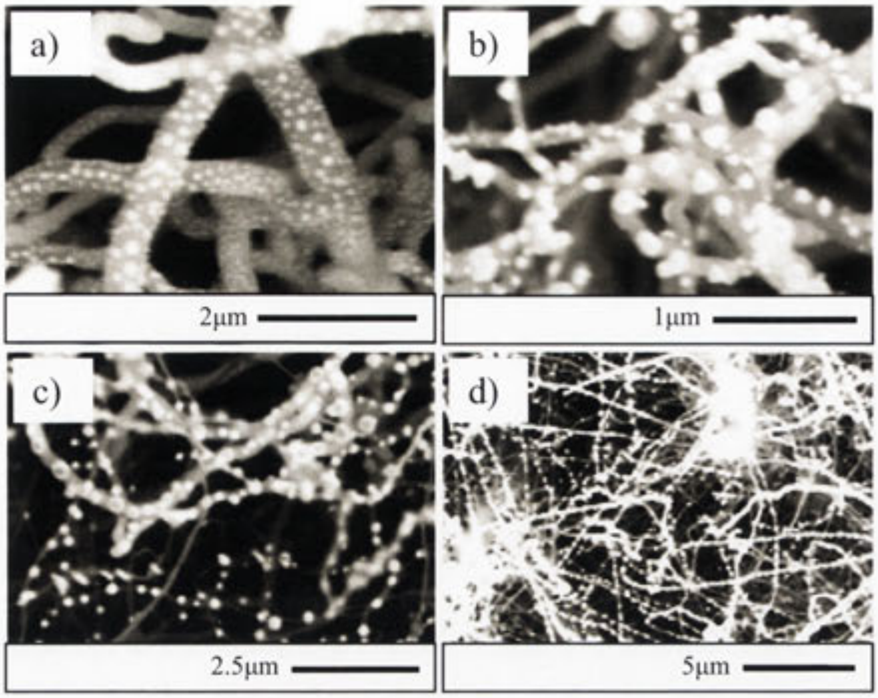

Figure 5.16: SEM images of Au decorated silica nanowires fabricated by 10nm Au deposited on as-grown silica nanowires after re-annealing a) 900, b) 1000, and c) 1100°C in oxygen for 1hour. On the other hand, d) SEM images of Au decorated self-supporting film fabricated by 10nm Au deposited on as-grown self-supporting film and re-annealing at 1100°C in oxygen for 1hour.

Figure 5.16 shows a hybrid metal-silica nanostructure consisting of Au nanoparticles on silica nanowires. This structure was synthesized by depositing 10nm Au film on as-grown silica nanowires and then re-annealing in oxygen ambient at different temperatures. Figure 5.16 a), b), and c) show Au necklaces annealed at 900, 1000 and 1100°C, respectively. The same hybrid nanostructure was also synthesized with self-supporting silica nanowire films (described in Section 5.3.1), as shown in figure 5.16 d). Au has a melting point of 1063°C and is expected to remain in the solid phase during annealing at 900 and 1000°C (NB: There is evidence to suggest that nanoscale particles melt at temperatures lower than their bulk counterpart and this cannot be ruled out. However, Au is observed to ball up into nanoparticles on silica at temperatures as low as 500-600°C where it clearly remains in the solid phase). The resulting nanoparticles have a broad size distribution but the average particle size clearly increases with increasing temperature. (This is not obvious from the SEM micrographs in Fig. 5.16 for the sample annealed at 1100°C and the self-supporting film because they represent nanowires of different diameters but it is confirmed by optical absorption data which samples representative areas of nanowires –see below) The Au nanoparticles remain on the nanowire surface but no secondary growth of nanowires is observed in this case, even at temperature as high as 1100°C, because the O_2 ambient precludes the formation of SiO vapour.

A: Optical absorbance

Figure 5.17 shows the optical absorption spectra of Au decorated nanostructures. As expected, no Plasmon-band is observed from as-grown silica nanowires (A) or as-grown self supporting nanowire films (D). In contrast, the decorated films show a well defined Plasmon absorption band in the 500-550nm wavelength range. As shown in figure 5.17 b), Au decorated nanowires synthesized by annealing at 1100°C with Au deposited on as-grown self-supporting film (E) show stronger and narrowing optical absorption band near 540nm. According to earlier studies, the absorption band of surface plasmon resonance of Au nanoparticles is close to 520nm and its peak position and width are affected by the size and shape of Au particles[10, 57-60]. For spherical nanoparticles the maximum shift in the plasmon resonance is from approximately in the range of 520 – 570nm, with the longer wavelength corresponding to the smallest particles. Analysis of the spectra in Figure 5.17 a) shows that the absorption peak shifts to longer wavelengths for the sample annealed at 1100°C when compared to that annealed at 1000°C, consistent with the trend discussed above.

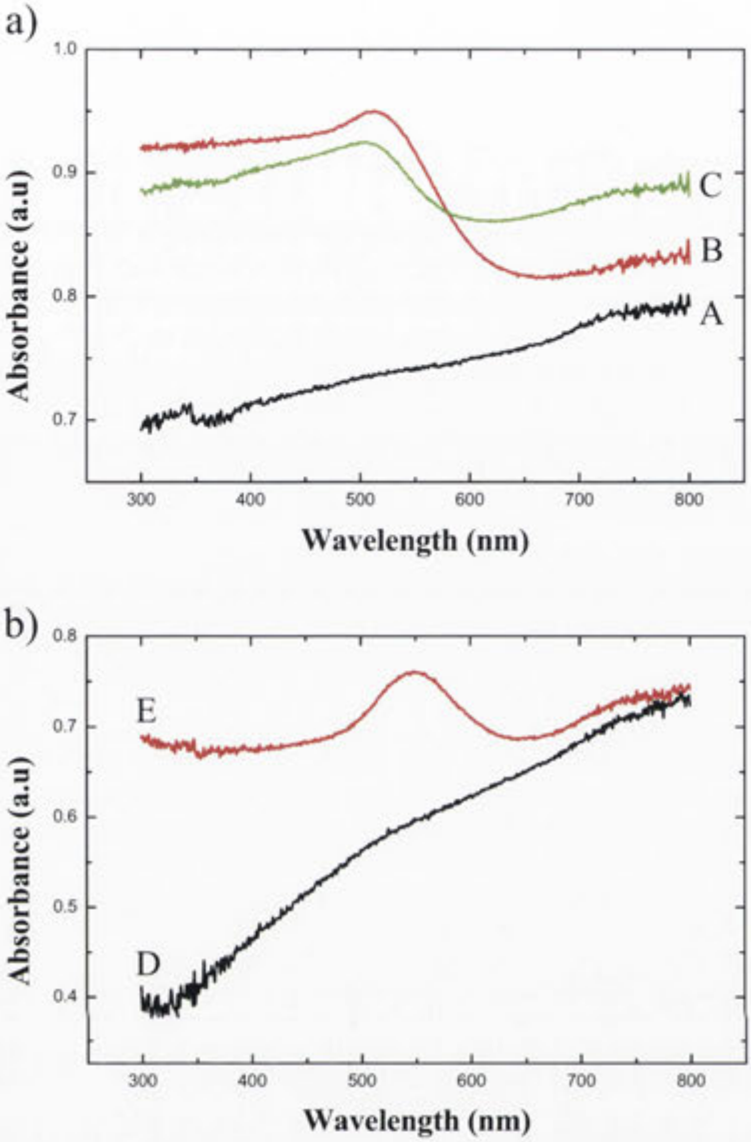

Figure 5.17: a) absorption spectra of as-grown silica nanowires on a silicon substrate without Au (A), Au decorated nanowires fabricated at 1000°C (B), and Au decorated nanowires fabricated at 1100°C (C). b) absorption spectra of as-grown self-supporting silica nanowire film (D) and Au decorated nanowires fabricated at 1100°C with self-supporting silica nanowire film (E).

5.3.6 Core-Shell nanowire structures

As an extension of the work on decorated nanostructures, nanowire samples were also coated with Er metal of 30nm thickness and annealed at 1100°C in O_2 for 1 hour to form a luminescent coating of Er_2O_3. Figure 5.18 a) shows a SEM image of nanowires after the coating process. As-grown silica nanowires were coated with Er metal using a sputter deposition system and subsequently annealed at 1100°C in oxygen ambient for 1 hour. No difference in the physical shape of the nanowires was observed after the deposition process. Figure 5.18 b) shows a TEM image of an individual nanowire after the coating process (inset edge of coated nanowire). Figure 5.18 c) shows a cross-sectional TEM image of a coated nanowire clearly highlighting the silica nanowire core and the Er-based coating. EDX measurement of the dark shell region confirms the presence of Er, as shown in Figure 5.18 d).

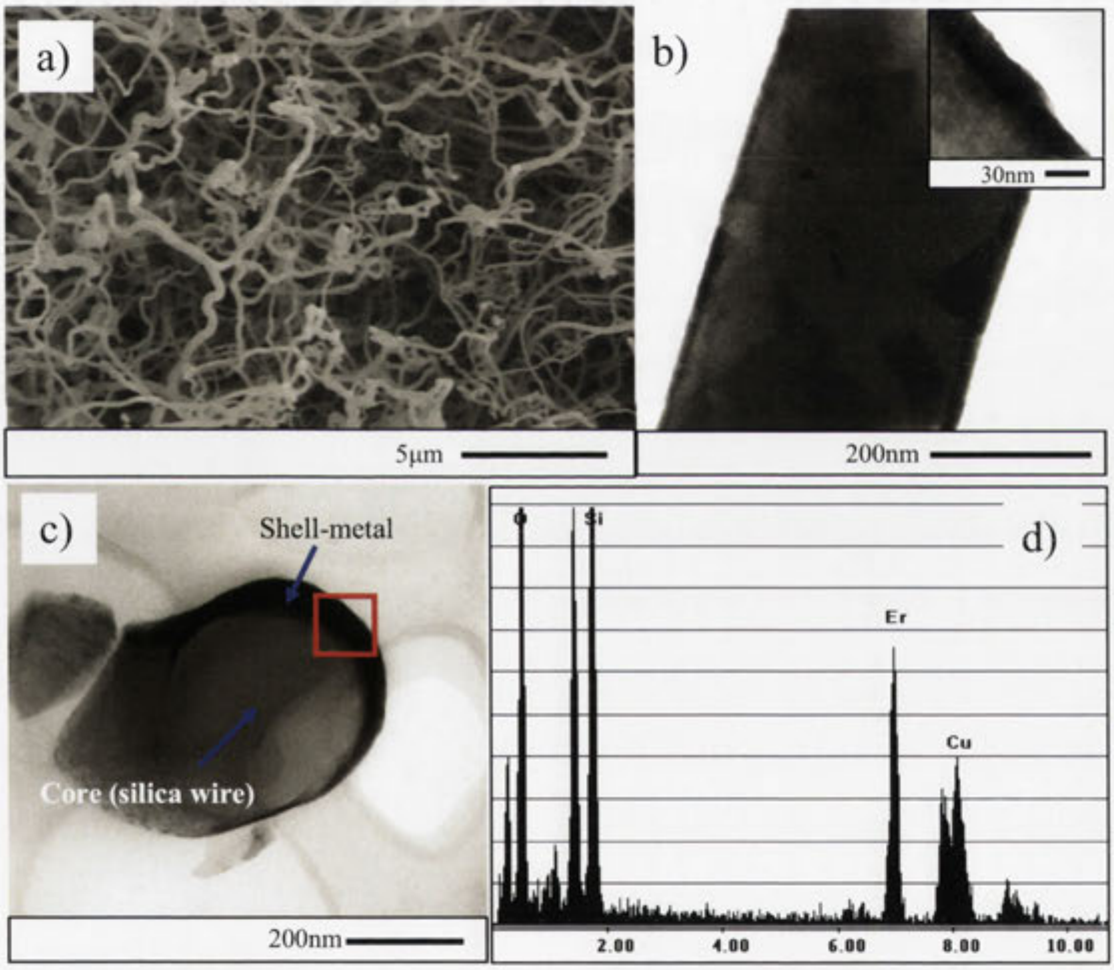

Figure 5.18: a) SEM image of nanowires annealed in O_2 ambient after the coating process, b) TEM image of individual nanowire (inset edge of coated nanowire), c) Cross-sectional TEM image of coated nanowires (core-shell structure), and d) EDX spectrum of dark part of nanowire.

For comparison, Er-coated nanowires of 30nm thickness were also annealed at 1100°C (1 hour) in N_2. i.e. under conditions in which SiO vapour is produced by reaction between residual oxygen and residual O_2. Figure 5.19 a) shows a SEM image of the resulting nanostructures. In this case a low density of small tapered nanowires (secondary growth) is observed on the primary nanowires. (As discussed earlier, deposited Er films show limited catalytic activity due to the lack of islanding.) However, TEM analysis of the primary nanowires, Figure 5.18 b), reveals a more complex coaxial nanostructure. Specifically it shows a triple-layer coaxial structure consisting of a silica-core, an Er-based coaxial layer, and an outer silica-based cladding layer, as shown in Figure 5.19 c). This structure can be explained by lateral growth, as discussed in chapter 4. i.e The surface of the Er coated nanowires was coated by a silica-based layer formed by the adsorption of SiO vapour produced from the substrate. Figure 5.20 shows a schematic diagram of the resulting multi core-shell structures fabricated by metal coating (A→B) and re-annealing process (B→C). In the previous study, Meng et al have previously reported core-shell nanostructure synthesized by thermal evaporation of SiO[61].

Analysis of the small tapered nanowires shown in Figure 5.19 is included in Figure 5.21 which shows TEM images and EDX spectra of these features. The growth of these tapered nanowires is clearly based on a float growth mechanism as metal catalyst particles are clearly visible on the tips of the structures. As discussed earlier, the growth of such tapered nanowires can be explained by Vapour-Solid-Solid (VSS) mechanism in which the taper is produced by the relative rates of transverse and lateral growth.

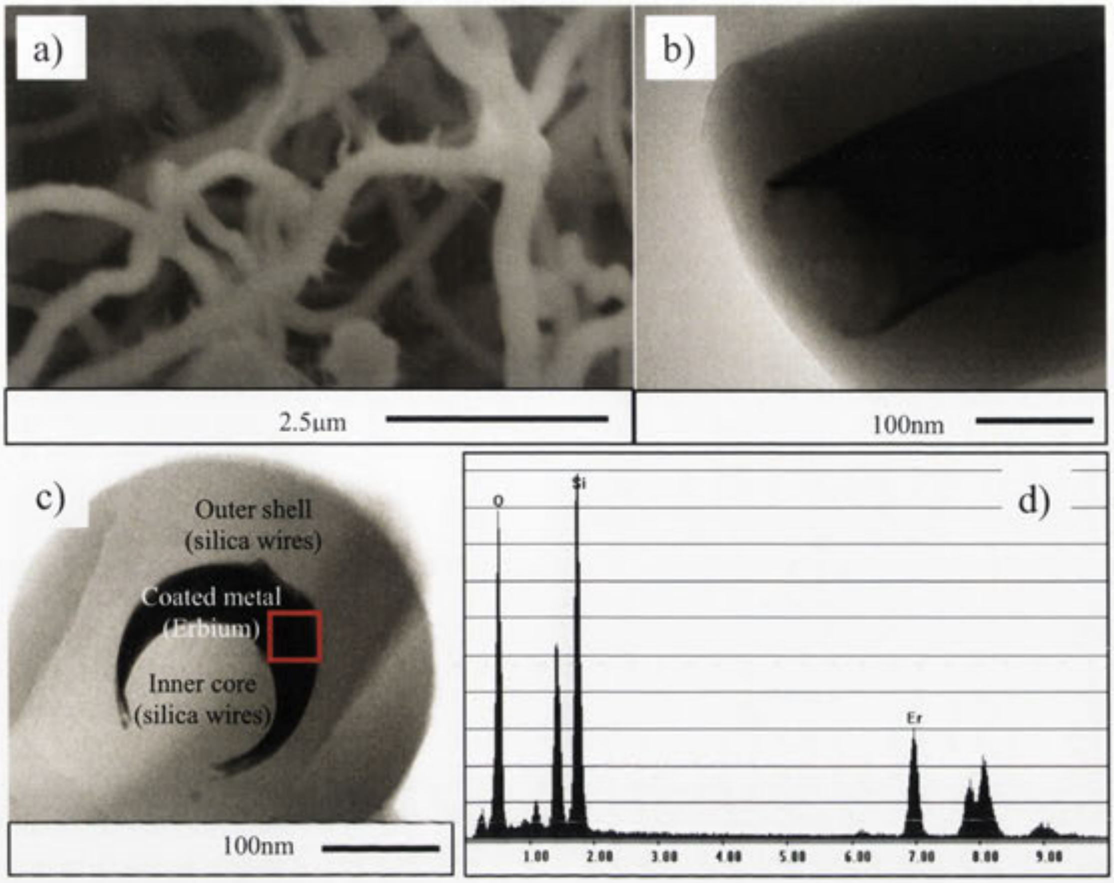

Figure 5.19: a) SEM image of nanowires annealed in N_2 ambient after the doping process, b) TEM image of individual nanowire, c) Cross-sectional TEM image of the doped nanowires (multi core-shell structure), and an d) EDX spectrum of the darker region of the nanowire image showing the presence of Er.

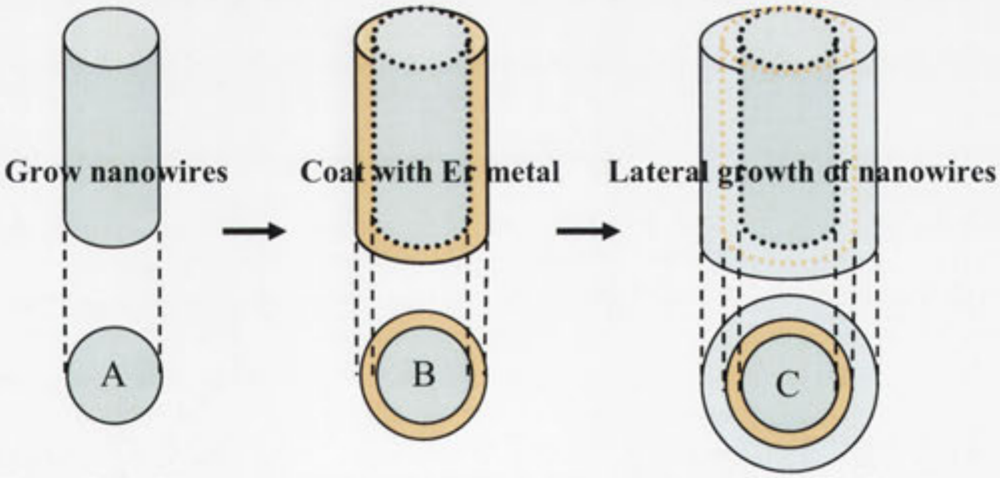

Figure 5.20: The schematic diagram of the core-shell structure (A→B→C).

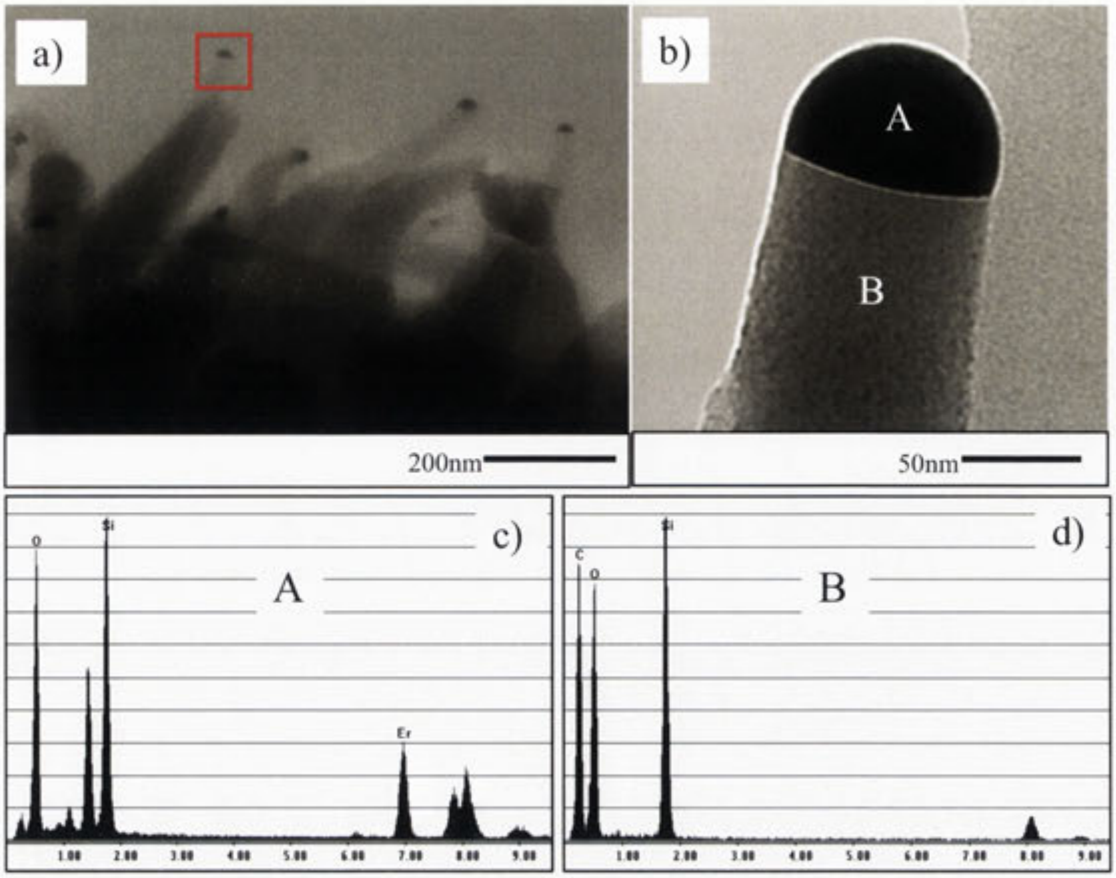

Figure 5.21: a) TEM image of tapered nanowires grown on Er coated silica nanowires after re-annealing process, b) TEM image of float growth mode of tapered wire, c) EDX spectrum of the head of tapered wire (A), and d) EDX spectrum of the stem of tapered wire (B).

A: Photoluminescence

Figure 5.22 a) shows PL spectra in the infrared (IR) range from as-grown silica nanowires, Er coated core- shell silica nanowires, and Si substrate after removal of the Er coated core-shell silica nanowires, respectively. No emission is observed in this wavelength range from as-grown silica nanowires or from the Si substrate after removing the Er-doped nanowires. This suggests that the measured PL emission is from the Er coated core-shell silica nanowires. For comparison, PL spectra were measured from silica slides co-doped with Er and Si nanocrystals (Er:SiNC) and Er_2O_3 powder, as shown in figure 5.22 b). The emission at around 1.53μm measured from Er:SiNC is characteristic of the $^4I_{15/2}$ -$^4I_{13/2}$ transition from the Er^{3+} ion in silica. Comparison of these various spectra shows that the emission from Er_2O_3 has significantly more structure than that from the Er^{3+} ion in silica. That additional structure is also evident in the Er-doped nanowire samples therefore suggests that at least part of this emission is from oxidized Er..

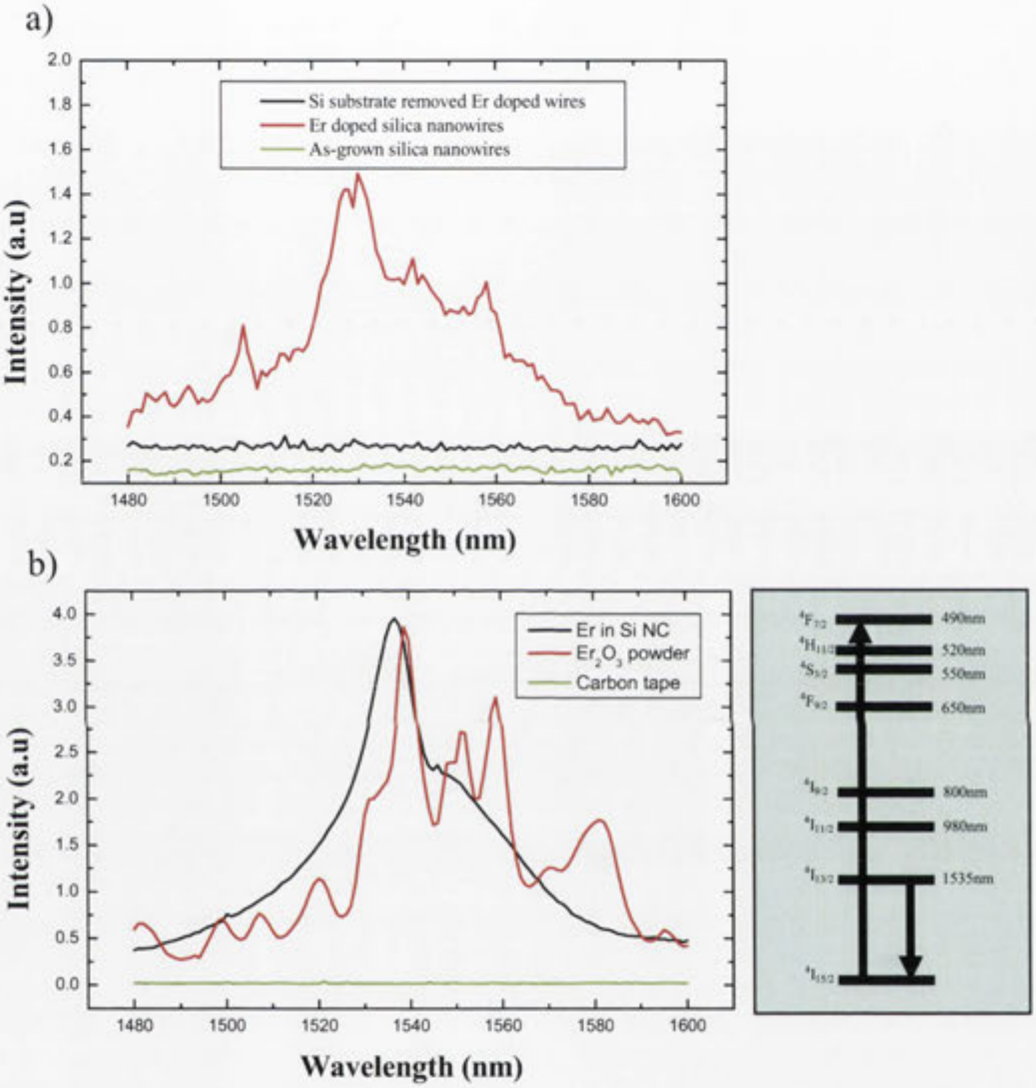

Figure 5.22: a) PL spectra of as- grown silica nanowires (green line), Er doped core – shell silica nanowires (red line), and Si substrate removed Er doped nanowires (black line). b) PL spectra of Er implanted Si nanocrystal synthesized in SiO_2 (black line), ErO_2 powder on carbon tape (red line), and only carbon tape (green line).

5.3.7 Combined (peapods + core-shell + self-supporting film) hybrid nanostructures

Having identified different approaches to the synthesis of novel nanostructures, attention is now directed to the synthesis on hyper-hybrid nanostructures that employ two or more of the above approaches. As an example, Figure 5.23 shows a complex nanostructure consisting of a silica inner core, an Er-based coaxial layer, an Au nanoparticle layer and a silica outer cladding layer. In order to fabricate this structure, nanowires were first grown on a silicon substrate by depositing a 10nm Au layer on silicon and annealing in N_2 at 1100°C for 1 hour. A 30nm layer of Er was then sputter deposited onto the nanowires and annealed in O_2 at 1100°C for 1 hour. This sample was then recoated with 10 nm of Au and annealed at 1100°C in N_2 to produce the silica cladding layer via lateral growth. The resulting film delaminated from the substrate to form a self-supporting thin film of silica-based nanowires with a structure as illustrated schematically in Figure 5.24. Figure 5.23 a) shows a SEM image of the resulting nanowires. A low density of secondary nanowires was observed on the primary nanowires, as discussed in the previous section. More detail of the nanowire structure is evident from the backscattered electron image of figure 5.23 b), which shows bright contrast from heavier elements and clearly delineates the Er-rich coaxial layer and the Au nanoparticles in the structure. This is even more evident in Figure 5.23 c) which shows an individual nanowire with the hyper-hybrid structures at high magnification. In this image, the inner Er-based coaxial layer is clearly evident. The brighter Au nanoparticles are encapsulated in an outer silica matrix produced by the final re-annealing in N_2. EDX spectra confirm the presence of Er and Au.

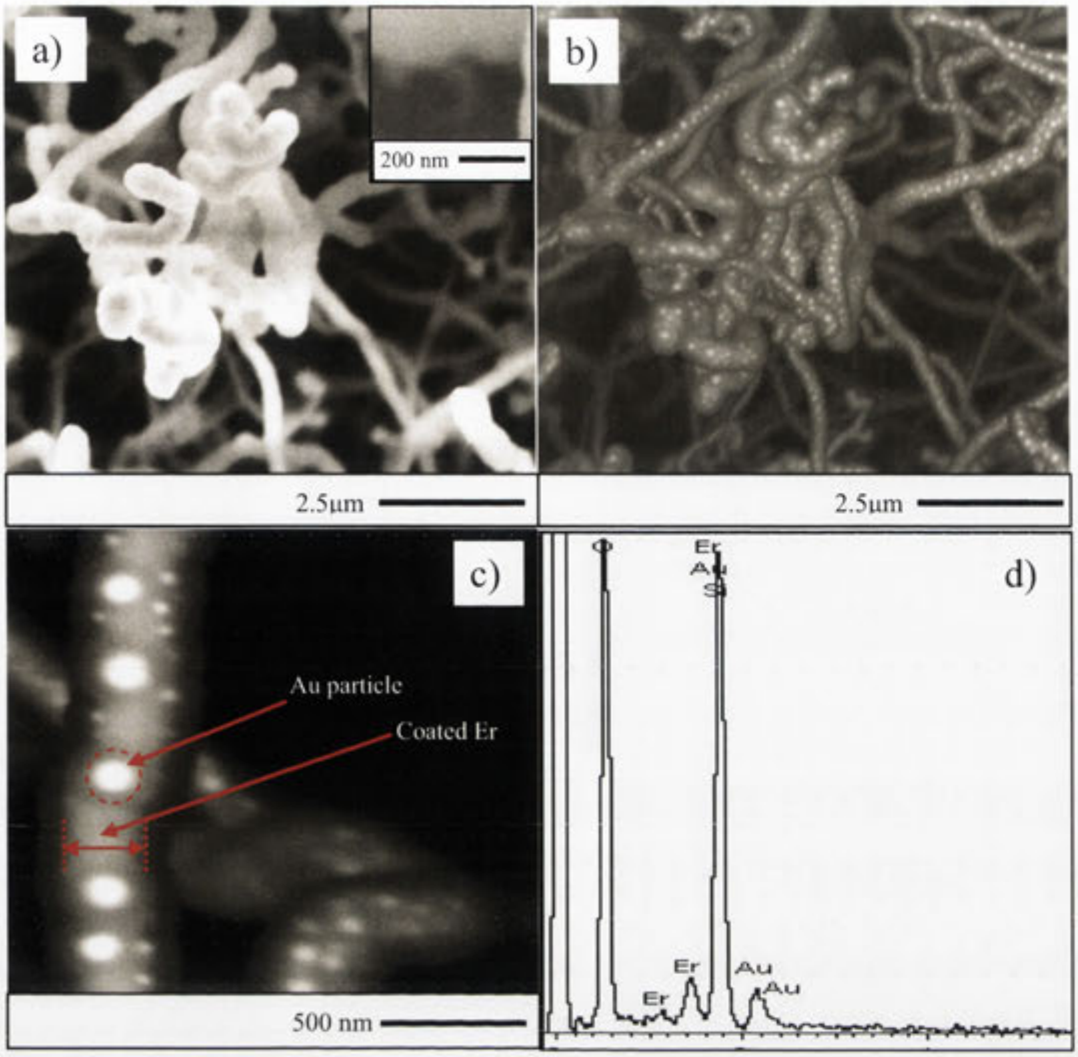

Figure 5.23: a) SEM image of hyper-hybrid nanowires and tapered nanowires (inset), b) backscattering image of hyper-hybrid nanowires, c) backscattering image of individual hyper-hybrid nanowire at high magnification, d) EDX spectra of hyper-hybrid nanowire.

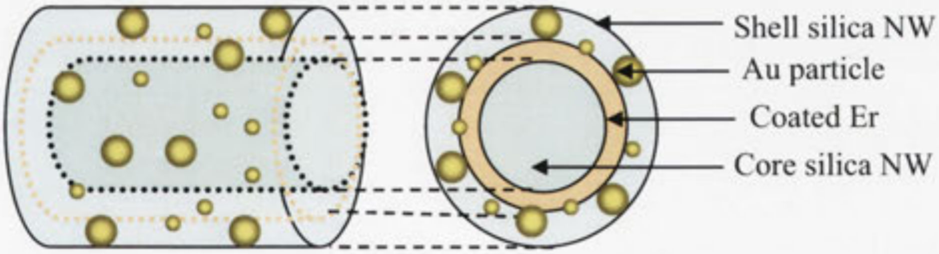

Figure 5.24: Schematic diagram of hyper-hybrid structure.

A: Optical absorbance

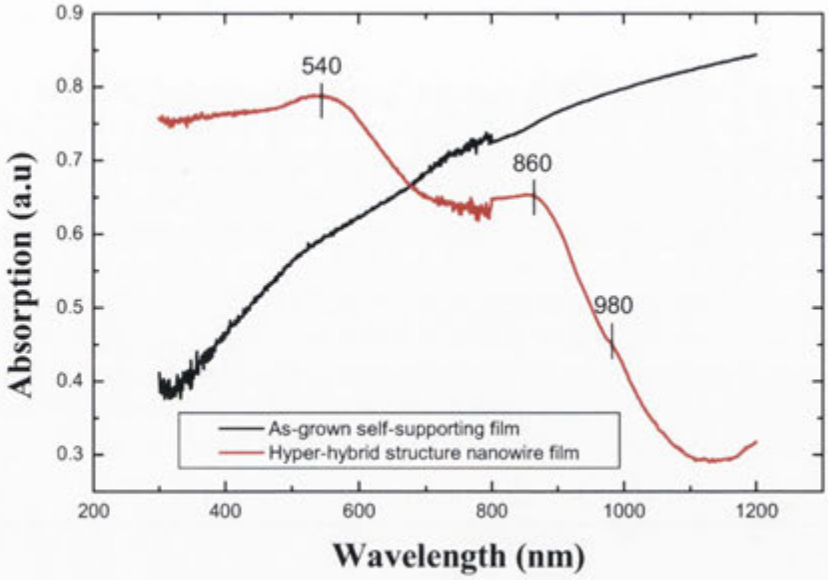

Figure 5.25: UV-visible spectrum measured from hyper-hybrid structures of silica nanowires (red line) and as-grown self-supporting film for comparison (black line).

The UV-visible absorption spectrum of the above sample is shown in figure 5.25. For comparison, an as-grown self-supporting silica nanowire film was also measured. The absorption spectrum from the sample shows three distinct absorption bands centered at 540, 860, and 980nm. As discussed in the previous section, the band at 540nm is attributed to the surface plasmon resonance of Au nanoparticles. The origin of the band at 860nm is less clear but absorption in this range has previously, been attributed to plasmon resonant absorption (longitudinal mode) from aggregates of small Au nanoparticles or to elongated Au nanoparticles[62-64]. This is consistent with the relatively strong absorption at 540nm which suggests a high density of Au nanoparticles but this conclusion remains speculative[65]. The smaller absorption band at 980nm corresponds to the $^4I_{11/2}$-$^4I_{15/2}$ transition in Er and is therefore attributed to this transition[66].

B: Photoluminescence

Figure 5.26 show a PL spectrum in the infrared range from hyper-hybrid structured silica nanowires. Only very weak Er-related emission is observed in this case.

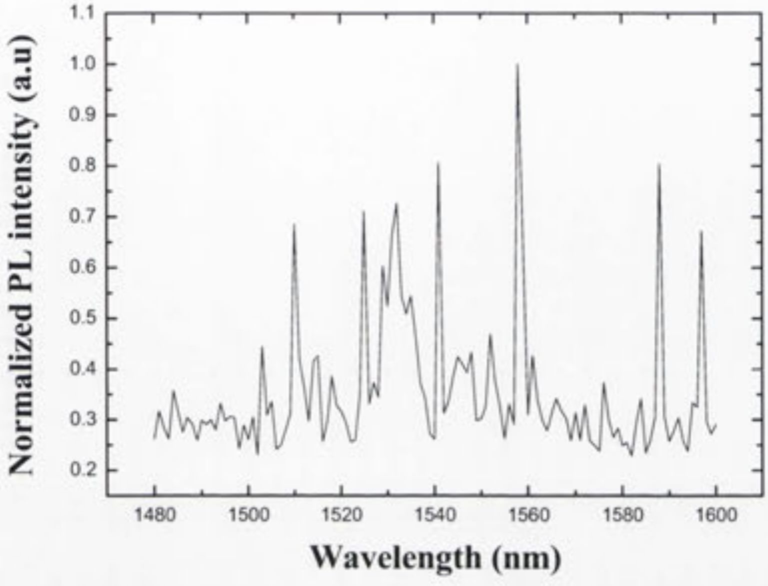

Figure 5.26: PL spectrum of hyper-hybrid structured silica nanowires.

5.4 Summary

In summary, a range of different approaches have been explored for the fabrication of hybrid metal-silica nanostructures. These structures include self-supporting nanowire films, Au peapod structures, Au decorated nanowires, Er core-shell nanowires and hyper-hybrid Au/Er/silica nanowires. Growth mechanisms were presented for these structures and basic optical properties were discussed.

5.5 References

[1] S. A. Maier, M. L. Brongersma, P. G. Kik, S. Meltzer, A. A. G. Requicha, H. A. Atwater, *Advanced Materials* **2001**, *13*, 1501.

[2] S. I. Bozhevolnyi, V. S. Volkov, E. Devaux, J. Y. Laluet, T. W. Ebbesen, *Nature* **2006**, *440*, 508.

[3] E. Ozbay, *Science* **2006**, *311*, 189.

[4] F. Patolsky, G. Zheng, C. M. Lieber, *Nanomedicine* **2006**, *1*, 51.

[5] D. J. Sirbuly, M. Law, P. Pauzauskie, H. Q. Yan, A. V. Maslov, K. Knutsen, C. Z. Ning, R. J. Saykally, P. D. Yang, *Proceedings of the National Academy of Sciences of the United States of America* **2005**, *102*, 7800.

[6] H. B. Liao, R. F. Xiao, J. S. Fu, P. Yu, G. K. L. Wong, P. Sheng, *Applied Physics Letters* **1997**, *70*, 1.

[7] A. Kiesow, J. E. Morris, C. Radehaus, A. Heilmann, *Journal of Applied Physics* **2003**, *94*, 6988.

[8] F. Hache, D. Ricard, C. Flytzanis, *Journal of the Optical Society of America B-Optical Physics* **1986**, *3*, 1647.

[9] R. F. Haglund, L. Yang, R. H. Magruder, J. E. Wittig, K. Becker, R. A. Zuhr, *Optics Letters* **1993**, *18*, 373.

[10] D. Dalacu, L. Martinu, *Applied Physics Letters* **2000**, *77*, 4283.

[11] V. Pardo-Yissar, R. Gabai, A. N. Shipway, T. Bourenko, I. Willner, *Advanced Materials* **2001**, *13*, 1320.

[12] S. Dhara, R. Kesavamoorthy, P. Magudapathy, M. Premila, B. K. Panigrahi, K. G. M. Nair, C. T. Wu, K. H. Chen, L. C. Chen, *Chemical Physics Letters* **2003**, *370*, 254.

[13] M. Quinten, A. Leitner, J. R. Krenn, F. R. Aussenegg, *Optics Letters* **1998**, *23*, 1331.

[14] M. L. Brongersma, J. W. Hartman, H. A. Atwater, *Physical Review B* **2000**, *62*, 16356.

[15] B. W. Smith, M. Monthioux, D. E. Luzzi, *Nature* **1998**, *396*, 323.

[16] J. S. Wu, S. Dhara, C. T. Wu, K. H. Chen, Y. F. Chen, L. C. Chen, *Advanced Materials* **2002**, *14*, 1847.

[17] M. S. Hu, H. L. Chen, C. H. Shen, L. S. Hong, B. R. Huang, K. H. Chen, L. C. Chen, *Nature Materials* **2006**, 5, 102.

[18] M. J. Sailor, E. J. Lee, *Advanced Materials* **1997**, *9*, 783.

[19] J. M. Buriak, *Chemical Reviews* **2002**, *102*, 1271.

[20] B. Sweryda-Krawiec, T. Cassagneau, J. H. Fendler, *Journal of Physical Chemistry B* **1999**, *103*, 9524.

[21] P. A. Schueler, J. T. Ives, F. Delacroix, W. B. Lacy, P. A. Becker, J. M. Li, K. D. Caldwell, B. Drake, J. M. Harris, *Analytical Chemistry* **1993**, *65*, 3177.

[22] S. R. Sershen, S. L. Westcott, N. J. Halas, J. L. West, *Applied Physics Letters* **2002**, *80*, 4609.

[23] C. L. Nehl, N. K. Grady, G. P. Goodrich, F. Tam, N. J. Halas, J. H. Hafner, *Nano Letters* **2004**, *4*, 2355.

[24] Z. J. Jiang, C. Y. Liu, *Journal of Physical Chemistry B* **2003**, *107*, 12411.

[25] J. B. Jackson, N. J. Halas, *Journal of Physical Chemistry B* **2001**, *105*, 2743.

[26] H. P. Liang, L. J. Wan, C. L. Bai, L. Jiang, *Journal of Physical Chemistry B* **2005**, *109*, 7795.

[27] Y. Cui, X. F. Duan, J. T. Hu, C. M. Lieber, *Journal of Physical Chemistry B* **2000**, *104*, 5213.

[28] Y. Cui, C. M. Lieber, *Science* **2001**, *291*, 851.

[29] Y. H. Tang, X. H. Sun, F. C. K. Au, L. S. Liao, H. Y. Peng, C. S. Lee, S. T. Lee, T. K. Sham, *Applied Physics Letters* **2001**, *79*, 1673.

[30] D. D. D. Ma, C. S. Lee, S. T. Lee, *Applied Physics Letters* **2001**, *79*, 2468.

[31] Y. H. Tang, T. K. Sham, A. Jurgensen, Y. F. Hu, C. S. Lee, S. T. Lee, *Applied Physics Letters* **2002**, *80*, 3709.

[32] R. G. Elliman, A. R. Wilkinson, T. Kim, P. Sekhar, S. Bhansali, *Nuclear Instruments & Methods in Physics Research Section B-Beam Interactions with Materials and Atoms* **2008**, *266*, 1362.

[33] P. K. Sekhar, A. R. Wilkinson, R. G. Elliman, T. H. Kim, S. Bhansali, *Journal of Physical Chemistry C* **2008**, *112*, 20109.

[34] D. P. Yu, Q. L. Hang, Y. Ding, H. Z. Zhang, Z. G. Bai, J. J. Wang, Y. H. Zou, W. Qian, G. C. Xiong, S. Q. Feng, *Applied Physics Letters* **1998**, *73*, 3076.
[35] D. Wang, F. Qian, C. Yang, Z. H. Zhong, C. M. Lieber, *Nano Letters* **2004**, *4*, 871.
[36] R. G. Elliman, A. R. Wilkinson, T. H. Kim, P. K. Sekhar, S. Bhansali, *Journal of Applied Physics* **2008**, *103*.
[37] H. J. Choi, J. H. Shin, K. Suh, H. K. Seong, H. C. Han, J. C. Lee, *Nano Letters* **2005**, *5*, 2432.
[38] R. A. B. Devine, *Journal of Non-Crystalline Solids* **1993**, *152*, 50.
[39] M. Handke, W. Mozgawa, *Journal of Molecular Structure* **1995**, *348*, 341.
[40] X. C. Wu, W. H. Song, K. Y. Wang, T. Hu, B. Zhao, Y. P. Sun, J. J. Du, *Chemical Physics Letters* **2001**, *336*, 53.
[41] J. H. Stathis, M. A. Kastner, *Physical Review B* **1987**, *35*, 2972.
[42] C. Itoh, T. Suzuki, N. Itoh, *Physical Review B* **1990**, *41*, 3794.
[43] H. Nishikawa, T. Shiroyama, R. Nakamura, Y. Ohki, K. Nagasawa, Y. Hama, *Physical Review B* **1992**, *45*, 586.
[44] L. Skuja, *Journal of Non-Crystalline Solids* **1998**, *239*, 16.
[45] G. G. Qin, J. Lin, J. Q. Duan, G. Q. Yao, *Applied Physics Letters* **1996**, *69*, 1689.
[46] K. Awazu, H. Kawazoe, K. Muta, *Journal of Applied Physics* **1991**, *70*, 69.
[47] L. S. Liao, X. M. Bao, X. Q. Zheng, N. S. Li, N. B. Min, *Applied Physics Letters* **1996**, *68*, 850.
[48] K. Sato, N. Kishimoto, K. Hirakuri, *Journal of Applied Physics* **2007**, *102*.
[49] H. Z. Song, X. M. Bao, *Physical Review B* **1997**, *55*, 6988.
[50] A. Franceschetti, S. J. Pennycook, S. T. Pantelides, *Chemical Physics Letters* **2003**, *374*, 471.
[51] E. I. Alessandrini, D. R. Campbell, K. N. Tu, *Journal of Vacuum Science & Technology* **1976**, *13*, 55.
[52] C. C. Buttner, N. D. Zakharov, E. Pippel, U. Gosele, P. Werner, *Semiconductor Science and Technology* **2008**, *23*.
[53] P. Werner, C. C. Buttner, L. Schubert, G. Gerth, N. D. Zakarov, U. Gosele, *International Journal of Materials Research* **2007**, *98*, 1066.
[54] M. E. Toimil-Molares, A. G. Balogh, T. W. Cornelius, R. Neumann, C. Trautmann, *Applied Physics Letters* **2004**, *85*, 5337.
[55] K. F. Gurski, G. B. McFadden, *Proceedings of the Royal Society of London Series a-Mathematical Physical and Engineering Sciences* **2003**, *459*, 2575.
[56] N. H. Fletcher, R. G. Elliman, T. H. Kim, *Nanotechnology* **2009**, *20*.
[57] S. Roorda, T. van Dillen, A. Polman, C. Graf, A. van Blaaderen, B. J. Kooi, *Advanced Materials* **2004**, *16*, 235.
[58] X. H. N. Xu, S. Huang, W. Brownlow, K. Salaita, R. B. Jeffers, *Journal of Physical Chemistry B* **2004**, *108*, 15543.
[59] J. H. Zhang, H. Y. Liu, Z. L. Wang, N. B. Ming, *Advanced Functional Materials* **2007**, *17*, 3295.
[60] Z. S. Li, C. X. Kan, W. P. Cai, *Applied Physics Letters* **2003**, *82*, 1392.
[61] X. M. Meng, J. Q. Hu, Y. Jiang, C. S. Lee, S. T. Lee, *Applied Physics Letters* **2003**, *83*, 2241.
[62] Y. Y. Yu, S. S. Chang, C. L. Lee, C. R. C. Wang, *Journal of Physical Chemistry B* **1997**, *101*, 6661.
[63] M. B. Mohamed, K. Z. Ismail, S. Link, M. A. El-Sayed, *Journal of Physical Chemistry B* **1998**, *102*, 9370.
[64] N. R. Jana, L. Gearheart, C. J. Murphy, *Advanced Materials* **2001**, *13*, 1389.
[65] N. Malikova, I. Pastoriza-Santos, M. Schierhorn, N. A. Kotov, L. M. Liz-Marzan, *Langmuir* **2002**, *18*, 3694.
[66] W. Strek, P. J. Deren, K. Maruszewski, E. Pawlik, W. Wojcik, G. E. Malashkevich, V. I. Gaishun, *Journal of Alloys and Compounds* **1998**, *275*, 420.
[67] J. U. Kang, *Applied Physics Letters* **2006**, *89*.

Chapter 6

Concluding remarks

6.1 Conclusions

This thesis examined the physical properties and possible applications of silicon rich oxide films deposited by PECVD and the synthesis, structure and properties of one dimensional silica and hybrid metal-silica nanostructures.

PECVD deposited silicon rich oxide films were shown to develop high tensile stress during the annealing process. The effect of varying film stress was shown to be correlated with densification and a loss of hydrogen. For critical film thickness and annealing at high temperatures (up to 650°C), failure modes such as delamination and cracking was caused by the film stress. Two distinct modes of crack propagation were reported for film on a (100) Si substrate: straight cracks along [100] directions in the underlying Si substrate or oscillating cracks propagating along [100] directions underlying substrate. The wavelength and amplitude of oscillating cracks was modified by the addition of a SiO_2 buffer layer and ion implantation was shown to reduce the density of cracks. Other properties of SRO films were investigated for specific applications. Charge trapping in SRO layers correlated with hydrogen release and the formation of metal nanoparticles within SRO films by direct thermal reaction with a deposited metal.

During the course of study of formation of metal nanoparticles in SRO matrix, the growth of one dimensional SiO_x nanostructures at elevated temperatures with high Si content on SRO films provided the new research directions. Henceforth, a systematic study was performed to understand the growth mechanism of SiO_x nanowires and their potential applications.

The growth mechanism of silica nanowires on metal coated Si substrates using a simple self-sourcing process has highlighted some of the experimental dependencies of growth process. A proposed model of nanowire growth is based on the production of SiO as a vapour phase source of Si and O via a reaction between Si and residual oxygen, present in the annealing ambient at 3-10ppm, described by: $2Si + O_2 \rightarrow 2SiO$. The SiO vapour so produced is absorbed by metal catalyst particles and facilitates nanowire growth via a VLS growth mechanism. The dominance of this reaction over the competing reaction: $Si + O_2 \rightarrow SiO_2$ is a strong function of oxygen concentration and temperature and for the fixed oxygen concentration employed in this study, limits growth to the temperature range >1000°C.

The diameter of SiO_x nanowires is dependent on many factors, including the catalyst/substrate combination, process gases, growth temperature, or combinations of these parameters. Critically, the nanowire diameter is also directly related to the size of the metal seed particles. This thesis has examined the size dependency of the Au nanoparticles and the resulting silica nanowires to the initial deposited Au films of varying thicknesses. During this process it has been observed that the diameter of the silica nanowires depends upon the size of the Au droplets, which is itself determined by the thickness of the original Au film.

In addition to the above mentioned detail investigation, more subtle growth modes, including the growth of nanowires on substrates other than silicon in which a secondary source of SiO was produced by a Si capping wafer in the vicinity of the substrate were also investigated. The influence of experimental parameters on the structure and morphology of the nanowires was also studied.

The fabrication of hybrid metal-silica nanostructures by using different approaches was examined. These structures include self-supporting nanowire films, Au peapod structures, Au decorated nanowires, core-shell nanowires, and hyper-hybrid silica nanowires. Growth mechanism of these structures was presented with proposed models and basic optical properties such as optical absorption and photoluminescence were discussed for potential applications.

6.2 Future work

Despite the intense research effort devoted to studying the mechanical properties of SRO films deposited by PECVD many important technological challenges remain. Further work is required to understand the how deposition and processing conditions affect film stress. The effect of substrate temperatures greater than 300°C on hydrogen retention and stress are critical in this regard. .

With regard to silica nanowires, future work is required to more fully understand the synthesis, structure and properties of hybrid metal-silica and coated-silica nanostructures; and to examine the potential of such structures for environmental and biological sensing, microcatalysis, etc. The ability to coat nanowires with functional materials using ALD or CVD is an area of particular interest in this regard.